Experimental Investigation of Flow Control Techniques To Reduce Hydroacoustic Rotor-Stator Interaction Noise

By:

Sarah Tweedie

Thesis submitted to the faculty of Virginia Polytechnic Institute and State University
in partial fulfillment of the requirements
for the degree

Master of Science
in
Mechanical Engineering

Approved by:

Dr. Wing F. Ng, Committee Chairman
Dr. Martin Johnson
Dr. Pavlos P. Vlachos
Dr. Jason Anderson

September 7, 2006
Blacksburg, Virginia

Keywords: rotor-stator interaction, hydroacoustics, active flow control, noise reduction, trailing edge blowing, leading edge blowing

Experimental Investigation of Flow Control Techniques To Reduce Hydroacoustic Rotor-Stator Interaction Noise

Sarah Tweedie

Abstract

Control of radiated acoustic noise is vital to the survivability and the detectability of submersible watercraft. Two primary sources of radiated fluid noise in submersible vessels are the boundary layer turbulence along the forebody and propulsor fluid-structure interaction. The propulsor contains several locations of such interaction, one of which was investigated in this research. Specifically, this research focused on experimentally investigating active flow control techniques to reduce rotor-stator interaction noise sources.

Two of the three flow control configurations applied to the flow involved the application of active flow control to the leading edge of a single exit guide vane (EGV) mounted downstream of a seven-bladed rotor. The leading edge blowing configuration (LEB) consisted of a single jet expelled from the leading edge of the EGV against the oncoming flow. This interaction between the wake and jet should offset or disrupt the coherency of any incoming flow structures. The second active flow control method applied to the EGV involved a tangential blowing configuration (TB) where two symmetric tangential jets were used to create an insulating fluid layer that reduced the effect of passing flow structures on the EGV. The final flow control design was the implementation of trailing edge wake filling on a three bladed rotor. A rotor was designed to ingest lower velocity flow from the hub and pump the fluid out of a blowing slot at the blade trailing edge. The blowing slot was concentrated on the outer third of the blade span in order to maximize pumping effect.

In order to quantify the effects of the active flow control techniques on rotor-stator interaction, the fluctuating lift force on the EGV was measured. Since this fluctuating force serves as a primary acoustic source, the effects of the active flow control on the radiated interaction sound can be estimated. These active flow control techniques were intended for reduction of blade passing frequency tonal sound radiation. The LEB configuration showed minor changes in overall spectral response; however, there was no significant reduction in forcing at the BPF measured. Similarly the TB configuration also yielded no measurable change in BPF tonal forcing. The first generation design of the self-pumping rotor also proved to have problems. Experiments showed that the application of the flow control on the self-pumping rotor did not generate the expected increase in torque demand or changes in the tonal forcing on the EGV. Field alterations to the rotor were unable to improve the performance; therefore, the conclusion became that the initial design was unable to pump fluid due to excessive pressure losses. Further design iterations are required to perfect the functionality of the self-pumping rotor.

Acknowledgements

Most of all, I would like to thank the staff at Techsburg for all of their help in performing this research. Especially I would like to thank Dr. Jason Anderson for all of his exhaustive help throughout the past year. His advice and experience was vital in both the experiments and this thesis. Also, the Techsburg machine shop was instrumental in this work thanks to their expert work in machining the components for the test assembly.

I would like to express my appreciation to my committee for their help, advice, and patience throughout this work.

My thanks also go to the graduate students of the CTFS Randolph and the Norris Fluids lab for their help with the experiments. All of the people in these labs were willing to lend a hand when I was in a bind.

I would like to thank my family for all of their help and support. They encouraged me through setbacks and listening to my trials and tribulations without complaint.

Dedication

In memory of Lucy Simons, my grandmother

1928 - 2005

Table Of Contents

Table of Figures

Table of Tables

Nomenclature

Terms

EGV ..... exit guide vane
IGV ..... inlet guide vane
LEB ..... leading edge blowing configuration
TB ..... tangential blowing configuration
SPR ..... self-pumping rotor
rpm ..... revolution per minute
CAD ..... computer assisted drafting
ESM ..... Engineering Science and Mechanics Department
NSWC ..... Naval Surface Warfare Center, Carderock
SLA ..... stereolithography
PIV ..... particle image velocimetry

Variables

F_L ..... fluctuating lift force on the EGV
∇_x ..... gradient computed at the measured location
N ..... rotor speed, rpm
B ..... blade number
s ..... blade span
c ..... blade chord
C ..... chord-wise location in EGV coordinate system
L ..... span-wise location in EGV coordinate system
BPF ..... blade passing frequency, N*B/60
p ..... acoustic pressure
d ..... distance between an airfoil and a passing vortex
l ..... length of the airfoil
Γ ..... circulation
ρ ..... density
H_1 ..... frequency response function estimator
ε ..... strain
K ..... strain gauge factor
c_0 ..... speed of sound
G ..... Green's function
x, y ..... coordinate locations on the EGV blade
S_v ..... surface of the EGV
fs ..... force per unit area of the EGV surface
f_v ..... force per unit volume of the EGV surface
H_0 ..... null hypothesis for Student's t-test
H_a ..... alternative hypothesis for Student's t-test
t_0 ..... test statistic for Student's t-test
σ, $s_{1,2}$ ..... standard deviation

$\mu_{1,2}$ ..... mean
df ..... degrees of freedom
$n_{1,2}$ ..... number of samples
z ..... standard normal value
α ..... probability
E ..... excitation voltage for the strain gauges
Δe ..... change in voltage output by the strain gauges
CV ..... Coefficient of Variation

1 Introduction

With the ever-growing world population, the impact of man-made noise sources has begun to be a major concern. Airplanes, helicopters, cars, and all variety of land transportation are required to meet certain noise pollution standards. Similar restrictions are beginning to be implemented regarding water travel. One reason is because the effect of man-made noise on undersea life is just now being understood. Also, in order to increase the effectiveness of naval vessels in wartime, it is vital that submarines, surface ships, and torpedoes emit as little sound as possible. To this end industry encourages the development of noise reducing methods in order to decrease the acoustic signatures of naval vessels.

1.1 Need of hydroacoustic noise reduction

Military vessels are tracked and detected by the acoustic noise they produce. Improving noise reduction lowers the radiation from the vessel, thus improving the survivability of the vessel. This is most important to submarines and torpedoes. There are two types of noise that cause a vessel to be detected, broadband and tonal. While both broadband and tonal noise emission contribute to detectability, the tonal noise is vehicle specific and can be used to identify specific craft. Table 1.1 shows the sources of these two types of acoustic noise. For most vessels a significant source of noise is the propulsion system, see Figure 1.1. Currently, naval vessels use either an open or ducted propulsor system as their main propulsion system. More recent submarines and torpedoes predominately utilize ducted pumpjet propulsors.[1] Figure 1.2A shows a diagram of the propulsion unit for the US Navy's heavyweight MK-48 torpedo. As can be seen, the unit has a ducted propeller configuration in order to maximize thrust. This type of ducted propulsor can be treated with flow control methods in order to reduce the hydrodynamic noise created by the propeller. The unducted propeller is used more frequently with both military and commercial surface ships, seen in Figure 1.2B. Both drive systems could benefit from acoustic reduction.

Table 1.1: Sources of Noise in an underwater vessel

Source	Type of Acoustic Radiation
Forebody- boundary layer turbulence	Broadband
Propulsor	Broadband and tonal

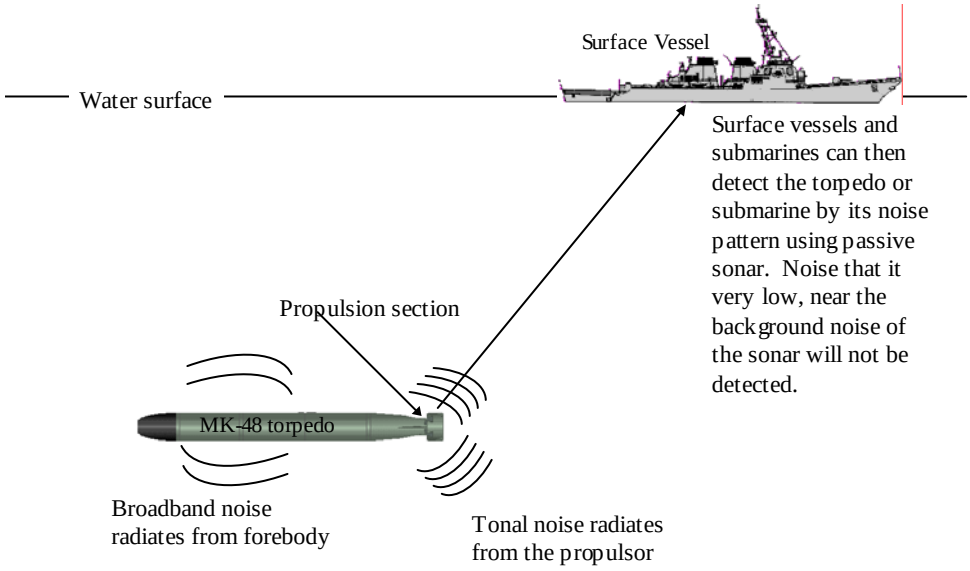

Figure 1.1: Sound waves generated by the propulsion section of a torpedo propagate away from the body and, if strong enough, can be measured by the sonar array on any nearby submarines or surface vessels.

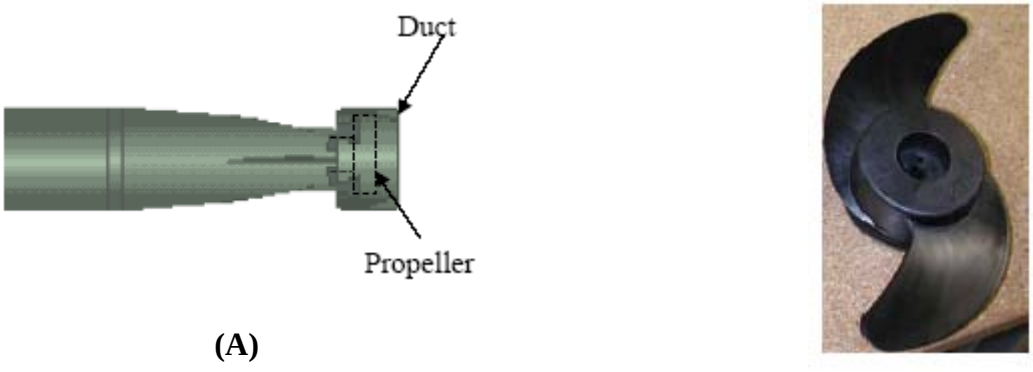

(A)

(B)

Figure 1.2: (A) Propulsor diagram for a MK-48 heavyweight torpedo. (B) Two bladed propeller for a small trolling motor, capable of propelling a small fishing boat at a slow rate of speed. This propeller is turned in open water by a single driveshaft.

1.2 Main Causes of Underwater Propulsor Noise

The two main causes of propulsor noise are mechanical and hydrodynamic. In general, hydrodynamic noise refers to all of the undesired sound that is generated as a body flows through water. In this case, hydrodynamic noise refers to the acoustic waves generated when a fluid interacts with a solid structure. A non-uniform unsteady flow field impinges on a structure, imparting a force on the structure; this causes a resultant force to be exerted on the surrounding fluid. It can be shown that this force, F_L, is directly related to the radiated acoustic noise by the equation,

$$p(\bar{x},t) \approx \frac{1}{4\pi|\bar{x}-\bar{y}_c|}\nabla_x \cdot \bar{F}_L\left(\bar{y}_c, t-|\bar{x}-\bar{y}|/c_0\right), \qquad \textbf{1.1}$$

A detailed derivation of Equation 1.1 is shown in Appendix A.

The typical propulsor for a torpedo, shown in Figure 1.3, consists of a 1.5 stage turbomachine mounted inside of a duct. Each portion of the machine creates flow non-uniformities that interact with every other stage to produce sound. The primary interaction noise sources are associated with the unsteady impingement of viscous wakes with downstream stages. Thus, the two main interactions with respect to noise generation that occur in the propulsor shown in Figure 1.3 are the interactions of the IGV wakes with the rotor and the rotor wakes with the EGV. These interactions create predominately tonal noise. Alternately, the acoustic noise generated by turbulent flow, as is found in a high velocity jet, is spread across all frequencies; otherwise known as broadband noise. The main hydrodynamic noise sources in this type of propulsor are listed in Table 1.2. Sources 1, 2, and 3 all have tonal components at the harmonics of the BPF from their interaction with the rotor. Sources 2 and 3 interact directly with the rotor, while the inlet distortion travels downstream and interacts with the rotor after passing the IGV. The exhaust from propulsor is normally a turbulent jet. This turbulence causes solely broadband noise.

Table 1.2: Noise sources within a propulsor

	Source	Acoustic Nature
1	Inlet Inflow Distortion	Broadband and tonal
2	Inlet Guide Vane (IGV) – Rotor Interaction	Broadband and tonal
3	Rotor – Exit Guide Vane (EGV) Interaction	Broadband and tonal
4	Exhaust Jet	Broadband

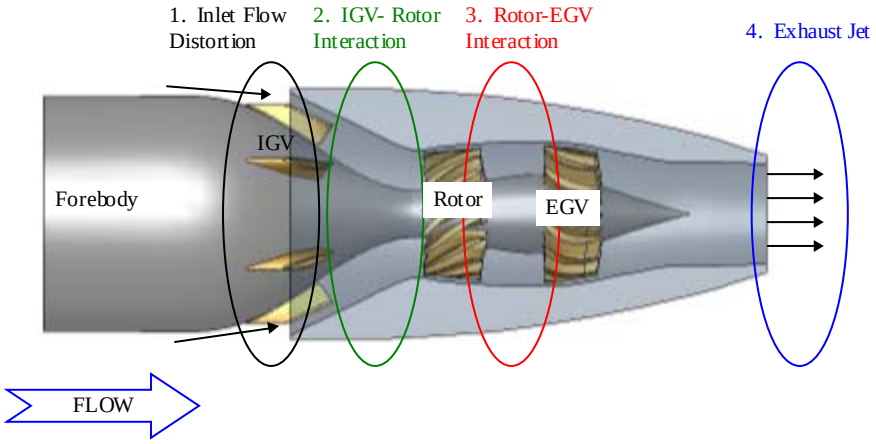

Figure 1.3: Diagram of the four main noise sources in a typical torpedo propulsor.

The other major source of propulsor noise is that caused by mechanical components. Mechanical noise refers to the noise generated by the bearings, shafts, gears, and other moving parts within the propulsion unit. This is the same type of noise that would be generated by any system with moving parts. For example, the gears rub against each other while rotating; creating vibration that is transmitted to the rest of the structure. Most engines and transmission systems are designed to minimize the amount of rubbing and shaft imbalance because it also reduces system performance. However, any imbalance in the propeller can effect the operation of the entire system. A great deal of the mechanical noise can be reduced in the initial design or by the addition of vibration isolation to reduce the amount of vibration transmitted between different sections of the machine.

1.3 Flow Control Methods for Reducing Hydrodynamic Noise

This work focuses on the reduction of hydrodynamic noise in a propulsion system by means of flow control. In this context, flow control is a technique wherein the flow field is altered in order to achieve a desired flow pattern. There are two means of altering the flow field, active and passive. In general, passive flow control involves the generation of additional vorticity in order to mix low momentum fluid with high momentum fluid. Conversely, in the application of active flow control to reduce interaction noise, there are two approaches: wake-filling and vortex-enhanced mixing. The wake-filling approach involves the addition of fluid momentum at the trailing edge of lifting bodes in order to reduce the downstream wake velocity deficit. This reduction in velocity deficit reduces the unsteady loads on any downstream components that cause noise. In regards to reducing hydroacoustic interaction noise sources in a propulsor, the flow mixing is predominately applied to reduce the velocity and momentum deficit in the wakes shed from stationary blades.

In this research two main types of active flow control were applied for the reduction of the interaction of a rotor wake on a single stator. The first, leading edge flow control, consists of adding fluid at the leading edge of the noise producing structure in order to prevent the structure from receiving any unsteady fluid forcing. This type of flow control was tested using two different configurations: straight leading edge blowing and tangential blowing. The leading edge blowing geometry (LEB) is designed to increase the offset distance of any impinging vortices by creating a “virtual leading edge” that diverts the vortices away from the airfoil surface. Similarly, the tangential blowing geometry (TB) is designed to have a flow control jet attach to the blade surface and insulate it from impinging vortices in the external flow. The second type of active flow control is the application of trailing edge wake-filling to the rotor. To implement the wake filling on a rotor without the implementation of complicated supply lines, a “self-pumping” design was created to ingest the boundary layer from the centerbody into the hub and, using centrifugal force to drive the fluid, expel a jet from the trailing edge of the rotor.

1.4 Thesis Outline

This thesis will present results from the test of three different active flow control configurations designed to reduce the force transmitted to a downstream exit guide vane (EGV). First, the background on how the fluid-structure interaction impacts the radiated acoustic noise will be reviewed. The previous work done using similar flow control configurations will be presented in Chapter 2. The experimental assembly and the instrumentation associated with it will be explained in Chapter 3. Results from the two flow control configurations applied to the single exit guide vane will be reported in Chapter 4. Finally, in Chapter 5 the results from the self-pumping trailing-edge flow controlled rotor design will be reviewed.

2 Literature Review

The acoustic noise caused by fluid interactions with solid bodies is a well-researched field. Theoretical and experimental research has led to a solid understanding of the basic mechanisms by which fluids can cause structures to radiate noise. The turbomachinery industry has led the drive to apply these results to reducing the noise generated by a rotor wake. Thus, the flow control techniques of trailing- and leading-edge blowing have been introduced. The trailing-edge blowing technique has been extensively tested in air, but has not been widely implemented in water vehicles. The leading-edge blowing technique is the newest method and has not yet been widely tested. The following sections give a summary of the previous research, both experimental and theoretical, performed in all three of these areas.

2.1 Fluid-Structure Interaction and Rotor-Stator Noise

One of the principle methods of noise generation in a fluid machine is the sound produced by the unsteady forced response of rotor blades and stator vanes to the surrounding fluctuating flowfield. These fluctuating forces on the rotor blades and stator vanes produce an acoustic pressure field described by Equation 1.1, which resembles that of a dipole. Two dominant causes of these dipole sources are the rotor wake impinging on the downstream stators and to a lesser effect the potential field of the stators extending upstream to interfere with the rotor.[2] Woodward and Balombin confirmed the effects of the rotor-stator interaction on the radiated noise by examining the change in sound pressure level with and without downstream struts to support the motor. They found that adding struts within downstream of the rotor showed an increase of 10 dB at the BPF tone. The amount of noise generated depended directly on the distance between the rotor and the stators. The smaller the distance, the more tonal noise occurred. However, the addition of struts did not change the broadband noise or the higher harmonics of the BPF.[3]

The forcing on downstream bodies, in this case an exit guide vane (EGV), is caused by the non-uniform flowfield from the rotor. The momentum deficit that is inherent in a viscous wake causes an upwash velocity on the EGV. As the wake passes by the stationary EGV the blade is subjected to a fluctuating upwash velocity, see Figure 2.1, which translates into a fluctuating reaction force exerted by the EGV onto surrounding fluid. The fluctuating force is the source for

acoustic pressure radiation described by Equation 1.1. The implication of this relationship is that the impact on acoustic radiation can be approximated experimentally by the force imparted on a structure. Goldstein derived a method to compute the tonal component of this fluctuating interaction force from a known impinging wake flow field, thus enabling an analytical estimation of the forcing on a blade in some circumstances.[4]

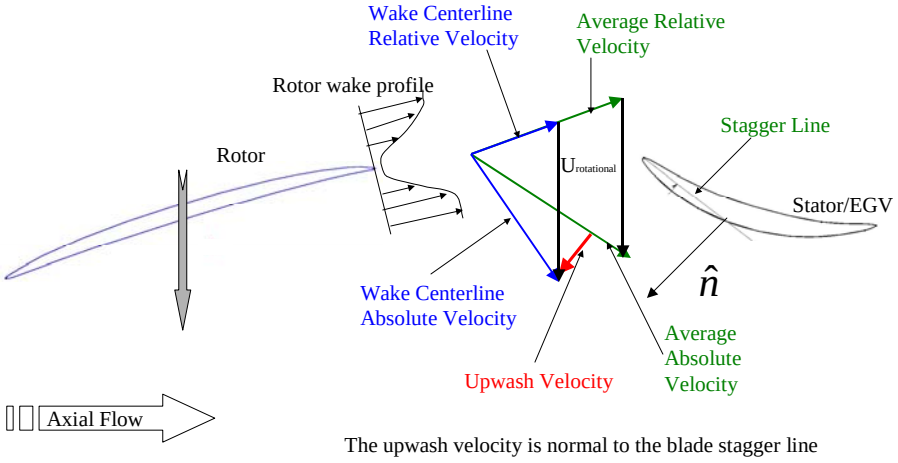

Figure 2.1: Diagram of upwash velocity with relation to a fan stage.

The rotor wake is a result of the viscous effects of the fluid as it passes by the moving rotor blade.[5] However, the blade-wake interaction can be approximated as an inviscid interaction in most turbomachines because the viscous effects do not significantly impact the behavior of the wake interaction with the downstream stator. This means that analytical approximations can use the simpler Euler equations to model the interactions as well as the more complicated Navier-Stokes equations.[6] These analytical models are confirmed by experiments on the radiated noise from turbomachines. For most of such turbomachines, the rotor/stator stage is housed inside of a duct, which significantly impacts the radiated acoustic noise. The shape and size of the duct determines the frequencies that are able propagate through the duct and out to the far field. In addition, the interaction creates specific circumferential modes that are determined by the blade count of both the rotor and the stator. These circumferential modes that are created and allowed to propagate to the far field constitute the tonal noise that is measured experimentally.[7] This tonal noise can be reduced by either acoustic treatments in the duct or reduction of the initial wake interaction.

The rotor-stator interaction problem has been well researched throughout the past years. In this time, several different techniques for reducing the effects of the interaction on performance and radiated acoustic noise have been researched. Since the rotor-stator interaction is one of the major sources of noise in high speed gas turbines and aircraft engines[7], most of this research has been performed in air. However, in many cases techniques that show improvement in aerodynamic applications will also show benefits in hydrodynamic applications. One of these methods of noise reduction is known as active noise control (ANC), which operates by using additional noise sources to cancel out or reduce the propagation of the rotor-stator interaction tones to the far field. Sawyer et al. used acoustic sources mounted on the stator vanes to match the tones radiated from the wake interaction. This configuration showed a reduction in radiated sound pressure level of 10 dB over all of the motor operating speeds, with larger reductions present at certain operating point. Hall and Woodward used experimental results to estimate the reduction of perceived noise given the removal of the certain radiated tones via active noise control. This research found that the removal of the BPF tone by active noise control would yield a reduction in radiated noise level of 2-3 dB.[8] This technique shows the most effectiveness in ducted propulsors where the duct allows the ANC to cancel the rotor-stator interaction noise before the sound leaves the duct to propagate into the far field. However, ANC does require extensive equipment, such as acoustic drivers and power amplifiers, that can add additional weight and complexity to the propulsor.

Another means of reducing the noise generated by the rotor-stator interaction is the application of active aerodynamic means to change the nature of the interaction between the wake and the solid body. One of these means is an actuated flap that serves as a control of the unsteady lift on the airfoil. Since the unsteady lift force exerted on the blade is the cause of most of the radiated tonal noise, reducing the magnitude of this unsteadiness should reduce the radiated noise. Simonich et al experimentally tested this technique using a single stator positioned downstream of a simple two bladed propeller. The flap on the trailing edge of the stator would actuate in response to the incoming wakes in order to achieve a lift force on the stator that remained constant. Using this technique, a 10 dB reduction was found at certain frequencies as well as a reduction of the peak to peak acoustic pressure by a factor of 2.[9] Minter and Fleeter also showed positive results applying this technique to both a single stator vane and a three vane cascade. The upstream and downstream propagating modes showed maximum

decreases of 9 and 6.5 dB, respectively.[10] While this method is beneficial, the mechanisms required for actuating the flap adds weight and complexity to the turbomachine.

Passive means of reducing the rotor-stator interaction can provide some of the same benefits as the active means, yet without the need of additional mechanical components. Alteration of the geometry of the turbomachine is a type of passive treatment of the rotor-stator interaction. First, since the rotor wake diffuses as it propagates downstream, increasing the axial distance between the rotor and stator reduces the velocity deficit felt by the stator.[11] Reducing the velocity deficit reduces the force imparted to the blade and thus the radiated noise. Kantola and Gliebe found that applying an increase in rotor stator spacing of 0.5 to 2.3 times the rotor chord length yields a reduction in the BPF tone sound level of 3 dB.[12] However, increasing the axial distance requires a longer turbomachine; an increase in length also causes an increase in the total weight of the propulsor. In many cases, the propulsor size and weight are intended to be a small as possible in order to meet design constraints, thus increasing the size creates detrimental effects on the design. Other passive techniques designed to reduce turbomachine noise include reducing the rotor tip clearance and adding lean to the stators. Hughes et al. showed that the decreasing the rotor tip clearance in a 22 blade turbofan simulator increased the performance of the fan while decreasing the radiated broadband noise. However, the rotor-stator interaction tonal noise increased for the smaller tip clearances, possibly due to the interaction of the rotor tip with the boundary layer on the duct wall.[13]

The use of lean and sweep in the stator design reduces the noise radiated due to rotor wake- stator interaction by changing the radial variation of the incoming flow. This causes a phase shift of the unsteady upwash velocity which distributes the interaction energy across higher order acoustic modes. By energizing the higher order modes as opposed to the lower modes the energy created by the wake interaction can be channeled into the higher modes that are cut off by the duct. Elhadidi and Atassi used analytical techniques to confirm that the application of leaned stators will reduce the radiated noise. However, this passive technique was only found to be effective for lower mode numbers.[11] Woodward et al. experimentally tested this theory on a row of 42 stators driven by an 18 blade rotor. Using a 30^{o} sweep and lean angle, a reduction of both broadband and tonal was observed; the broadband noise indicated the most significant reduction of 4 dB as opposed to the 3 dB reduction of BPF tonal noise.[14]

Many different flow control techniques have been researched to determine their effectiveness in controlling rotor-stator interaction. The passive techniques involve no moving parts or alteration of the flow due to fluid injection. Some such passive techniques include using lean on the stators to change the strength of the BPF and its harmonics, increasing the axial spacing between the rotor and the stator, and changing the tip clearance to reduce either tonal or broadband radiated noise. These passive techniques do not have the mechanical complexity of the active techniques; however, the passive techniques outlined here have not shown the same magnitude of noise reduction as some of the active techniques. In addition to the active noise control and active lift control, there is a flow control technique that uses momentum injection to reduce the rotor-stator interaction. This technique is known as active flow control. There are two main types of active flow control; both types will be explained in the following sections. Application of these techniques in experiment has shown the potential for larger noise reduction than some passive techniques without the complexity of the mechanical actuators needed for active lift control.

2.2 Trailing Edge Blowing

The trailing edge blowing technique has been applied in many different fields. The primary application has been for acoustic noise reduction in turbomachines. The viscous wake formed by an airfoil moving through a fluid has a region of low momentum that propagates downstream from the rotor. As the wake progresses downstream it interacts with downstream objects, such as an exit guide vane, causing fluctuating pressures of the structure surface.[15] These pressures radiate acoustic noise from the blade. Trailing edge blowing (TEB) means the application of flow control to the blade trailing edge to energize the low momentum section of the wake. Figure 2.2 shows an illustration of the effects of trailing edge blowing on the rotor wake that would impinge on downstream bodies. Often TEB involves momentum injection to fill in the deficits that are formed by the flow of fluid around a rotor blade. The momentum is added in the form of fluid ejected from the trailing edge of the airfoil.[16]

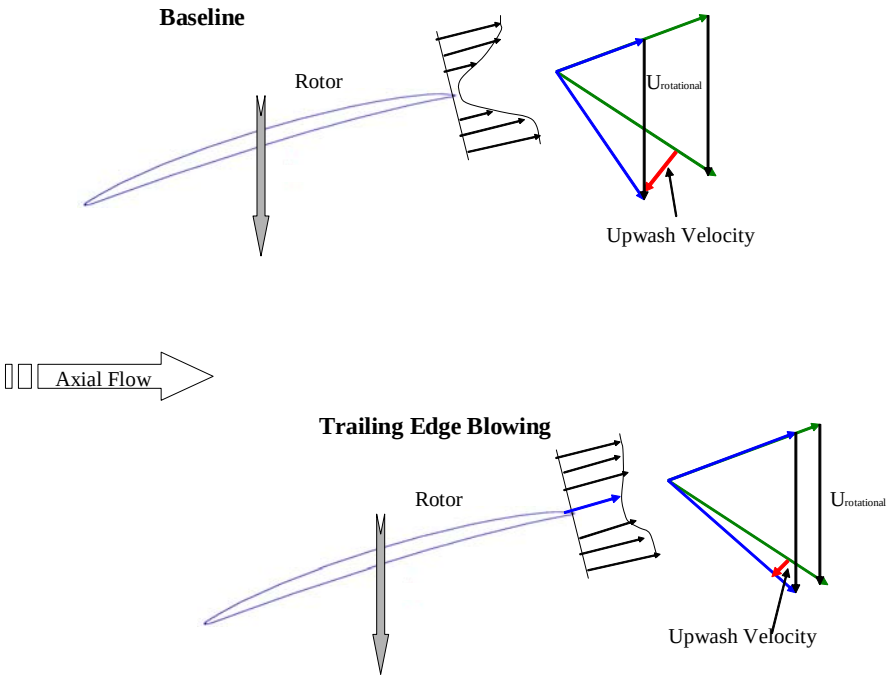

Figure 2.2: Diagram of the effects of trailing edge blowing on the wake shed by a rotor.

The benefits of this technique have been experimentally determined extensively in air. Brookfield and Waitz applied TEB for a high-bypass ratio fan stage with the mass injected being less than 2% of the fan throughflow. They tested two different spanwise blowing distributions along the fan blade, one where the majority of flow came from the fan tip and another where the flow came from the fan midspan. The tip-weighted configuration showed a reduction of up to 10 dB in tonal tone at the blade passing frequency. The midspan-weighted configuration also showed reductions, though less significant than the tip-weighted geometry.[17] Similar results using a tip-weight blowing configuration were found by Langford et al using only 0.7% fan throughflow to achieve a reduction of 7 dB in tonal noise.[18]

Fite et al. showed a 2 dB reduction in BPF tone for all test speeds, using a continuous slot on an 18 blade fan with 2% of the fan throughflow ejected from the trailing edge. For specific test speeds a greater tonal noise reduction of 6 dB was observed.[19] Using a similar configuration of total span trailing edge blowing on a 16 blade fan, Sutliff et al. found a 5.4 dB reduction of the far field radiated noise for 1.6 to 1.8% fan throughflow. In addition, larger reductions of 10.6 and 12.4 dB were observed for the 2xBPF and 3xBPF harmonics, respectively.[20]

Several different TEB jet designs have been evaluated. Naumann researched the use of discrete jets instead of the slots. The jets act as both momentum injection and vortex generation

in order to increase mixing. The mixing effect was found to enhance the effects of the flow control.[21] Fleming and Johnson investigated the application of this technique in a hydrodynamic situation. Tests were conducted on a ducted fan with TEB applied to an upstream inlet guide vane. The flow control was designed using a row of discrete jets positioned on both sides of the symmetric inlet guide vane. A hydrophone mounted outside of the ducted fan assembly measured the change in radiated noise. The results showed a 7 dB reduction in radiated tonal noise at the blade passing frequency.[22] Other experiments performed in air also showed a reduction in the wake velocity deficit produced by the rotor. Wo et al. demonstrated that the application of flow control along the span of the blade filled at least a portion of the wake velocity deficit for all of the mass flow injection rates tested. This reduction in velocity deficit did show a similar reduction in the force transmitted to the downstream stator.[23]

To this author's knowledge the "self-pumping" rotor design investigated in this paper has not previously been presented for open publication. The application of boundary layer suction immediately upstream of a rotor has been applied to high-speed compressors with some success in improving performance, yet the effect noise radiation was not studied specifically.[24] However, in such aspirated compressors the removed fluid was not rerouted to supply any active flow control on the rotor.

2.3 Leading Edge Blowing

Leading edge blowing (LEB) is a form of flow control that has recently been investigated by Weiland and Vlachos for reduction of blade vortex interaction. The most common instance of blade vortex interaction is found in helicopter rotors. The tip vortex generated by a blade convects downstream until a subsequent rotor passes. The interaction of the tip vortex with the advancing rotor blade causes unsteady forces on the blade. The worst case of this interaction occurs when the vortex and blade span are parallel. The noise radiated due to this type of interaction relates directly to the distance between the airfoil and the vortex. Weiland cites the simplified two-dimensional noise radiation model as

$$p\left(x,t^{*}\right)\approx\frac{\Gamma Ll}{\rho_{\infty}d^{2}}, \qquad \textbf{2.1}$$

where *d* is the distance between the airfoil and vortex.[25] Since the radiated noise is inversely proportional to the square of the offset distance, increasing the offset distance will reduce the noise generated.

The LEB method involves projecting a continuous jet of fluid in the opposite direction of the incoming fluid. This effects the blade vortex interaction in two different ways. For vortical structures that approach the blade directly in line with the leading edge, the jet will break up the incoming structures in smaller, less coherent vortices. The smaller vortices have less strength, cause less forcing on the airfoil, and, thus, reduce the amount of radiated noise. However, most of the incoming fluid structures will not strike the leading edge directly. In those cases, the leading edge jet deflects the structures away from the blade, increasing the offset distance.[25]

Weiland et al. tested this method in a two-dimensional experiment in water using the wake shed from a cylinder to provide forcing for a symmetric airfoil. Changing the diameter of the cylinder varied the forcing frequency on the blade. Four jet mass flow rates were tested against the shedding frequencies of 8.4 and 5.8 Hz. At the maximum blowing rate, a 26 dB reduction was reported at the 8.4 Hz forcing frequency. However, this frequency was close to the first natural frequency of the system, so the reductions are more dramatic. At the 5.8 Hz forcing frequency, a reduction of 12 dB was found for the maximum blowing rate.[25]

This flow control technique was originally formulated for reducing the effects of blade vortex interaction. It has not previously been applied to the situation of a three-dimensional wake shed from a rotor. Weiland's work concentrated on the treatment of large coherent vertical structures that were shed at very low frequencies. The technique was not tested at the higher frequencies that will be shed from a rotor. The rotor speeds used in these experiments yielded blade passing frequencies between 50 Hz and 240 Hz, several times larger than those tested by Weiland. In addition, the flow field created by a rotor does have fundamental differences from that created by a cylinder in crossflow. This research will investigate the extent to which this technique will function in the more complicated rotor wake flow.

3 Experimental Assembly

From research, three different flow control strategies were designed. In order to test their effectiveness, an experimental platform was designed and manufactured for the testing these strategies in a realistic flow field. This experimental assembly incorporated a single blade to approximate the exit guide vane and an upstream rotor. This chapter will describe the test assembly and the instrumentation that was used to measure the effects of flow control on the rotor-induced flow field. Also, a detailed description of the flow control geometries will be presented.

3.1 Assembly and Facility Overview

All of the full assembly tests were performed in the Virginia Tech Engineering Science and Mechanics water tunnel. This tunnel, shown in Figure 3.1, is a recirculating low speed water tunnel with a 2' x 2'x 6' open top test section. The maximum freestream speed available is one meter per second. A manually controlled variable speed inline pump circulates the fluid through the clear-walled test section. The open-top test section allowed the assembly to be suspended into the center of the test section from the top.

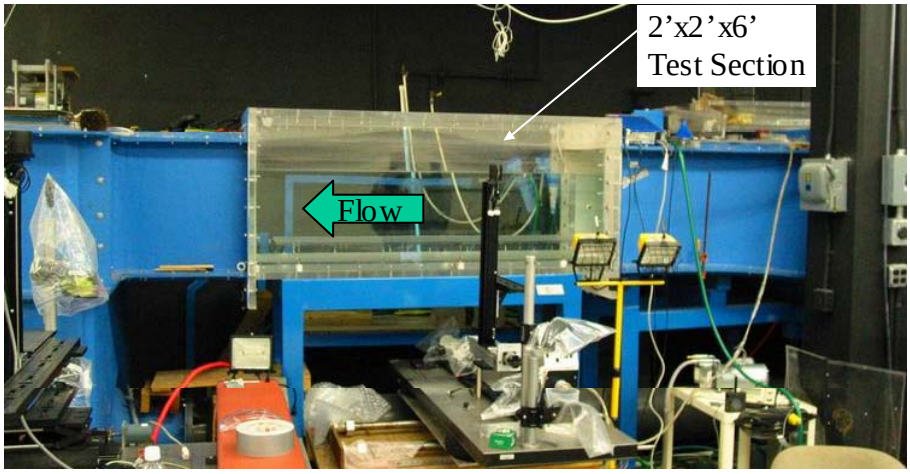

Figure 3.1: Virginia Tech ESM water tunnel.

The purpose of these experiments was to determine the effectiveness of different flow control methods on reducing rotor-induced structural vibrations on downstream objects. In order

to approximate this situation, an assembly was designed that positioned a single exit guide vane (EGV) downstream of a rotor. The EGV was then instrumented to yield vibration measurements. Although in an actual turbomachine there are multiple EGVs, the flow field is axisymmetric around a center axis; thus, the change in induced vibrations could be measured using only one EGV. Figure 3.2 shows a CAD model of the entire assembly as mounted in the water tunnel. The apparatus was divided into two separate parts, the EGV assembly and the rotor assembly. This allows flow control methods to be applied to both the rotor and the EGV easily and independently of each other. Each part will be examined in detail in subsequent sections.

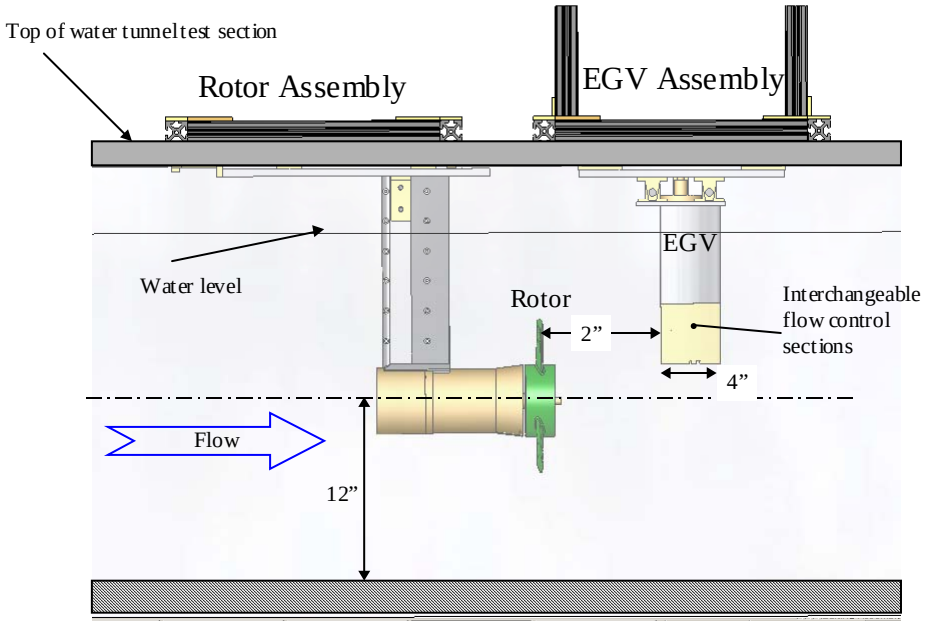

Figure 3.2: CAD model of experimental assembly. The apparatus was separated into to parts, the rotor assembly and the EGV assembly in order to simply application and installation of different flow control concepts.

3.2 Rotor Assembly

The rotor assembly, shown in Figure 3.3, consists primarily of a custom Moog G413-8xx AC servomotor that is used to drive the propeller. The servomotor was custom built with a water-resistant shaft seal and encased in an aluminum housing to prevent water damage to the electronics. The motor is suspended into the flow via a foot long strut that also houses the motor cables. Unfortunately, the strut does disturb the flow directly in front of the propeller. In order

to minimize the effect of the shedding from the strut, the structure was streamlined as much as possible.

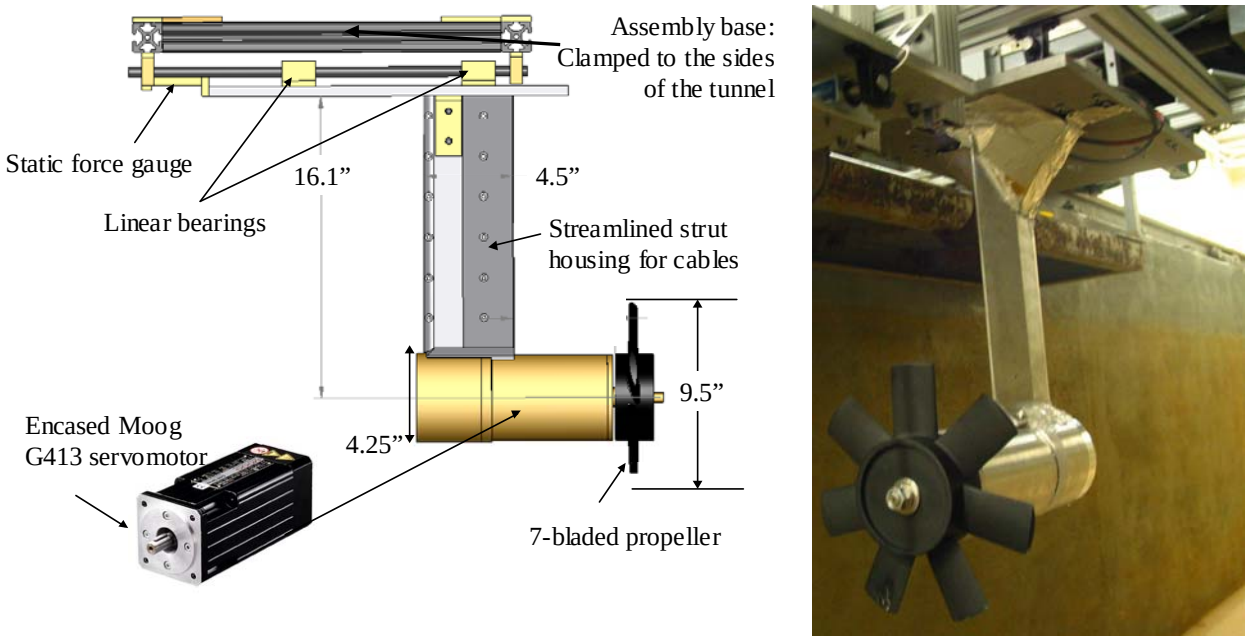

Figure 3.3: (A) Model of the motor assembly. (B) Picture of the manufactured motor assembly.

The entire motor and strut structure attaches to a set of rails via linear bearings. The linear bearings allow for the thrust of the propeller to be measured using a Futek LSB300 25 lb S-beam tension/compression force gauge. The force gauge is mounted between the assembly base and the motor assembly. When the propeller turns it creates a thrust force that is transmitted through the motion of the linear bearings to the force gauge. In addition to the thrust measurement, the motor is equipped with feedback that gives the torque demand and the actual motor speed. This gives a direct measure of the performance of the motor-propeller system.

Two propellers were used in this experiment; a 7-bladed plain propeller and a 3-bladed propeller equipped with flow control. Scott Black at the Naval Surface Warfare Center (NSWC) Carderock Division initially designed the blade geometry for both propellers.[26] Each propeller was then adapted to the specific task. For the EGV flow control tests, the 7-bladed propeller was used in order to test the response at high blade passing frequencies (BPF), see Figure 3.4A, whereas the three blade propeller was implemented for the flow control tests since the blades

were equipped with thicker trailing edges. Both propellers were manufactured using stereolithography (SLA) by Solid Concepts, Inc out of SOMOS 11120 resin. Scott Black provided an estimate of the torque demand for the propeller when the designs were completed. Using the torque feedback from the motor, the actual torque curve for the motor was determined experimentally. Figure 3.5 shows a comparison between the analytical torque curve and the experimental data. For the lower speeds that were used in this experiment, the analytical curve matches the experimental curve very well. However, the motor speeds available for experimentation were limited because when running the propeller, cavitation was observed at the higher speeds. Between 1800 and 2000 rpm sheet cavitation began to form at certain locations along the blade surface. As testing progressed the collapse of the vapor bubbles began to damage the propeller, shown in Figure 3.4B, thus the higher speed test cases were removed from the test matrix. The 3-bladed propeller was manufactured using the same methods and is outlined in more detail in Section 3.4.3.

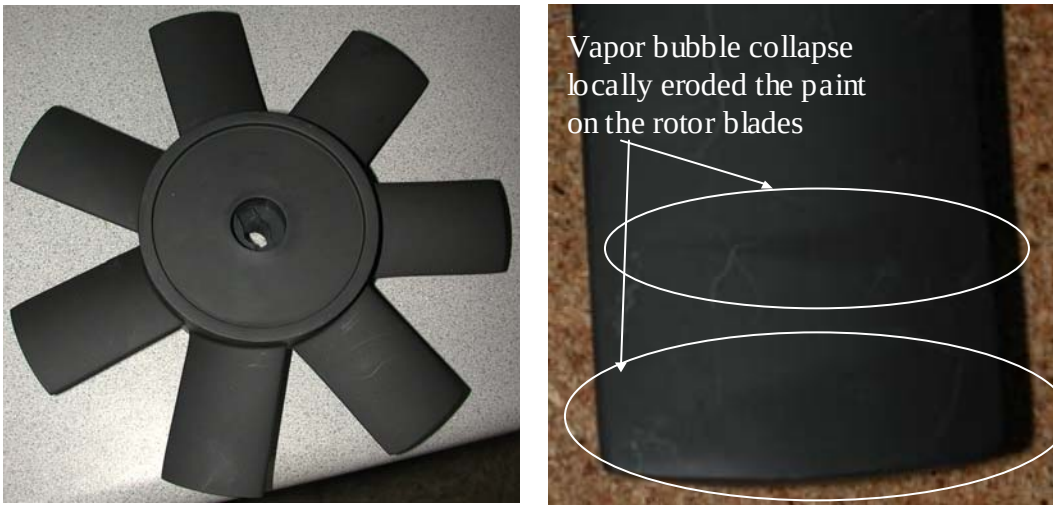

(A) **(B)**

Figure 3.4: (A) The 7-bladed B2 propeller designed by NSWC before testing. (B) The cavitation began to erode away the paint on the propeller blades at the higher speeds.

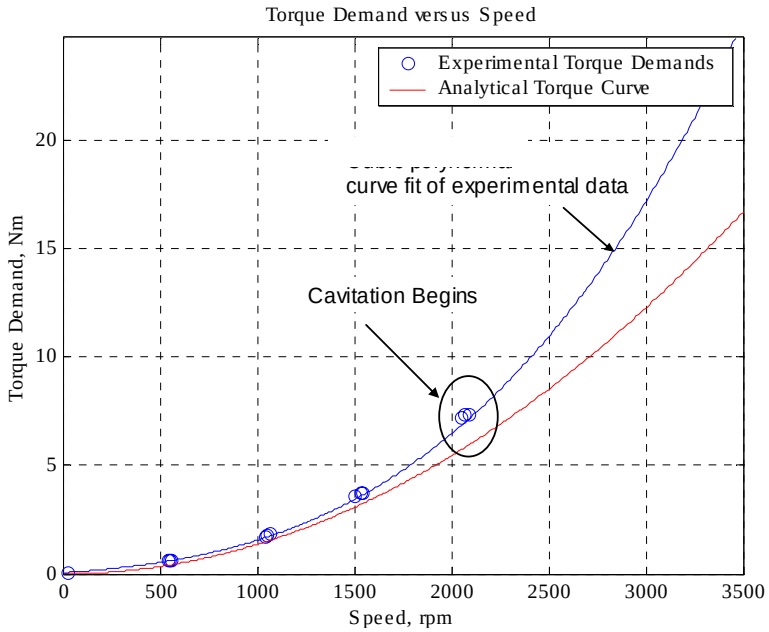

Figure 3.5: Ideal and experimental torque curves for the B2 7-bladed rotor used in the EGV flow control experiments

3.3 Exit Guide Vane Assembly

The exit guide vane (EGV) assembly contained the majority of the instrumentation in these experiments. The blade was designed to allow for different flow control geometries to be installed in the lower half. In addition, instrumentation such as strain gauges and a force gauge was installed on the EGV and its mounting structure. These measurements were calibrated using a modal analysis. This section outlines the overall geometry and instrumentation of the EGV and the modal analysis results.

3.3.1 EGV Assembly Geometry and Instrumentation

The EGV assembly, shown in Figure 3.6, consisted of a single blade mounted in a cantilevered arrangement from a mounting structure. The blade was mounted such that the blade chord was parallel to the tunnel freestream flow. However, due to the rotational effects of the rotor, this does not mean that the blade had a zero angle of attack to the impinging flow. The actual flow angle of attack varied radially with respect to the twist in the rotor blades and could not be measured directly using the available instrumentation. The blade consisted of a 6.5 in

long aluminum base that was machined into an airfoil shape to match the flow control sections. The 4 in long flow control sections screwed onto the end of the aluminum base giving the blade a total span of 10.5 in. The airfoil section was chosen to be a thin symmetric airfoil with a sharp leading edge. The exact airfoil section was taken from data given by the Navy on a prototype propulsor.

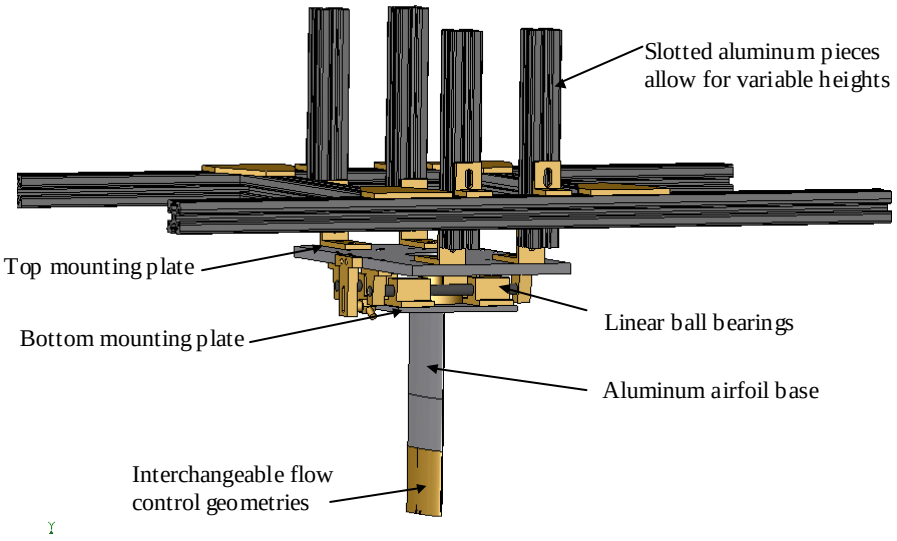

Figure 3.6: Computer model of EGV assembly.

Since the acoustic radiation is directly related to the force imparted on the blade, the forcing due to fluid-structure interaction had to be measured. As with any three-dimensional system there are three forces and three moment components acting on the blade. In order to fully quantify all six of these forces and moments a multiaxis force balance is required. However, given the small forces that were present in the system, a high-precision force balance was prohibitively expensive. The other measurement option was to configure the mounting structure such that a single force on the blade could be measured. This was achieved by mounting the blade on four linear bearings that allowed motion only in one direction, see Figure 3.7. The degree of freedom allowed by the linear bearings was parallel to the direction of the lift force on the airfoil. However, the PCB 208C01 ICP dynamic force gauge only measured the dynamic component of the lift force. The gauge had a minimum measurable frequency of 0.01 Hz, so the steady lift force could not be measured. The sensitivity of the gauge coupled with the resolution of the data acquisition system, yielded a total sensitivity to +/- 0.4 N according to the manufacturer's specifications.

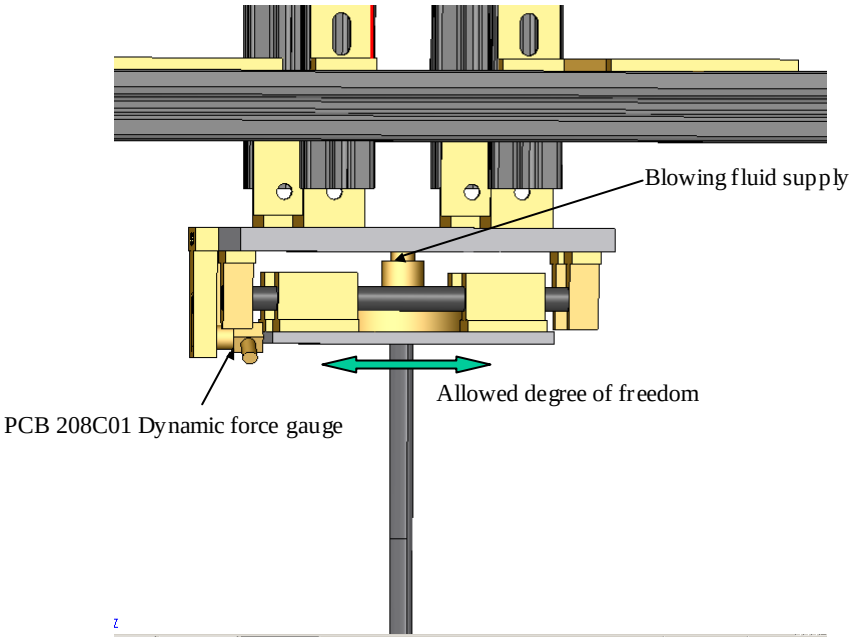

Figure 3.7: Linear bearings isolate the lift force on the airfoil. The dynamic force gauge measures the dynamic changes in lift force caused by the unsteady fluid interaction.

In an ideal assembly, the entire structure would be completely rigid. A rigid system would mean that the fluid forcing would not cause any structural vibrations. Structural vibrations could increase the forces measured by the force gauge, thus corrupting the forcing data. In order to monitor the structural vibrations of the blade strain gauges were mounted on the blade surface. The TML waterproof strain gauges, shown in Figure 3.8, were encapsulated with preattached lead wires to prevent water damage. The coating on the strain gauges was 1.5mm thick. The thickness of the gauges meant that they could not be installed on the flow control sections without causing flow disruption. However, the rotor wake did not significantly impact aluminum base, see Figure 3.2, since the span of the rotor blades was less than that of the flow control sections. Thus, the strain gauges were installed on the aluminum base where there was less flow field impact.

Early tests showed that the structural vibrations were not limited to the blade, so two Wilcoxon Model 752-2 waterproof accelerometers were installed on the top mounting plate of the assembly, see Figure 3.9. These accelerometers measure both the force transmitted through the structure from the blade as well as the vibrations coming from the water tunnel itself. Although rubber was put between the tunnel walls and the EGV assembly to dampen the transmitted vibration, some of the vibrations from the tunnel could still be transmitted to the

structure. Any reductions in forcing due to the flow control should also appear in the accelerometer measurements.

Figure 3.8: Four strain gauges were installed on the aluminum airfoil base. Each was assigned a number in order to expedite the data processing.

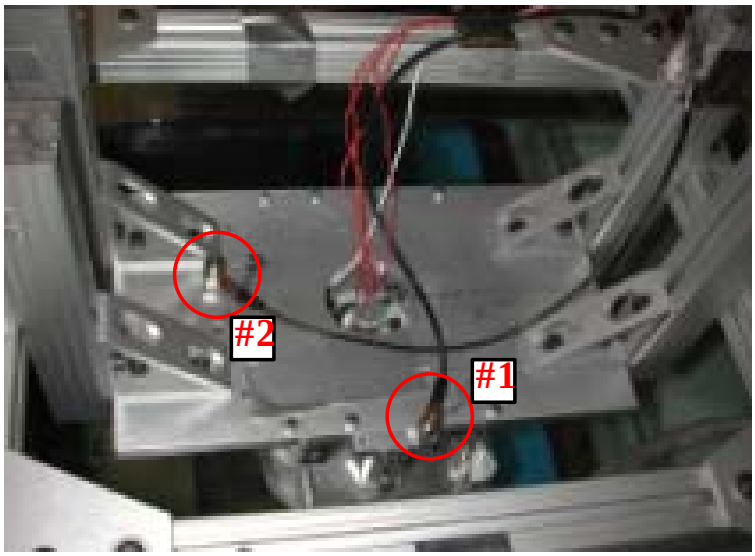

Figure 3.9: Two accelerometers were attached to the top mounting plate to measure the structural vibrations of the entire system.

3.3.2 Structural Analysis of EGV Assembly

Given the coupled structural dynamics of the EGV assembly, the entire assembly influences the behavior of the force transducer. This means that the system needs to be calibrated in order to determine the relationship between input forces and the force measured by the force gauge. The relationship is not necessarily one to one because of the structural resonances present in the system. To find the frequency response function between an input

force and the force gauge, a roving hammer test was performed on the assembly. The roving hammer test required mounting one of the accelerometers on the blade itself, while the other instrumentation remained mounted in the positions outlined in Section 3.3.1. The blade was then struck with an impact hammer while the output force, acceleration, and strain were measured. The impact hammer was equipped with a force gauge that measures the force of the impact. To measure the system response to forces at different input locations, the blade was divided into a 65 point grid with input forces applied at each grid point. Figure 3.10 shows the grid used to locate the input forces and the accelerometer located on the blade. Each grid point is referenced by the chordwise (C-axis) and lengthwise (L-axis) position.

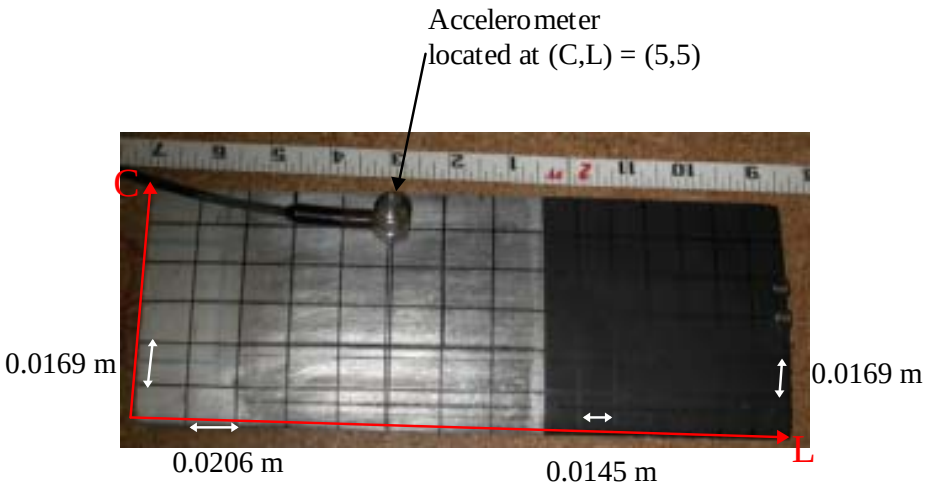

Figure 3.10: The EGV was sectioned into a regular grid for the modal analysis. Each grid point is referenced by chordwise (C) and lengthwise (L) position.

For each point, the blade was struck five separate times and the output response measured each time. The measured responses from each repetition were compared to yield the coherence of the data at that point. The coherence gave an indication of how well correlated the measurements were with each other; coherent measurements have values close to one, while incoherent measurements have values approaching zero. Analysis of the coherence measurements across the response frequency range indicates in what bandwidth the force and strain measurements can be considered reliable and repeatable. Figure 3.11 shows the coherence between the input force hammer and the output force gauge for a particular point. Sharp, localized drops in coherence indicate a resonant frequency and a roll-off indicates the bandwidth limit of the transducer. Each test point showed at least the same, if not greater, bandwidth of

response. The coherence plots for additional test points are shown in Appendix B; comparing the test points yielded a minimum bandwidth of 0 to 500 Hz. Although, the system does not have usable high frequency response, it does yield reliable data for the all of the desired blade passing frequencies (BPF) and their first harmonics.

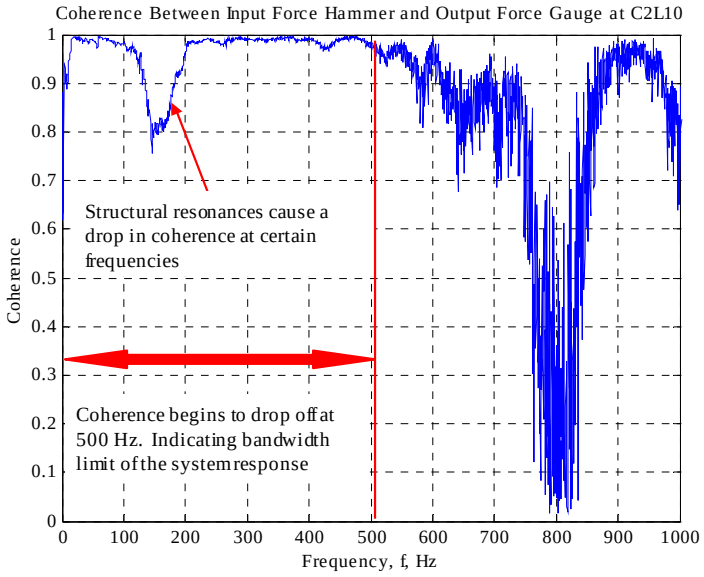

Figure 3.11: Coherence between the force hammer and the force gauge at (C,L) = (2,10). This plot shows that the bandwidth of reliable data to be 0 to 500 Hz.

The modal tests also yielded information on the frequency response function between the input force and the output measurements. The most important frequency response function was computed between the force hammer and the force gauge. This frequency response function outlines how well the force gauge measurement captures the actual input force. Figure 3.12 shows the frequency response function from a given input force location. The structural resonances cause the output force to be larger than the input force due to the vibration of the system. The first three resonances occur at 30, 106, and 160 Hz, this first resonance dominates the frequency response function. However, despite the peaks that occur in several places in the frequency response function, the ratio of input force to output force never drops below one for frequencies below 500 Hz. This means that within the measurement bandwidth the system only amplifies forces, it does not dampen the response at any frequency. The frequency response functions for each input location are shown in Appendix B; the frequency response functions exhibit the same trends without respect to the input force location.

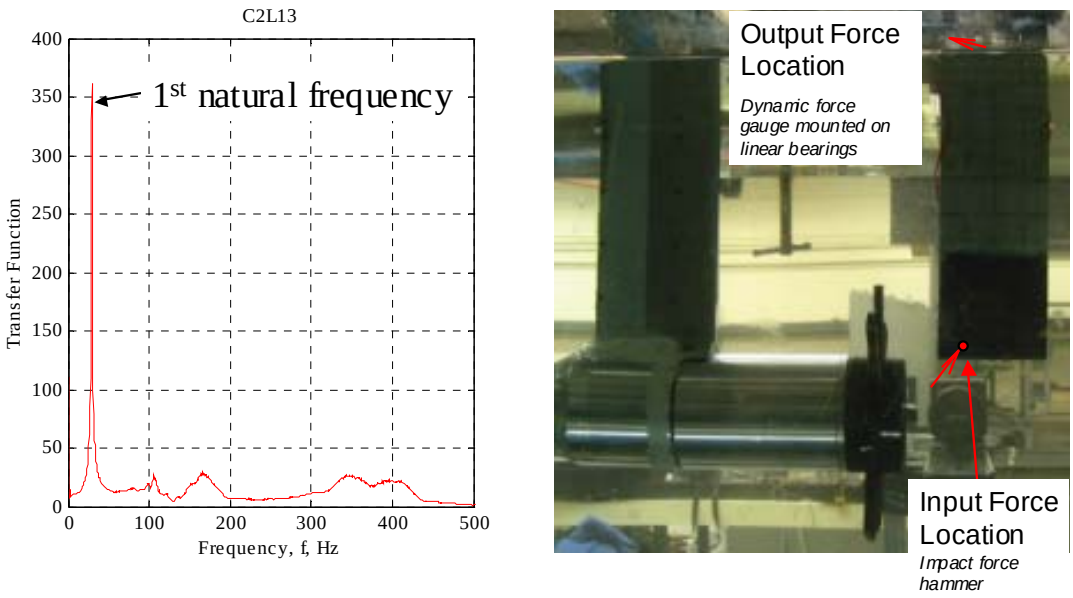

Figure 3.12: The frequency response function ($F_{output,\ gauge}/F_{input,\ impulse\ hammer}$) between the input force, measured by a PCB Impulse Hammer, and the dynamic force gauge mounted at the top of the EGV. The picture shows were the impulse was applied to the EGV in order to get the shown frequency response function.

3.4 Flow Control Configurations

There are two main methods of flow control that were tested in this research. The first was to add active flow control to the EGV to reduce the effect of the impinging wake. The active flow control on the EGV consisted of two different configurations that utilized blowing from the leading edge of the EGV. One configuration involved straight leading edge blowing (LEB) where a jet was propelled from the leading edge of the airfoil into the oncoming flow. The other configuration had a tangentially blowing jet (TB) that was located just downstream of the leading edge and blows along the surface of the airfoil. Particle image velocimetry measurements were taken on both EGV flow control configurations to determine the velocity profile of the blowing jet. The second flow control method was to add flow control to the rotor and reduce the wakes at the source. The rotor flow control uses a self-pumping mechanism to fuel a trailing edge jet for wake filling.

3.4.1 Leading Edge Blowing EGV Flow Control

The leading edge blowing configuration was designed based on a sharp leading edge symmetric airfoil. A single jet is emitted from the leading edge of the airfoil into the oncoming flow. The slot is 1.02 mm thick and along the bottom third of the EGV with a span of 88.9 mm., see Figure 3.13A. The jet was supplied by a plenum located inside the body of the blade, this plenum contained several turning vanes that helped to guide the flow around the right angle from the supply pipe to the slot, see Figure 3.13B. By using vanes to assist in turning the flow prior to the slot, a more even velocity distribution across the slot span was possible. The edges of the slot are very thin, so the vanes also added support to ensure that the slot edges do not deform during operation. Particle image velocimetry (PIV) was used to determine the velocity profile of the jet in quiescent flow. PIV measures the velocity field with a given area, in this case the area immediately surrounding the flow control jets. The PIV measurements of the jet are outlined in Appendix Appendix C. The results of the PIV indicated that the turning vanes used in the plenum did assist in creating a predominantly uniform jet across 75% of the jet span.

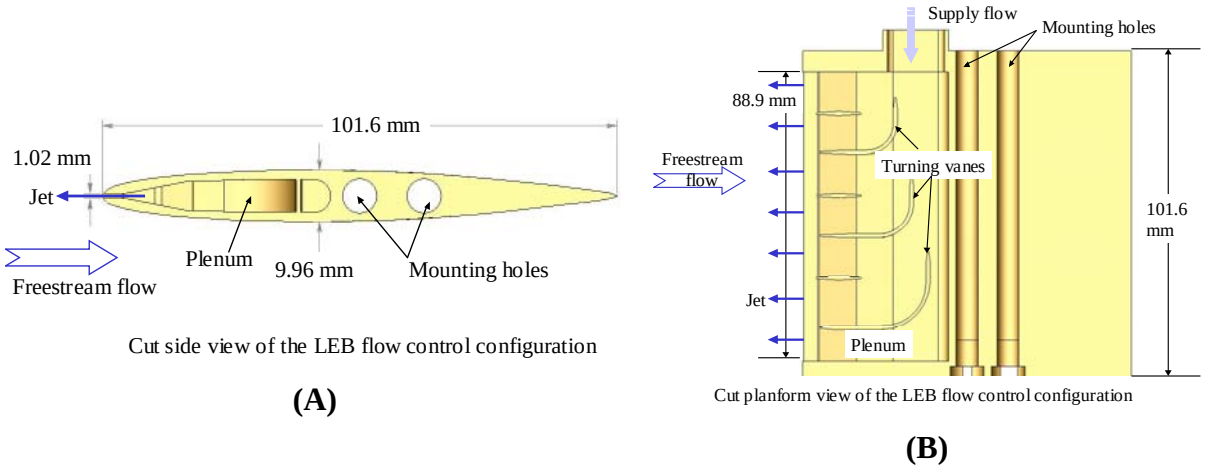

Figure 3.13: LEB geometry. (A) shows the cut side view, (B) shows the cut planform view.

3.4.2 Tangential Blowing (TB) Configuration

The tangential blowing configuration used the same airfoil section as the LEB configuration. The supply flow was split between two symmetric tangential jets that were located 10.26 mm downstream from the leading edge of the airfoil. The slot height of 0.267 mm

means that the maximum jet velocity possible is 2.8 m/s with a flowrate of 8.47 L/min. Figure 3.14A shows a cut view of the side with a magnification of the jet exit; the flow makes an 180^{o} turn from the plenum to the slot, exiting tangential to the blade surface. Like the LEB configuration the slot spanned a length of 88.9 mm along the bottom third of the total EGV span. The turning vanes inside the plenum do not extend as close to the slot as in the LEB case, shown in Figure 3.14B. Having the vanes end earlier helps ensure that the spanwise velocity distribution does not contain wakes from the vanes.

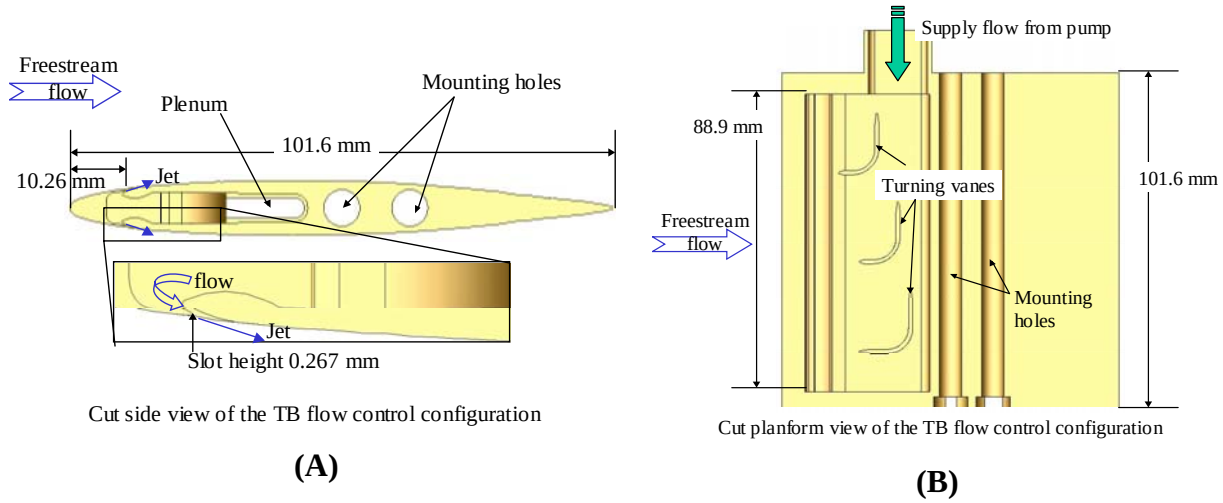

Figure 3.14: TB geometry. (A) shows the cut side view, (B) shows the cut planform view.

The TB configuration presented several problems in both design and manufacture. The intent of the slot design was that the jet would leave the airfoil tangent to the surface and remain attached along the surface of the blade. In order to achieve the desired jet velocities given that the maximum mass flow available was 10 L/min, the slot needed to be very thin. Stereolithography prototypes allow for high precision internal passageways to be manufactured quickly and economically; however, there is a limit to the gap size that the process can resolve. For this blade the slot height is only 0.267 mm in height, due to this small size, the edges of the slot were blocked during manufacture. Using a sharp razor blade, the slot was opened to allow fluid through the entire span. However, this alternation caused the slot to be slightly smaller in height at the opened section. Despite these problems, the overall geometry worked better than expected. PIV measurements of the jet were taken using the same methods outlined in Appendix

Appendix C, analysis of these measurements indicated that in stagnant flow the jet remained attached to the airfoil surface for at least one inch before separating.

3.4.3 Self-Pumping Rotor Design

The rotor flow control is an implementation of trailing edge blowing for the purpose of wake-filling. In order to make the method easier to implement in a small underwater vehicle, the intent was to design a rotor such that no exterior fluid supply was needed. This removes the need for external pumps and fluid supply. The self-pumping rotor design utilized boundary layer suction and ram effects to remove lower velocity flow from the hub of the rotor to pump fluid to the trailing edge blowing slot. The centrifugal force generated by the propeller rotation causes the system to act like centrifugal pump; fluid is pumped through the blade to eject out the tip. Figure 3.15 shows a solid model of the final rotor design. A three bladed propeller with blades designed by the Naval Surface Warfare Center was used as the basis for the design. This propeller has the same airfoil sections as the seven-bladed rotor used in the LEB and TB experiments. However, in order to accommodate the blowing slot, the 3-bladed rotor has a thicker trailing edge with a radius of 1.63 mm. This trailing edge is 5.12 times thicker than that of the 7-bladed rotor.

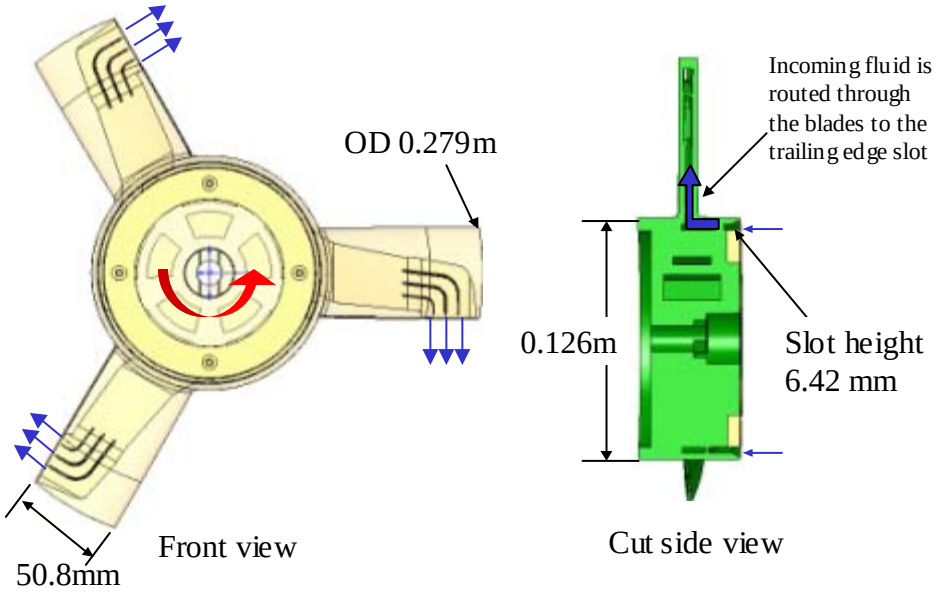

Figure 3.15: Solid model of the self-pumping rotor design.

In order to acquire more pumping power and assist suction into the intake, vanes were added to the intake, these vanes were designed to have the same angle as the root of the rotor blades. Figure 3.16 shows the model of the intake with the five swept vanes. A NACA 0008 section was used to create the vane profile. Due to the differences in propeller design, the results from the two propellers could not be compared with each other. To provide an accurate baseline for comparison, an insert was added that blocked off the inlet. In addition, a ramp was installed to guide flow over the enlarged hub, see Figure 3.16. The propeller was manufactured from SOMOS 11120 using stereolithography. Due to the limitations of the manufacturing method, the interior passageways were not perfectly smooth. Figure 3.17 shows the manufactured propeller, the rotor was left unpainted so that the interior passageways could be easily visible.

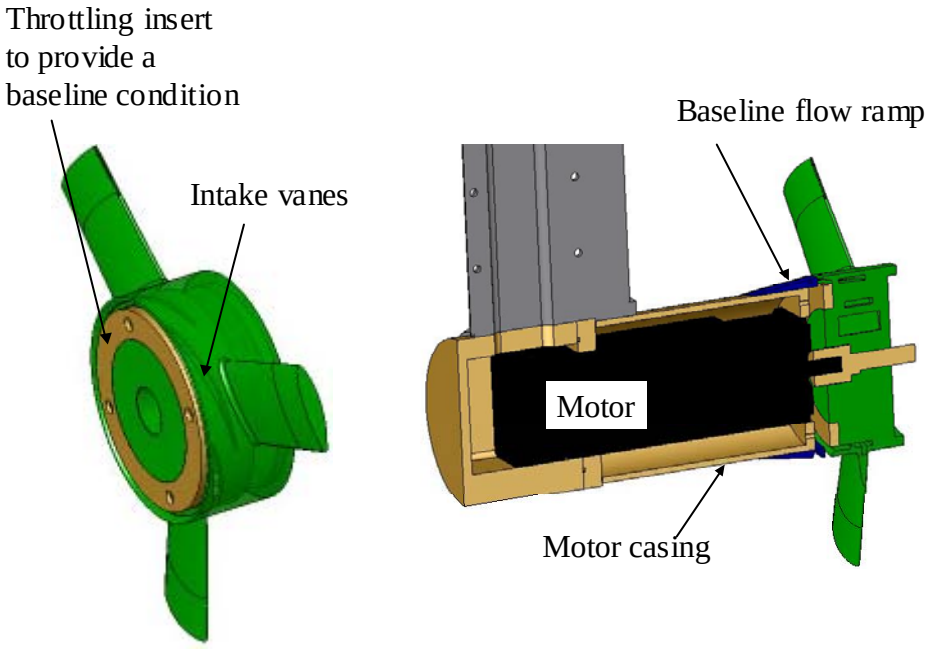

Figure 3.16: CAD models of the final self-pumping rotor design and the installation on the motor assembly. The baseline flow ramp guides the flow past the oversized hub that houses the flow control intake.

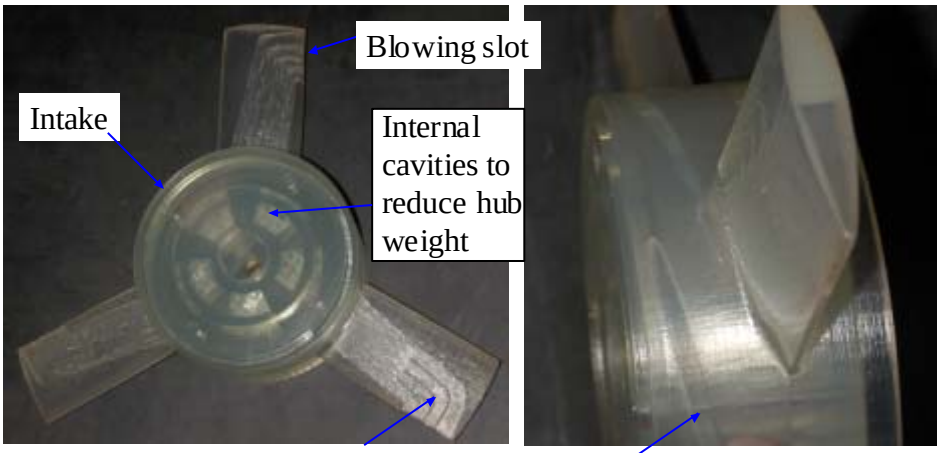

Figure 3.17: Photos of the manufactured self-pumping rotor.

4 EGV Flow Control Results

This chapter outlines the procedures and results from the experimental investigation of the leading edge blowing and tangential blowing configurations for reduction of rotor-EGV interaction noise. The flow control configurations were described in Sections 3.4.1 and 3.4.2. Both configurations were tested at six different flow control blowing rates and a minimum of four rotor speeds. Table 4.1 shows the test matrix for the LEB and TB tests that were performed. In addition, this chapter will explain the validation and calibration experiments that were performed on the assembly. These calibration experiments assist in the determination of the experimental accuracy and the limitations of the measurements.

Table 4.1: Test Matrix for LEB and TB tests

	LEB Configuration					TB Configuration			
Motor RPM	*1200*	*1400*	*1600*	*1800*	*2000*	*1200*	*1400*	*1600*	*1800*
Average Flow Control Jet Velocity [m/s]	0.00	0.00	0.00	0.00	0.00	0.00	0.00	0.00	0.00
	0.44	0.44	0.44	0.44	0.44	0.80	0.80	0.80	0.80
	0.60	0.60	0.60	0.60	0.60	1.10	1.10	1.10	1.10
	0.96	0.96	0.96	0.96	0.96	1.75	1.75	1.75	1.75
	1.30	1.30	1.30	1.30	1.30	2.36	2.36	2.36	2.36
	1.55	1.55	1.55	1.55	1.55	2.82	2.82	2.82	2.82

4.1 Assessing Force Measurement Variability

For this experiment the instrumentation required calibration in order to determine the validity of the measured results. The primary quantity of interest in this experiment is the unsteady fluid force imparted on the EGV as measured by the force gauge due to the unsteady incident flow field. This force provides the most direct indication of the sound radiation from the EGV as given by Equation 1.1. Figure 4.1 shows the orientation of the lift force with respect to the EGV assembly and the incoming flow. The unsteady lift force, F_L, acts perpendicular to the blade span. In addition to this lift force, there is also an unsteady drag force; however, due to thin symmetric blade theory this drag force on a thin blade section is much smaller than the lift force. Thus, drag force would be too small to accurately measure with the available equipment.

The fluctuating lift force occurs across a broad range of frequencies. At certain frequencies the unsteady lift force is larger due to a consistently periodic component of the flow; one of the largest periodic components to the flow is caused by the rotor wakes. As mentioned

in Section 1.2, a main cause of tonal noise is this interactions caused by interaction of the rotor blade with the rotor wakes. Specifically these tones appear at the blade passing frequency and its harmonics. Since the goal of this work is the reduction of tonal noise, the forcing measured at the BPF indicates the desired changes in the radiated tonal noise due to the non-uniform flow from the rotor

The feedback provided by the motor controller allowed the actual rotor speed to be monitored and thus used to calculate the exact BPF. In order to assess the force gauge's ability to accuractely measure forcing at the BPF, autospectrums of the response at different motor speeds were computed. Ideally, these autospectrums should show a peak at the BPF given by the motor speed. Two such force gauge responses are shown with respect to frequency in Figure 4.2 for motor speeds of 1207 and 1817 rpm. As evidenced by the high amplitude of the spectral line at the BPF relative to the broadband noise floor, the force gauge demonstrated the capability clearly measure the forcing at the blade passing frequency for the different motor speeds. The peak response at the BPF was at least two orders of magnitude above the broadband noise floor for all of the test cases, which yields a signal to noise ratio of 20 to 30 dB.

The BPF found from the force gauge autospectrum was within 0.5 Hz of the value calculated from the motor speed. The low frequency response that is seen around 30 Hz likely stems from the excitement of the first structural mode of the assembly. This mode appears at 30 Hz and could be excited by the broadband forcing caused by the incoming flow field as well as the shedding from the motor strut. Although the motor strut is streamlined, it would still shed vortices in its wake; the Strouhal shedding frequency for this shape would be 34 Hz, thus exciting the first mode of the EGV.[27] Also, increase in rotational speed cause larger wakes to be shed from each rotor blade, in the axial frame of reference, this yields an increase in the pressure changes on the blade as the wake passes. The increased pressure change causes a rise in the unsteady forcing on the EGV.[28] As expected, the magnitudes of the BPF forcing increased in direct relation to the change in motor speed.

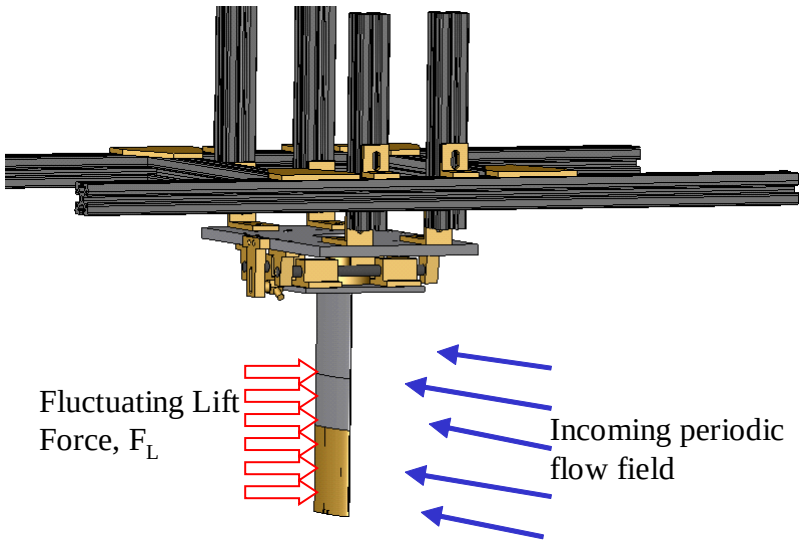

Figure 4.1: Diagram of the force measured by the EGV force gauge.

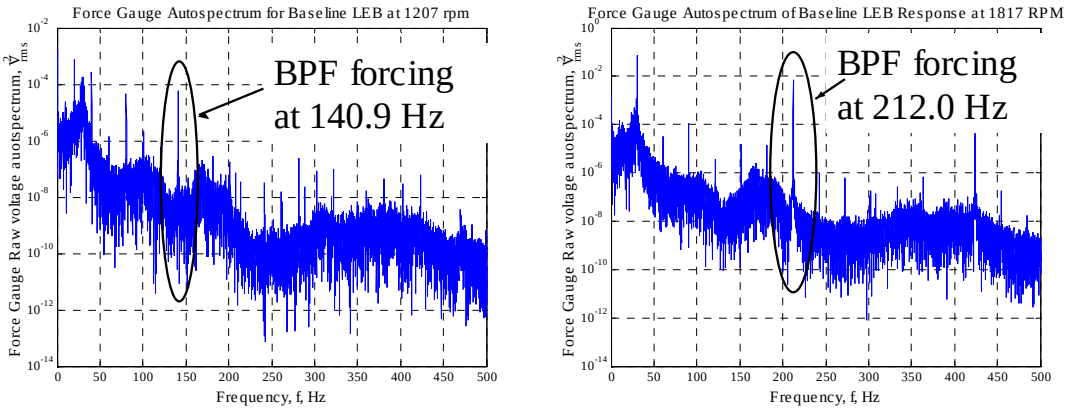

Figure 4.2: Comparison of the force gauge autospectrums for two motor speeds

As was mentioned in Section 3.3, the EGV assembly is not a completely rigid body, thus, structural resonances could exist in the frequency range of interest. The structural analysis conducted on the EGV confirmed that resonances existed within the 100 Hz to 240 Hz range. A structural resonance will amplify the force input at the resonant frequency. Thus, due to the resonances that exist at or near the BPF for each speed, the measured force, F_{fg}, is not equal to the input force, F_L. The experimental data obtained via the roving hammer test outlined in Section 3.3.2 enabled the relationship between the input force and the transducer response to be determined. Specifically, this relationship was characterized in the frequency domain using the H_1 frequency response function estimator,

$$H_1 \equiv \frac{G_{xy}(f)}{G_{xx}(f)} = \frac{F^*_{input}(f)F_{fg}(f)}{F^*_{input}(f)F_{input}(f)}. \quad \textbf{4.1}$$

For three different input locations these frequency response functions are plotted in Figure 4.3 over the frequency range that contained all BPF's considered in this study. As can be seen, the frequency response function, *H*, behaves differently depending on the location of the input force. At structural vibration mode resonant frequencies, 165 Hz for example, the frequency response function indicates that the system amplifies the force that is applied at the location labeled as C1L5, see Figure 3.10. Thus, the structural dynamics of the system effects the magnitude of integrated force measured by the force gauge. This effect can be modeled for a continuum system as

$$F_{fg}(\omega) = \int \int H(x, y, \omega) f_L(x, y, \omega) dxdy\,, \quad \textbf{4.2}$$

where $f_L(x, y, \omega)$ is the unsteady lift force per unit area. Therefore, the entire structure, including the EGV blade, the linear bearing to which the EGV is mounted, the base mounting structure, and force gauge itself all comprise the force transducer system. This implies that any resonances in the structure will effect the force measured by the transducer. Any data taken at the resonance frequencies would then be extremely sensitive to any variations in fluid loading and structural mounting of both the EGV and motor assembly.

These resonances cause the measurements to be dependent on the dynamics of the transducer system. The resonance effects could not be removed from the measured forces without knowledge of the flow field exciting the structure because the flow field does not force the structure at a single point or equally across the surface. This means that the location of the forcing on the blade is not known. The structural analysis showed that the response of the system to an input force is related to the location of the force. Thus, both the magnitude and location of the distributed input force would be required in order to determine the fluid forcing without the resonance effects of the system. However, even though the exact quantity of the

forcing could not be determined, the transducer system is able to distinguish changes in the flow field, as seen from the change in response with respect to motor speed shown in Figure 4.2. Ideally, the EGV assembly should have been designed with a higher structural stiffness in order to move the structural resonances above the highest tested BPF. However, the cantilevered configuration of the EGV limited the amount of structural stiffness that could be built into the system. The cantilevered design was chosen for its ability to readily allow the force measurement to be taken without submerging the force transducer through the use of linear bearings. This meant that a more sensitive non-waterproof force transducer could be used. The aluminum base was incorporated to increase the stiffness of the blade, yet its additional stiffness was of limited effectiveness.

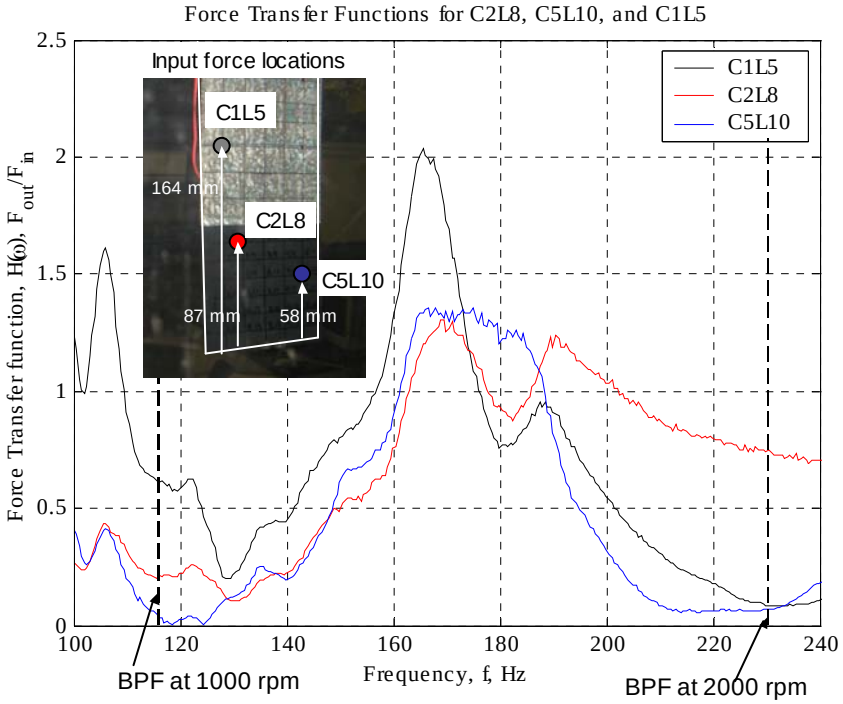

Figure 4.3: The frequency response function, H(w), for three input points on the EGV surface.

In addition to transducer structural dynamics, installation effects were another source of force measurement variability. In order to avoid damage to the motor, the entire motor assembly was removed from the water in between test sets. This removal and reinstallation of the motor could cause a change in the axial spacing between the rotor and the EGV, a change in the flow angle of attack on the EGV due to a rotation of the motor assembly, and a non-radial alignment of the EGV with the centerline of the rotor. The EGV assembly was never moved in order to

provide a common reference point for the repositioning of the rotor assembly. However, the slight changes in position caused an appreciable amount of variation in forcing data from test to test. These effects of these changes can be seen in Figure 4.4 where the baseline BPF forcing magnitude is shown as a function of motor speed for two different test days. The motor was removed and reinstalled between days. This comparison shows that without removing the motor the data points are clustered together for all speeds except the 1600 rpm. Thus, the variability at 1600 rpm is not due solely to the reinstallation of the motor assembly. For the other speeds, the change in motor position has less impact on the repeatability of the measurements.

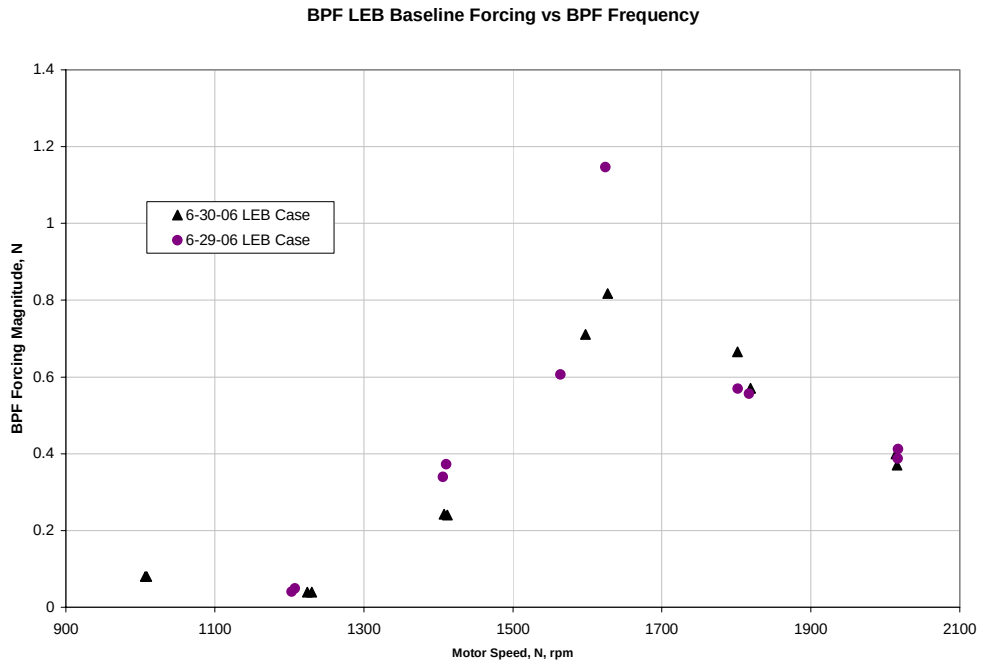

Figure 4.4: Comparison of the Baseline forcing with respect to motor speed for two different days of experiments

Thus, experiments were performed over several days with multiple runsets and motor entries being taken on a single day. A single runset consisted of a set of measurements taken for increasing motor speed followed immediately by the same measurements taken for decreasing motor speed. A motor entry consisted of at least one runset that was conducted without removing the motor from the water tunnel. The difference in measured force at the BPF between different motor entries is shown in Figure 4.5. The variation at the 1600 rpm [BPF = 186 Hz] speed is most likely caused by the resonance that occurs near 185 Hz, the BPF. To determine the variation of each motor speed with respect to the other datasets, the coefficient of variation,

$$CV = \sigma_N / \mu_N \,, \qquad \textbf{4.3}$$

was computed to quantify the variation of each dataset where σ_N is the standard deviation and μ_N is the mean for a particular motor speed, N. These coefficients are shown in Figure 4.6 with respect to the motor speed. The datasets used to create these coefficients span several different motor entries over four days of tests. The CV values indicate that the variation is greatest at 1400 and 1600 rpm. The higher motor speed, 1800 and 2000 rpm, show much less variation. The difference correlates to the structural resonances that appear between 160 Hz and 200 Hz. The BPF for both 1400 rpm and 1600 rpm fall within this resonance band.

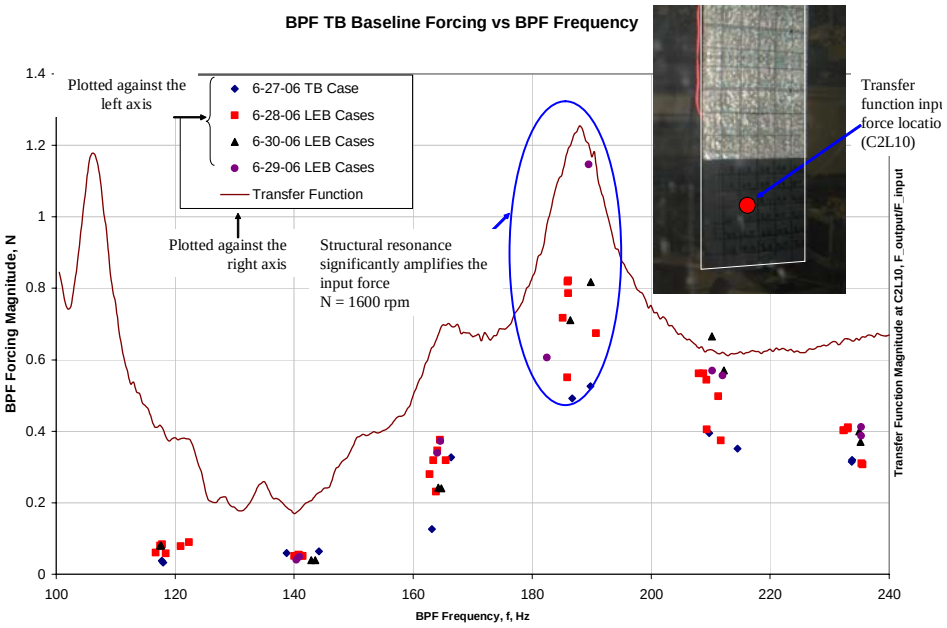

Figure 4.5: The baseline forcing at the BPF over several days compared with one of the frequency response functions between the input force and output force gauge

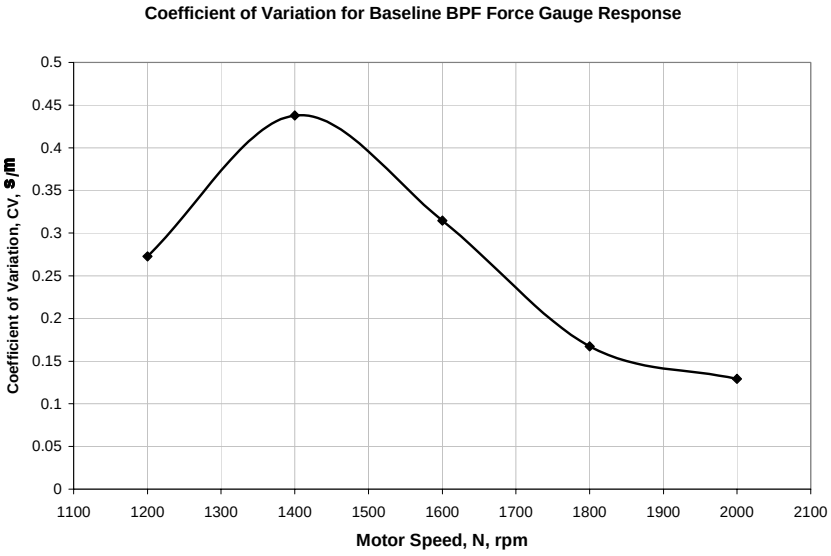

Figure 4.6: Coefficient of Variation for the Baseline BPF force gauge response for different motor speeds. The CV was computed using the data from several different motor entries.

In order to determine if the datasets are statistically likely to have originated from the same conditions, a Student's *t*-test hypothesis test was used to compare the 1200 [140 Hz], 1400 [163 Hz], and 1800 rpm [210 Hz] results. This test, outlined in Appendix F.1, indicates that the probability of the 1200 rpm and 1400 rpm dataset having equal means is less than 0.01%. Similarly the probability that the 1400 rpm and 1800 rpm datasets have equal means is 3.5%. From these tests, the assumption can be made that the data at a given rpm is sufficiently different from the other speeds that trends can be extrapolated.

All of these issues cast doubt on the ability to compare the results between different motor entries. A summary of the main sources of variability and the procedural means used to compensate for the variation are listed in Table 4.2. In particular, to address this effect of these issues on the flow control comparison, the flow control tests for a specific speed were all conducted without moving the motor position. The motor was set at the desired speed and all flow control cases, including the baseline, were tested before moving on to the next speed. In addition, measurements were taken of the forcing caused by the freestream flow of the tunnel without the rotation of the propeller. For the runsets taken within a single motor entry, the freestream circulation of water tunnel was returned to zero and the propeller was stopped. This ensured that the runsets could be treated as separate tests. Before any data was taken with freestream circulation, the water tunnel was allowed to reach a steady state. This method of conducting the leading edge and tangential flow control experiments allowed for the data

comparisons to be made within individual runsets. The conclusions from each runset could then be compared.

Table 4.2: Main sources of variability in the unsteady force measurement and the experimental and procedural means used to address the variability.

Sources of Variability	Means used to address variability
Reinstallation effects of removing the motor between tests	Take flow control case data without removing the motor or changing the motor speed to ensure a test specific baseline a the basis for comparison
Structural dynamics of the system obscure the absolute magnitude of the fluid forcing	Evaluate the effectiveness of the flow control based on the improvement from the baseline, not the measured forcing
Structural resonances amplify small changes at certain motor speeds	Identify which speeds show the most effect due to resonance and not use those speeds as a measure of the flow control effectiveness

4.2 Leading Edge Blowing Configuration Results

The leading edge blowing (LEB) configuration, as was shown in Figure 3.13, consists of a single jet emanating from the leading edge of the hydrofoil. LEB tests involved acquiring twenty seconds of time history data from all of the available instrumentation. The steady measurements that indicate the motor operating conditions, such as the motor speed and torque, were averaged for each test. The time-resolved force gauge, accelerometer, and strain gauge measurements were processed using the Fast Fourier Transform (FFT) algorithm to produce the spectral distribution of each measurement. This allowed the BPF component to be removed and compared with other tests. Recall that the dominant hydrodynamic forcing from the rotor results from the passing rotor wakes, which are sensed by the EGV at the BPF. Figure 4.7 illustrates how a 4 Hz bandwidth was applied to the autospectrums in order to determine the BPF component, each of the spectral lines within this band were summed together in order to give a magnitude of the forcing at the BPF. Comparison of the unsteady EGV forcing at the BPF was used to evaluate the effectiveness of the flow control techniques. Since all of the peaks for each measurement were well separated and the signal to noise ratio approximately 30 dB, it can be conclude with a relatively high level of confidence that the measured force signal content at the BPF and its harmonics can be attributed to the non-uniform flow field shed from the upstream

spinning rotor. The spectrums for select blowing and motor speed cases are shown in Appendix D.

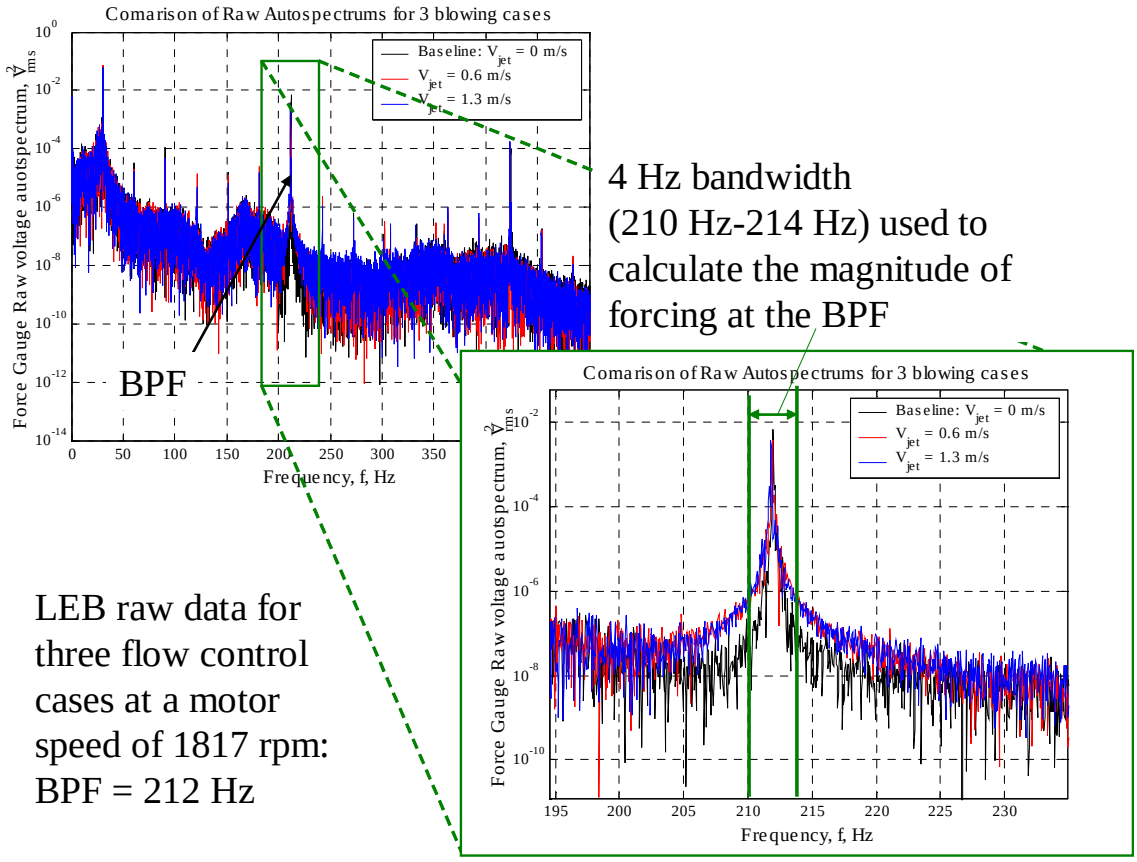

Figure 4.7: A narrow bandwidth was used to calculate the BPF component of the measurements.

The autospectrums computed from the force measurement time histories indicated that the addition of flow control did not affect the spectral behavior of the forcing on the EGV. Figure 4.7 presents a comparison of the autospectrums of the force measurements for the baseline and two jet velocities with respect to frequency. From this comparison it can be seen that the system behavior at the BPF and its harmonics exhibits the same magnitude of response despite the application of flow control. Yet, the shape of the baseline BPF spectral peak is slightly different from the BPF spectral peaks of the flow control cases. This could indicate that the addition of flow control spreads the force across more frequencies, but does not affect the overall magnitude of the response at the BPF. This effect is only present at the 1800 rpm rotational speed. When the flow control is applied to lower motor speeds the jet has no measureable effect on the force gauge frequency response of the system. Alternatively, at speeds

greater than 1800 rpm, the higher velocity flow control jet causes the response at the BPF to be concentrated across a narrower bandwidth. The cause of this motor speed dependent change in frequency response is not currently well understood. The higher rotational speed could cause some separation on rotor blade, thus causing a different wake pattern than is found at lower speeds. In this case, the flow control jet could be affected by the incoming wake, causing the jet to curl back around and impact the EGV at a slightly shifted frequency. This research was not able to determine the velocity profile shed from the rotor experimentally, so the exact nature of the interaction of the jet with the wake is not known. Yet, although the frequency response at the BPF varies, the variation did not significantly impact the total forcing magnitude at the BPF felt by the EGV.

Determining the effectiveness of the LEB flow control on reducing the radiate noise at the BPF required the comparison of the forcing magnitude at the BPF in order to highlight any reduction in tonal forcing. The target reduction in tonal forcing due to the application of flow control was 6 dB. For this comparison, the flow control is defined in terms of the jet velocity. Normally, the flow control effort would be indicated by momentum coefficient; however, in this case there is no available measure of the incoming flow momentum to act as a reference. These jet velocities were determined by the mass flow supplied by the pumps. The effects of this flow control were then demonstrated by a comparison of the BPF forcing at the different test conditions outlined in Table 4.1. The measured unsteady lift force at the BPF is plotted with respect to motor speed and flow control jet velocity in Figure 4.8 in order to indicate the relationship between the force exerted on the EGV by the rotor wake and the leading edge flow control. The data taken at 1600 rpm was discarded due to the resonance effects that were outlined in Section 4.1. It should be noted, that at 2000 rpm the propeller began to cavitate, thus reducing both the rotor performance and the force it was able to transmit to the fluid. This cavitation likely caused the reduction in forcing at the highest speed cases as well as defining the upper limit of the motor speeds to be tested. Measurements at speeds below 1200 rpm were not performed because the rotor wake did not transmit enough force against the EGV to be measured by the force gauge. However, for the speeds greater than 1200 rpm, the system calibration given in Section 4.1 indicated that the system was able to delineate changes in forcing magnitude of at least 1.75 dB. As can be seen in Figure 4.8, the application of LEB flow control does not yield the target reduction in the fluctuating lift force at the BPF.

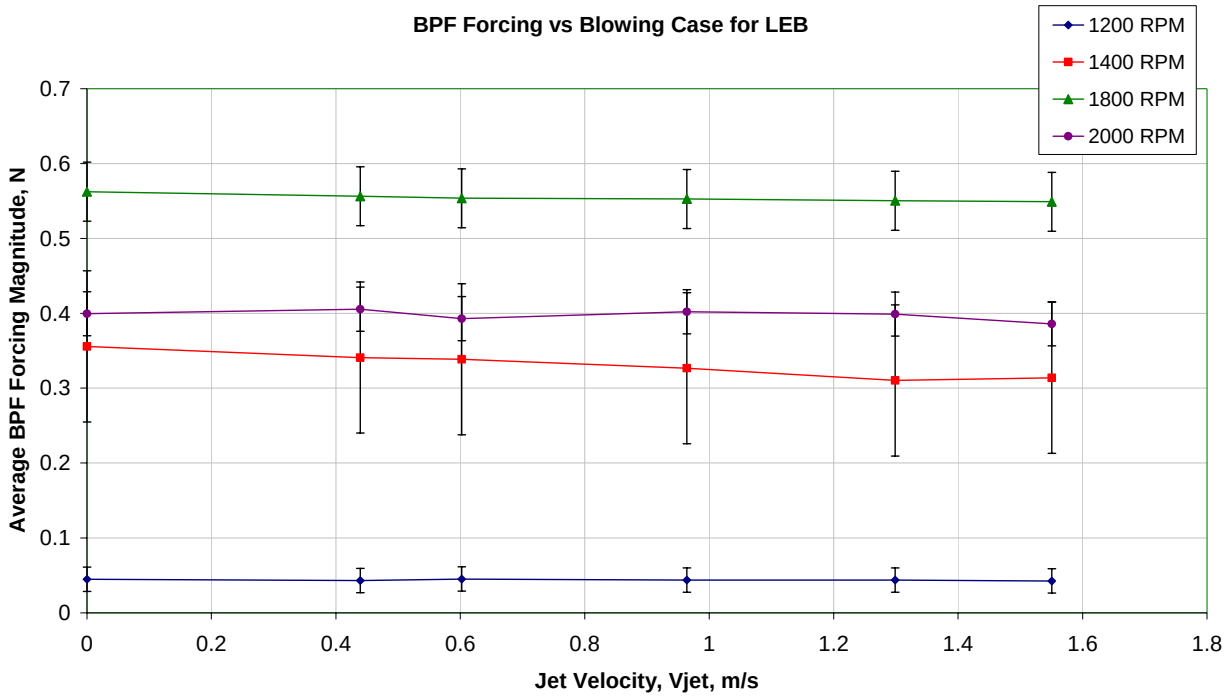

Figure 4.8: Lift forcing at the BPF with respect to the LEB flow control jet velocity and the motor speed.

The error bars shown in Figure 4.8 give the maximum error of the data for each test case. This error is computed using a 95% confidence interval on the data from each motor speed; further details on this computation are outlined in Appendix F.2. It bears mention that the manufacturer's specification rates the sensitivity of the force gauge as 0.4 N. This would imply a larger range of error on the force magnitude as well as invalidating the data collected at the lower motor speeds where the forcing was measured to be very small. However, the results of the hypothesis test referenced in Section 4.1 imply that the existence of a difference between the data at separate speeds could not be rejected. Therefore, the error computed from the data is shown in Figure 4.8 rather than the uncertainty given by the force gauge manufacturer.

Other indicative measurements were performed to confirm the insensitivity of the fluctuating lift to LEB. The accelerometers mounted on the EGV assembly served to measure the amount of vibration transmitted to the base structure. This vibration of the base structure is of significance because in a full propulsor the transmission of structural vibrations from the blades to the casing could also cause sound radiation. For this assembly the measurements from the second accelerometer were available to gauge this vibration; the second accelerometer was mounted at location two on the top mounting plate, see Figure 3.9. In the same manner as the

force gauge measurements, a comparison of the magnitudes of the measured acceleration at the BPF gave an indication of the effect of LEB on the BPF tone transmitted to the mounting base. The average structural acceleration at the BPF in terms of the flow control jet velocity and the motor speed is illustrated in Figure 4.9, thus highlighting any changes in the structural behavior of the system at the BPF due to the application of LEB. The error shown in Figure 4.9 for each motor speed was calculated using the method as referenced previously in this section with the force measurements because the sensitivity of the accelerometer was not known. As can be seen, analysis of the average structural acceleration shows a slight increasing trend in base vibration as the jet velocity increases. This extra vibration could be caused by the internal supply fluid flow triggering vibrations in the supply tube and the interior plenum of the blade. Another cause could be the momentum of the jet increasing the amount of forcing on the blade by adding vorticity to the flow. However, the small accelerations values that were measured were close to the limit of the data acquisition board even with amplification. Therefore, the error in these measurements is of a large enough percentage of the mean data to obscure any changes in acceleration of less than 1.5 dB. Despite this error, the transducer system was capable of measuring the target reduction of 6 dB at the BPF tone. Such a reduction was not seen in the analysis of the data yielded by the accelerometer measurements.

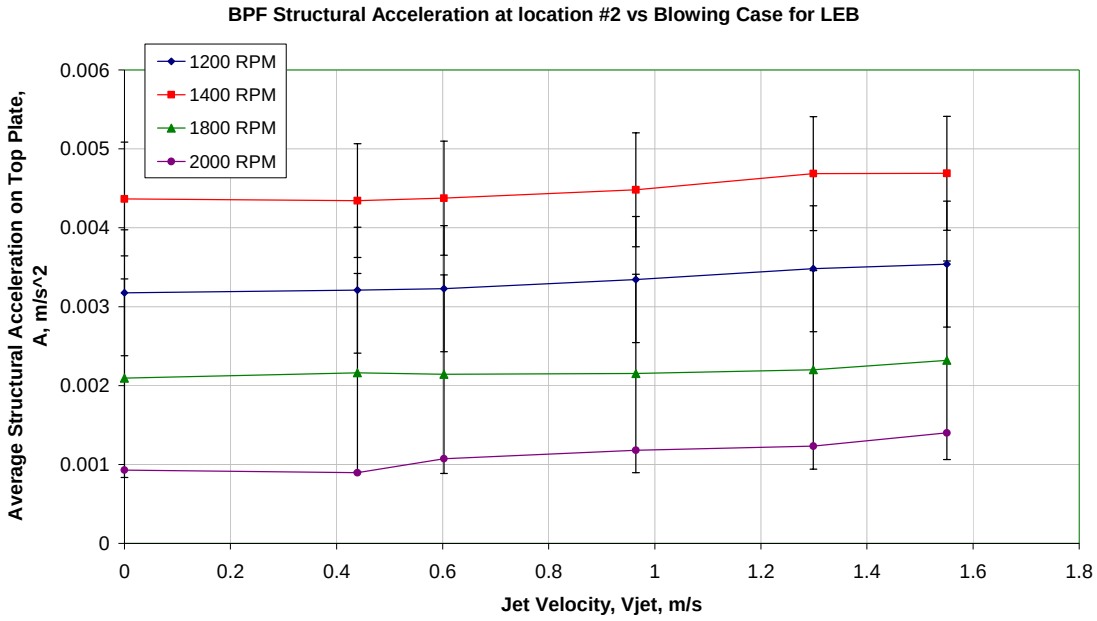

Figure 4.9: BPF structural acceleration at location #2 for LEB flow control

The strain gauge measurements were also intended to indicate the amount of vibration of the blade for a given test case. A portion of the energy imparted on the EGV by the rotor wake excites the vibrational modes in the blade, without necessarily being measured by the force gauge. Thus, a reduction in the strain in the blade could also indicate a beneficial effect of the flow control. The four different strain gauge locations used in this experiment are shown in Figure 3.8. Plotted in Figure 4.10 is the autospectrum of the strain at location one for one baseline and two flow control conditions. As was the case for the force and acceleration data, the strain measurements shows similar spectral responses despite the addition of flow control. The shape of the response at the BPF varies slightly with the addition of flow control, with the maximum flow control case showing a response at the BPF over a smaller range of frequencies than the other flow control and baseline cases. However, the magnitude of the fundamental response remains unchanged despite the addition of flow control. Scrutiny of the autospectrums highlighted an increase in spectral peaks at frequencies outside the BPF bandwidth over the spectral response measured by the force gauge and the accelerometer. This is because the strain gauges were more sensitive to electrical noise than the other measurements due to the unshielded leads that attached to the gauges. In these cases, the 60 Hz frequency was easily avoided because the lowest rotor speed tested yielded a BPF of 140 Hz. Therefore, given the target BPFs for these tests, the electrical noise measured by the strain gauges would not effect the computed BPF strain magnitudes.

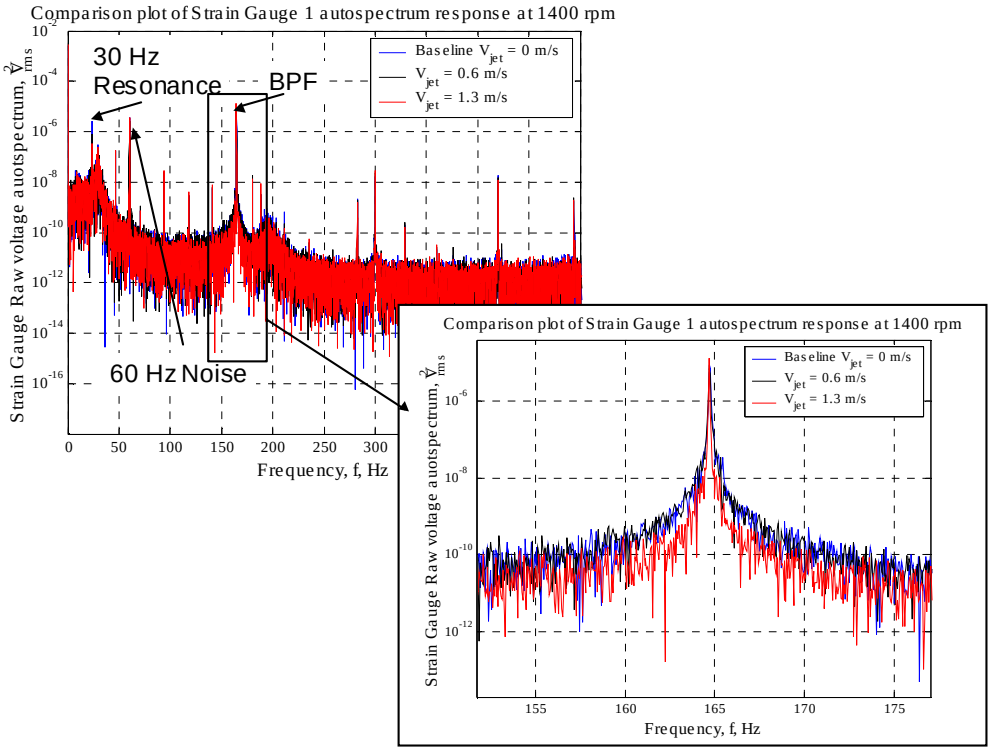

Figure 4.10: Comparison of the strain gauge autospectrums with the application of flow control.

After computing the magnitude of the BPF forcing at each speed and blowing case, the strain gauges analysis showed the same independence of jet velocity with respect to the measured strain. The average strain at the BPF is plotted against the flow control jet velocity in Figure 4.11. As can be seen, the effect of motor speed is a more significant influencing factor on the vibration than the addition of flow control. The computed magnitudes of forcing vary in response to the structural dynamics of the assembly. There are vibrational modes at 160 Hz, thus the 1600 rpm response is higher than the others because the BPF occurs near 160 Hz. The forcing from the rotor wake excites the modes, causing strain in the blade as it twists and bends. Analysis of the other strain gauge measurement spectral responses, shown in Appendix D, also only displays variation with respect to the motor speed. In addition, the magnitudes of the strain gauge response for a particular motor speed are not the same for each strain gauge because the complex movement of the system at the different modes causes the strain in the structure to vary throughout the EGV. For these strain gauge measurements the sensitivity was controlled by the limits of the data acquisition system (DAQ). Using the bit resolution of the DAQ and the properties of the strain gauges, the strain measurement error shown in Figure 4.11 was

calculated; detailed sample calculations can be found in Appendix F.2. Despite this significant measurement error, the strain gauges are capable of measuring changes in strain of at least 1 dB. Taking this limitation due to error into account, the strain does not show the target reduction in BPF tone vibration of 6 dB.

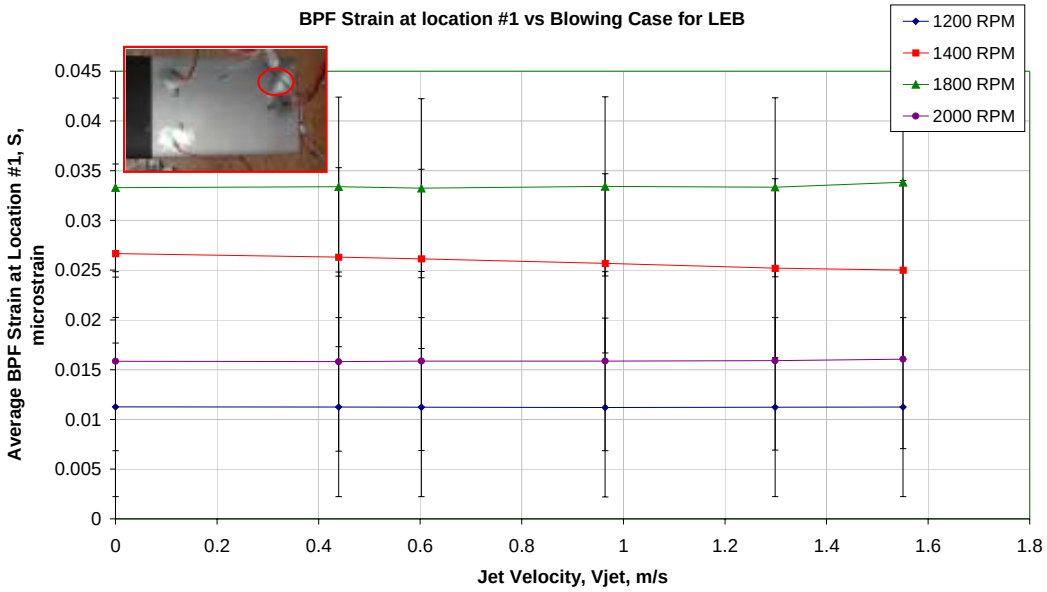

Figure 4.11: Strain at the BPF for strain gauge 1, mounted at the base of the hydrofoil, with respect to the flow control jet velocity.

The data taken in this experiment does not show the improvements found by Weiland et al. for the LEB technique. This inconsistency between the results of the experiment outlined in this work and those performed by Weiland et al. is a result of the fundamental differences in the mechanisms present within the flow. Weiland's experiment utilized a wake from a cylinder in crossflow to provide well-defined coherent structure to force the symmetric airfoil; this provided a periodic forcing at the Strouhal shedding frequency. The shedding frequencies tested were 5.8 and 8.7 Hz; values that are an order of magnitude lower than BPF present in this experiment. A diagram depicting the differences between this experiment and the one performed by Weiland et al. is shown in Figure 4.12. In addition to a higher forcing frequency, this experiment also employed a three dimensional flow field as shed by the rotor; the experiment performed by Weiland was a two dimensional approximation.

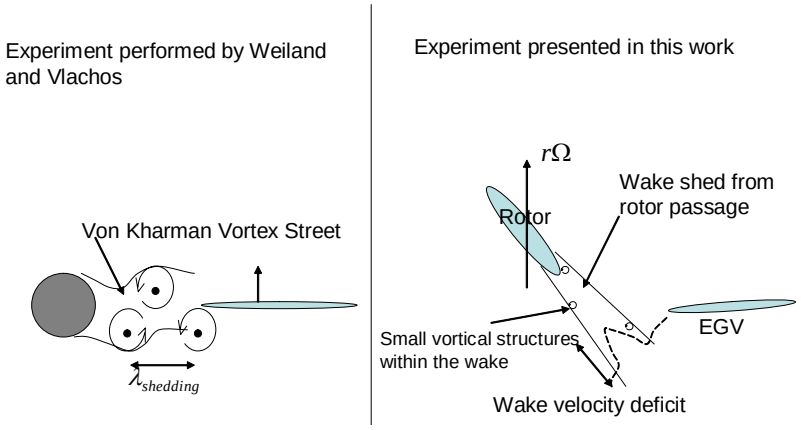

Figure 4.12: Comparison of the experiments performed by Weiland et al. and the experiment presented in this work to analyze the effectiveness of LEB on radiated tonal noise.

The main difference between the two experiments is that in this application over most of the span, the blade is forced by the velocity deficit caused by the rotor passage, not by the passage of coherent structures. The large vortical structures found in a rotor wake are concentrated in the tip region.[29] Uzol et al. found that at the tip of a shrouded rotor the tip vortices frame the rotor wake and dominate the tip flow. However, below 75% of the blade span, the tip vortex effects subside, leaving the wake velocity deficit to be the dominant flow characteristic. Shaw and Balombin also analyzed the characteristics of a rotor wake, finding that outside of the tip region the velocity profiles along the span exhibit the same form of a single velocity deficit corresponding to each rotor blade.[30] However, tests performed by Borgoltz et al. on fan blades in a cascade indicated evidence of some coherent flow structures. Yet, in comparison to the other turbulence within the wake, these structures dissipated quickly along the streamwise distance.[31] This implies that outside of the region affected by the tip vortices, although the rotor wake does contain some vortical structures, structures are not of enough magnitude to be easily distinguished from the velocity deficit. Outside of the tip region, offsetting the small structures in the wake of a rotor does not dramatically effect the forcing on the blade at the BPF because the main cause of the unsteady load is the velocity deficit. The LEB technique is able to break up or offset structures by interaction with the jet; however, the jet does not compensate for the velocity deficit caused by a rotor wake. The tip vortices shed by the rotor could be affected by the LEB technique, since the tip vortices affect approximately 25% of the blade span; however, the experimental EGV force measurements do not indicate that LEB alters the streamwise tip vortex-EGV interaction. Thus, the effectiveness of LEB on reducing

the unsteady load on the EGV is limited and therefore it is plausible that this technique alone would not produce a noticeable reduction in the loading at the BPF.

4.3 Tangential Blowing Results

The second flow control configuration, as depicted in Figure 3.14, was intended operate in much the same way as the film cooling jets used in high-speed turbines. The tangential jets should attach to the blade surface and prevent the wake structures from imparting a force onto the blade. The same experimental process as used for the LEB case was implemented to obtain the system response to tangential flow control. The test matrix for the TB test, see Table 4.1, varied slightly from the matrix for the LEB tests. This is because slight cavitation damage was found on the propeller after the completion of the LEB tests, thus the maximum motor speed used for the TB tests was limited 1800 rpm to reduce the possible damage to the propeller.

Analysis of the frequency response of the force gauge system at the BPF did not indicate any large improvements in the transmitted forcing despite the addition of the TB flow control. The autospectrum of the force gauge response for three TB flowrates are plotted in Figure 4.13. As can be seen, the force gauge measured the BPF forcing and its harmonics below 500 Hz. The magnitude of the BPF and its harmonics are all at least two order of magnitudes above the background noise, yielding at least a 20 dB signal to noise ratio. This indicates that the force caused by the passing rotor wake is strong enough to be adequately measured by the force gauge. In Figure 4.13 it can be noted that the spectral response of the baseline forcing at the BPF is slightly shifted from the two blowing cases. This effect is caused by variations in the motor speed, since the actual motor speed could vary by +/- 2.5 rpm within a particular set of blowing cases thus shifting the BPF frequency by up to 0.29 Hz. This was determined to be the cause because in repeated experiments the shift was not constant between the different trials. Thus, the examination of force gauge measurement frequency response yielded few changes of spectral behavior due to the addition of tangential blowing flow control.

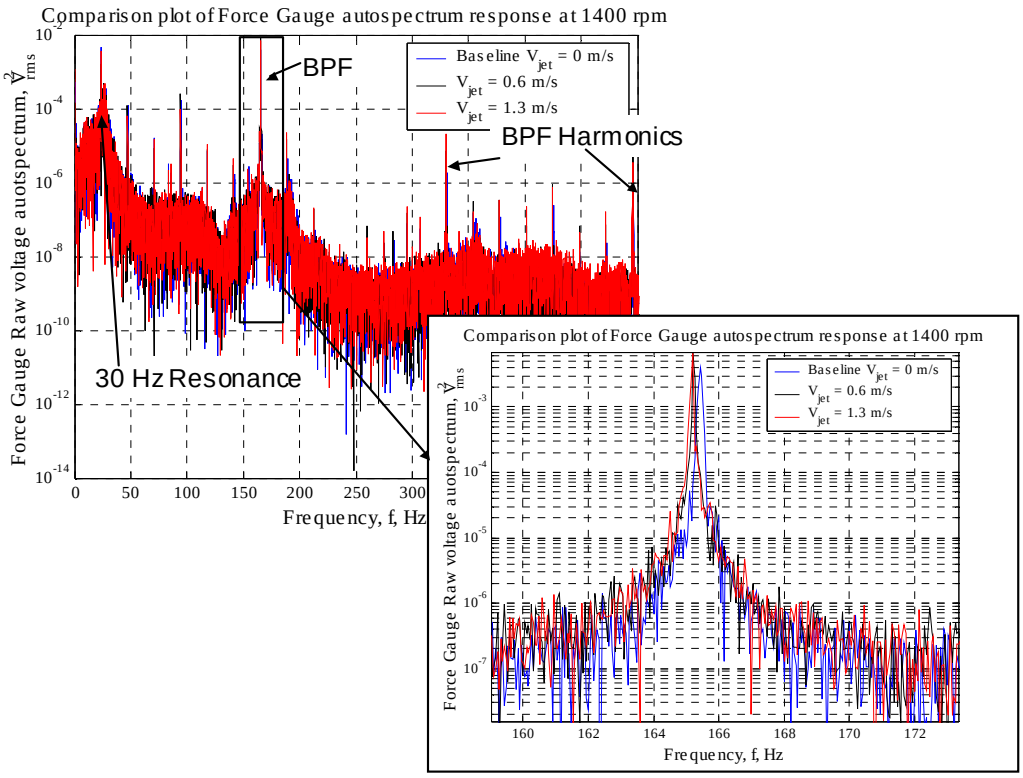

Figure 4.13: Autospectrum comparison of the force gauge response at three of the blowing velocities.

As with the LEB flow control tests, the target reduction in BPF tonal forcing was 6 dB. Using the same methods as outlined in Section 4.2 for the LEB case, the average lift force at the BPF was plotted against the flow control jet velocity in Figure 4.14. From this plot it can be seen that the unsteady lift forcing at the BPF exhibits no measurable changes greater than 1 dB due to the addition of flow control. The change in forcing is more sensitive to the change in motor speed than application of flow control. At a particular speed the forcing did not vary with the application of flow control. The cause for this could be that the main location of the force impact is at the leading edge of the airfoil. In the TB configuration the jet is offset from the leading edge by 10 mm (0.39 in). This leaves a significant area not covered by the flow control. This means that the flow control does not cover the entire area where the unsteady forcing is applied. Thus, the effectiveness of the flow control on controlling the imparted force was limited. Also, as was noted in the analysis of the LEB experiment results, Section 4.2, the wake of a rotor blade only contains large structures in the tip region of the blade. Since the tangential blowing technique is designed to reduce the effect of passing vortices on the EGV, the blowing would have little effect on velocity deficit that dominates the wake flow.

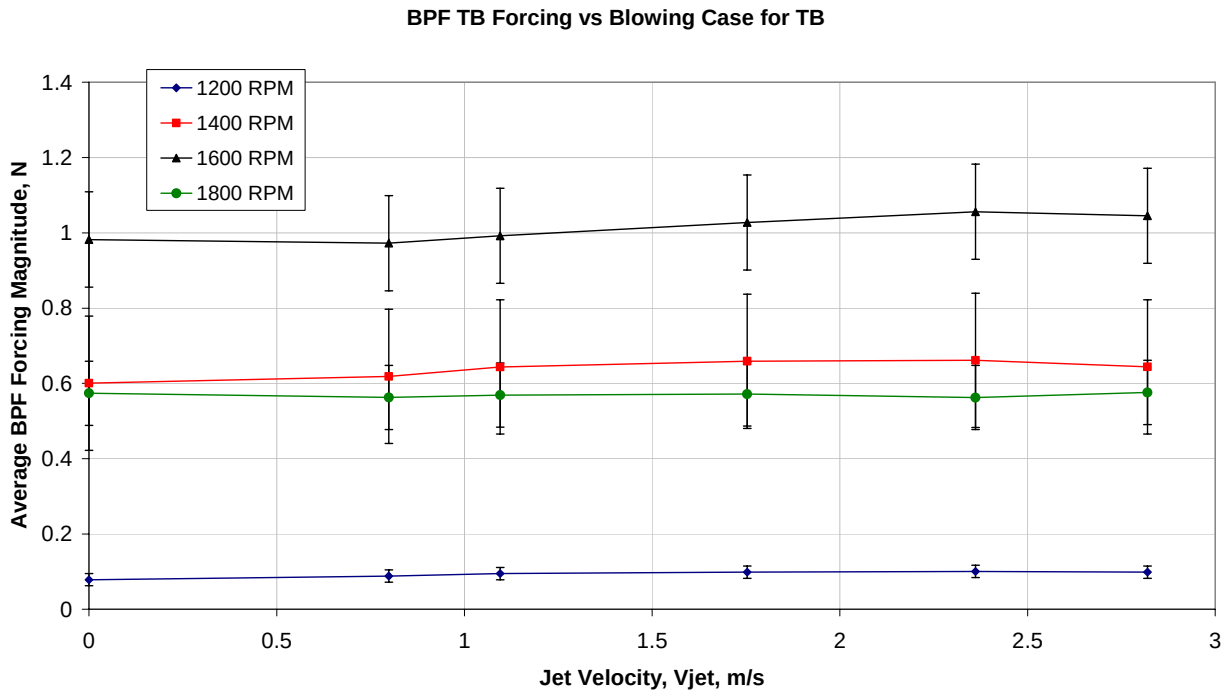

Figure 4.14: Unsteady lift forcing magnitude at the BPF for the tangential blowing configuration.

In order to support the conclusions presented by the force data, the acceleration at location #2 was also measured. These accelerometer measurements at the BPF tone are graphed against flow control jet velocity in Figure 4.15. The acceleration magnitudes computed from the accelerometer measurements did not indicate that the flow control was able to provide a 6 dB reduction in the forcing at the BPF tone. However, when compared to the LEB tests the acceleration measured in the LEB cases was less the TB cases. This difference could be caused by several different phenomena. For instance, the change in the flow control configuration could cause minor changes in the structural dynamics of the system. In order to change the flow control insert on the blade a section of the assembly must be disconnected from the base. A change in the torque applied to the fasteners when the section was replaced changes the structural response of the system, thus causing a change in the measured acceleration. Also, the behavior of the flow control fluid as it passed through the interior passages of the blade could have caused the additional vibration. Yet, even though the acceleration measurements differ from those yielded by the LEB tests; the acceleration remained unchanged from the baseline with the addition of TB flow control.

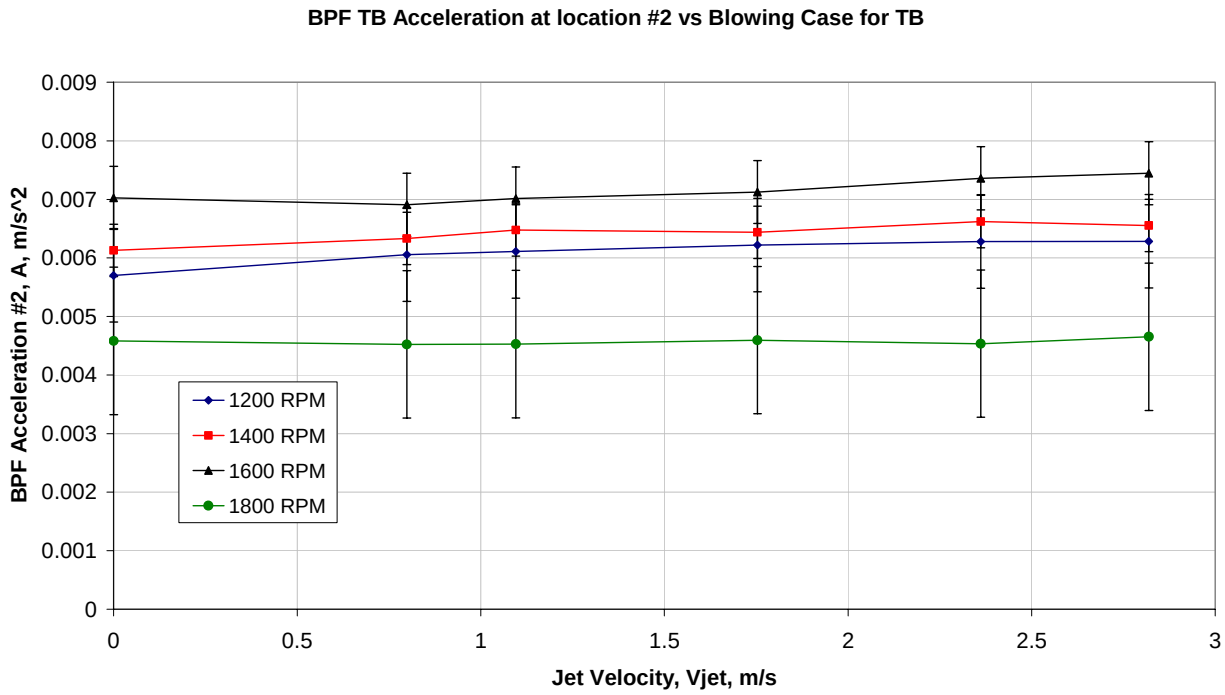

Figure 4.15: BPF Structural acceleration at location #2 for the tangential blowing configuration.

The remaining measurement available to confirm the force measurement results was the four strain gauges mounted on the EGV, the locations of the strain gauges are shown in Figure 3.8. The average strain with respect to flow control as measured at location one is plotted in Figure 4.16. This plot indicates that the strain increases with the increase in speed, caused by the excitation of different structural resonances at the different BPF as well as the increase in forcing on the EGV by the increase in rotor wake deficit. The resonance effects at 1600 rpm also increase the magnitude of the system response. Yet, while the system responds to the changes in BPF that correspond with the change in speed, the strain gauge data does not exhibit a significant trend with respect to the application of flow control. The full strain gauge measurement frequency spectrums used to compute the BPF magnitude for selected example cases, as well as the average BPF forcing for the other three strain gauges, are shown in Appendix D. These strain gauge frequency spectrums indicate that the tangential blade configuration has a similar response to the application of flow control as the LEB configuration. However, as noted in the accelerometer data, the magnitude of the measured strain does differ from the LEB data due to unavoidable minor changes in the mounting structure. Despite this, the system did not show the desired reduction in blade vibration needed to rule the TB flow control as effective in reducing

vibration. Thus, using all available measurement tools, the application of tangential blowing flow control was not able to yield a 6 dB reduction in the force exerted on the EGV in this assembly.

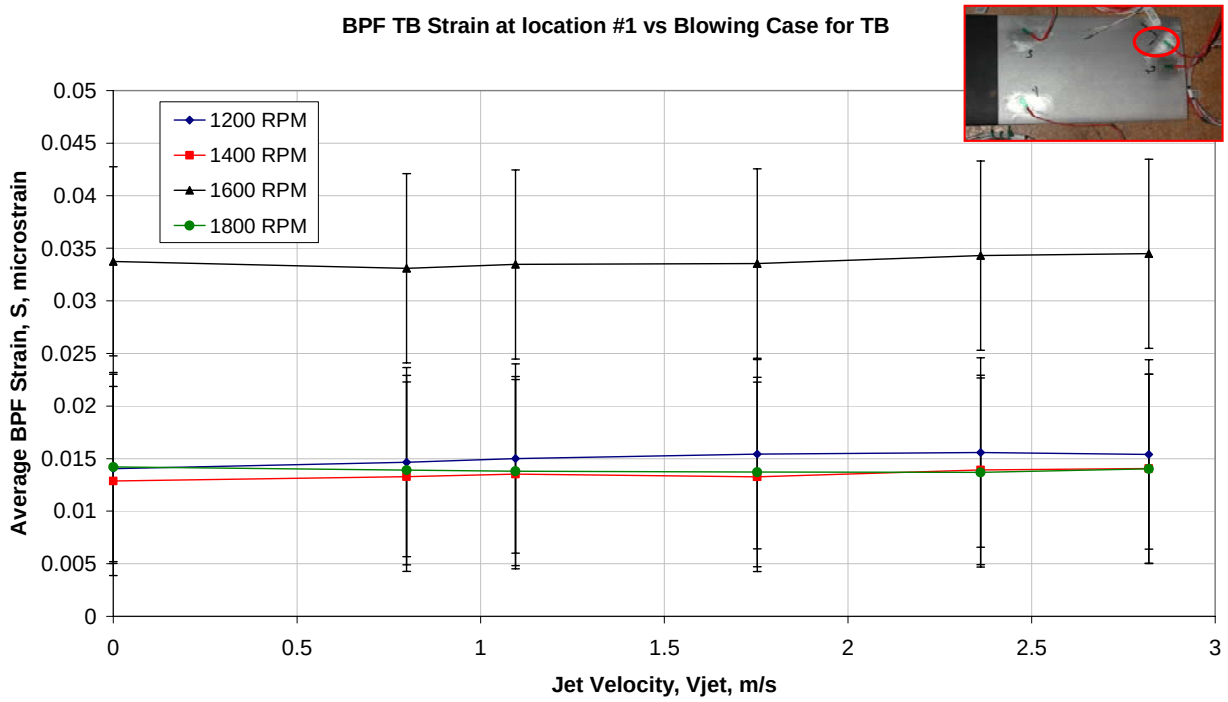

Figure 4.16: Magnitude of the strain at location #1 for the BPF.

4.4 Summary and Conclusions of EGV Flow Control Results

The two flow control configurations designed for implementation on the EGV were tested to show their effectiveness on reducing the unsteady rotor wake force on the EGV. Before the evaluation of the flow control configurations could be performed, the instrumentation had to be tested and the measurement limitations determined. These limitations were caused by the instrumentation sensitivity and the structural dynamics of the system. By applying the results of the modal data outlined in Section 3.3.2 to the assembly, it was discovered that a structural resonance existed within the frequency band that spanned all of the BPFs to be tested. This resonance causes the system to become extremely sensitive to small changes in the structural dynamics of the assembly. However, tests over several motor speeds indicated that the system was able to measure the BPF within 1.75 dB and had a signal to noise ratio of at least 20 dB. Thus, the system was able to measure the target BPF tonal change of 6 dB.

The leading edge blowing configuration (LEB) consisted of a single jet emanating from the leading edge of the hydrofoil opposite to the impinging flow. Since the intention of this type of flow control is to reduce the creation of tonal noise, the BPF response of the system to the application of flow control was used as the determining factor for success. Analysis of the measured magnitude of forcing at the BPF tone did not show a measurable change with the application of flow control. These results were supported by the accelerometer and strain gauge measurements at the BPF. Upon further investigation, while the magnitude results showed no change, study of the force gauge frequency response spectrums did indicate a change in response at the BPF for certain motor speeds and flow control jet velocities. At 1800 rpm, the application of LEB flow control spread the energies at the BPF across a larger band of frequencies than the case without flow control. Despite this, the overall amplitude of the response at the BPF remained the same. The computed frequency response of the force gauge measurements at other motor speeds did not exhibit the same variation due to flow control, implying that a particular combination of jet momentum with the incident flow momentum was required in order for the LEB to have this effect. However, the magnitude of the forcing at the BPF tone was not reduced by the target amount for any of the motor speeds. Thus, the leading edge blowing configuration was not effective in reducing the forcing on the EGV at the BPF.

The tangential blowing configuration (TB) incorporated two symmetric jets that ejected fluid tangentially to the blade surface towards the trailing edge for the purpose of creating an insulating layer of fluid around the blade surface. Like the LEB configuration, the primary quantity of interest in this set of experiments is the magnitude of the forcing at the BPF with respect to the application of flow control. At the BPF the system did not exhibit any measurable change in forcing on the EGV due to the addition of the flow control. The strain gauge and accelerometer data was also analyzed for the change in BPF forcing magnitude with respect to the amount of flow control fluid applied. Neither measurement indicated any appreciable change in the magnitude of the forcing at the BPF. The autospectrums of the strain gauge results displayed a slight shift in frequency for the flow control cases. However, it was determined that this shift corresponded to a minor variation in motor speed, not the application of flow control. Since none of the available measurements indicated any reduction in the forcing imparted on the EGV by the rotor wake, it can be concluded that the tangential blowing configuration was not effectual in reducing the forcing on the EGV by the required 6 dB.

5 Self-Pumping Rotor Results

The purpose of the self-pumping rotor experiments was to determine the effectiveness of the first generation self-pumping rotor design outlined in Section 3.4.3. The self-pumping rotor (SPR) was designed to pump fluid from an intake located at the hub to a slot in the trailing edge of the rotor blade tip. The slot extended from the tip along 25.4 mm of the rotor blade span. This chapter outlines the results of the SPR experiments for three different blowing slot thicknesses. These experiments tested the response of the SPR to variation in motor speed and trailing edge slot thickness; the test matrix used for these experiments is shown in Table 5.1. The maximum motor speed tested for each slot thickness was based upon the amount of cavitation evident and the magnitude of the rotor wake effects on the water surface. The limiting motor speed was lower for the SPR experiments than the tests performed on the seven-bladed rotor because the SPR began to cavitate at a lower speed. In addition, the increased span of the SPR blades causes more significant effects on the surface than the seven-bladed rotor due to the decrease in fluid above the rotor. This chapter will present the results from the aforementioned SPR experiments as well as the conclusions drawn from these results.

Table 5.1: Test matrix that was used for the self-pumping rotor (SPR) experiments

		Average Blowing Slot thickness (mm)		
	No Blowing	**Case1: 1.27**	**Case 2: 1.91**	**Case 3: 2.54**
Motor speed (rpm)	800	800	800	800
	1000	1000	1000	1000
	1100	1100	1100	1100
	1200	1200	1200	1200
	1300	1300	1300	1300
	1400	1400	1400	
	1500	1500	1500	

5.1 Case 1 Flow Control Results

The self-pumping rotor, as illustrated in Figure 3.15, incorporates the principles of trailing edge blowing for the purpose of wake-filling without requiring an external supply of fluid for the flow control. In order to test this concept the three-bladed SPR was manufactured differently than the seven-bladed rotor. Due to the problems encountered during the LEB and TB tests caused by the small force magnitudes, the SPR blades were left rough and unfinished. The

purpose was to create a large wake that would create forces on the downstream blade of enough magnitude that they could be confidently measured by the force gauge. Alternatively, the seven-bladed propeller was sanded smooth and painted to reduce the torque demand on the motor. However, the demand on the motor proved to be of less concern than originally thought. Thus, with the motor performance information yielded by the tests using the seven-bladed rotor it was determined that the SPR could be left unfinished without causing undue motor wear. Larger rotor wakes likely to be created by the rough blade surface would facilitate determining the effectiveness of the SPR design. Filling in a large rotor wakes causes a more dramatic difference between the blowing and non-blowing cases, thus ensuring that any changes due to the SPR could be measured by the available instrumentation.

In theory, the addition of the internal pumping system to the propeller should increase the amount of power required to turn it. The centrifugal force created by the rotation of the propeller propels the ingested fluid from the trailing edge slot. This additional work done on the fluid by the propeller should cause an increase in torque demand on the motor. Unfortunately, there is no direct measurement of the flow control fluid mass flow to confirm that any power increase was caused by the addition of flow control. Thus, the only means of determining if the propeller was functioning as designed was to monitor the changes of the motor torque and EGV response between the baseline condition and the flow control condition.

When the experiments were performed on the smallest slot thickness, 1.27 mm, the torque measurements indicated no changes due to the application of the flow control configuration. The torque versus speed curves for both the baseline and the flow control cases are plotted in Figure 5.1. As can be observed from the plot, the torque demand does not change with the addition of flow control. Aside from the single outlier point, all of the data taken across the two days of experiments yielded the same torque-speed curve. Only the torque measurements up to 1500 rpm are shown because this propeller, due to its rough finish and longer blades, began to cavitate at a lower rpm that the seven-bladed rotor. For the SPR, cavitation began at approximately 1600 rpm, thus limiting the test range to speeds 1500 rpm and below. The lack of change with the addition of the flow control indicates the strong possibility that the SPR is not succeeding in expelling any fluid from the slot.

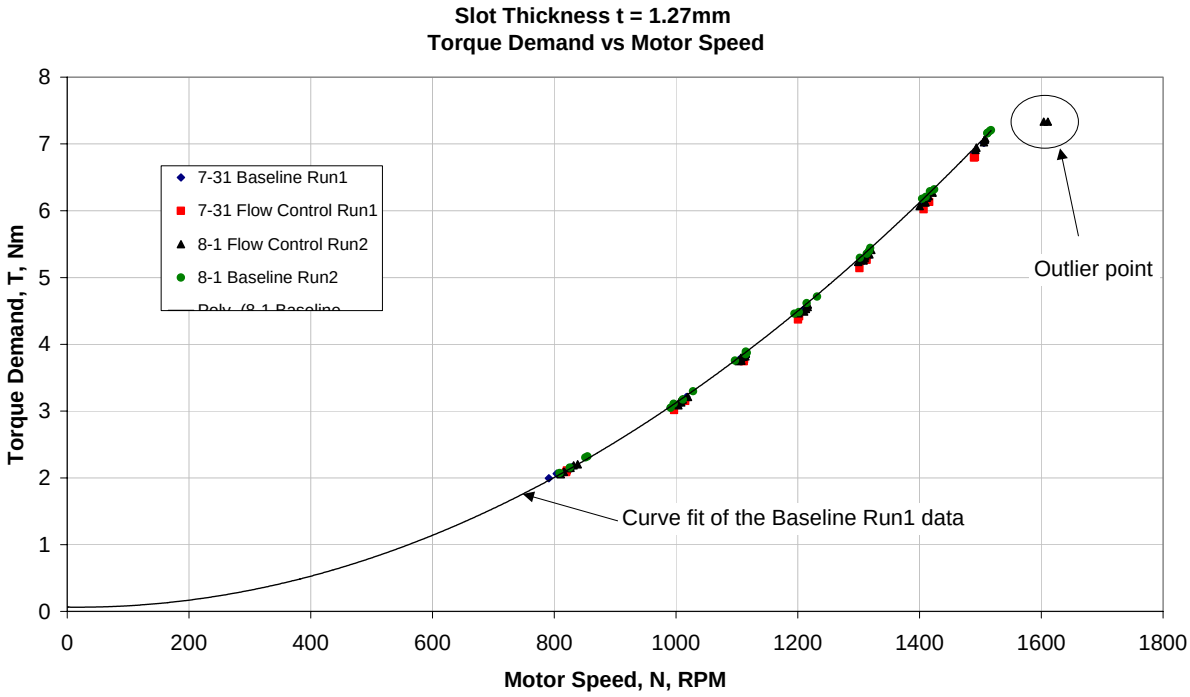

Figure 5.1: Torque demand versus motor speed for the t = 1.27mm flow control case and the baseline. 7-31 and 8-1 indicate the days on which the data was collected.

In order to determine if the flow control was pumping fluid from the trailing edge, the EGV measurements were examined for changes. All of the EGV measurements were processed in the same way as in the LEB and TB experiments. However, the BPF forcing in this case was significantly larger due to the rough blades and the increased blade span of the SPR. The autospectrum of the force gauge response for both the baseline and the flow control case is shown in Figure 5.2. From this plot it is clear that the addition of flow control causes no significant changes to the tonal force response. Due to the low blade count the range of BPFs tested was across a lower frequency band, 40 Hz to 75 Hz. This lower BPF meant that the first three harmonics of the BPF could be detected. These BPF tones appeared in the same locations on the frequency response spectrum with the same magnitudes even though flow control was applied.

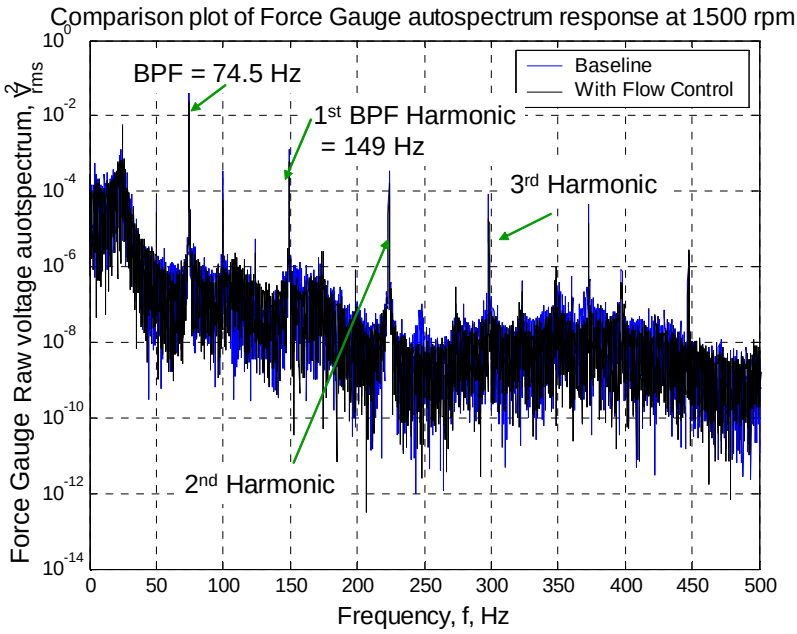

Figure 5.2: Force gauge autospectrum response for the baseline and flow controlled rotor with a slot thickness of 1.27mm.

In a similar method as the LEB cases, the BPF forcing magnitude was used as a measure of the effectiveness of the flow control. The signal to noise ratio at the BPF was found to be at least 20 dB, yielding the well defined BPF peaks seen in Figure 5.2 and allowing the forcing magnitude at the BPF to be calculated from the spectral magnitudes. The magnitudes at the BPF for each case were calculated from these BPF tone peaks and are plotted against motor speed in Figure 5.3. The exemplar error bars in Figure 5.3 show the uncertainty computed using a 95% confidence interval on the baseline data. The data was taken over three days in order to account for the variability that was introduced by moving the motor assembly between each test. As was discussed in Section 4.1, removing the motor causes a large amount of variability in the data due to the limitations on repositioning the motor assembly. However, removing the motor was unavoidable due to the changes that were applied to the propeller between each set of tests. It can be seen that the data taken on August 1 showed a significant difference from the data taken on other days. This is likely due to both motor mounting position and the degree of lubrication in the EGV bearing. The motor mounting position would affect the behavior of the rotor flow field with respect to the EGV by altering the way in which the rotor wake impacts the EGV, while the lubrication of the bearing in the EGV assembly changes the structural dynamics of the

force transducer system. Yet, despite the changes that occurred between test days, the flow control showed no variation when compared to the baseline measurement of that test day.

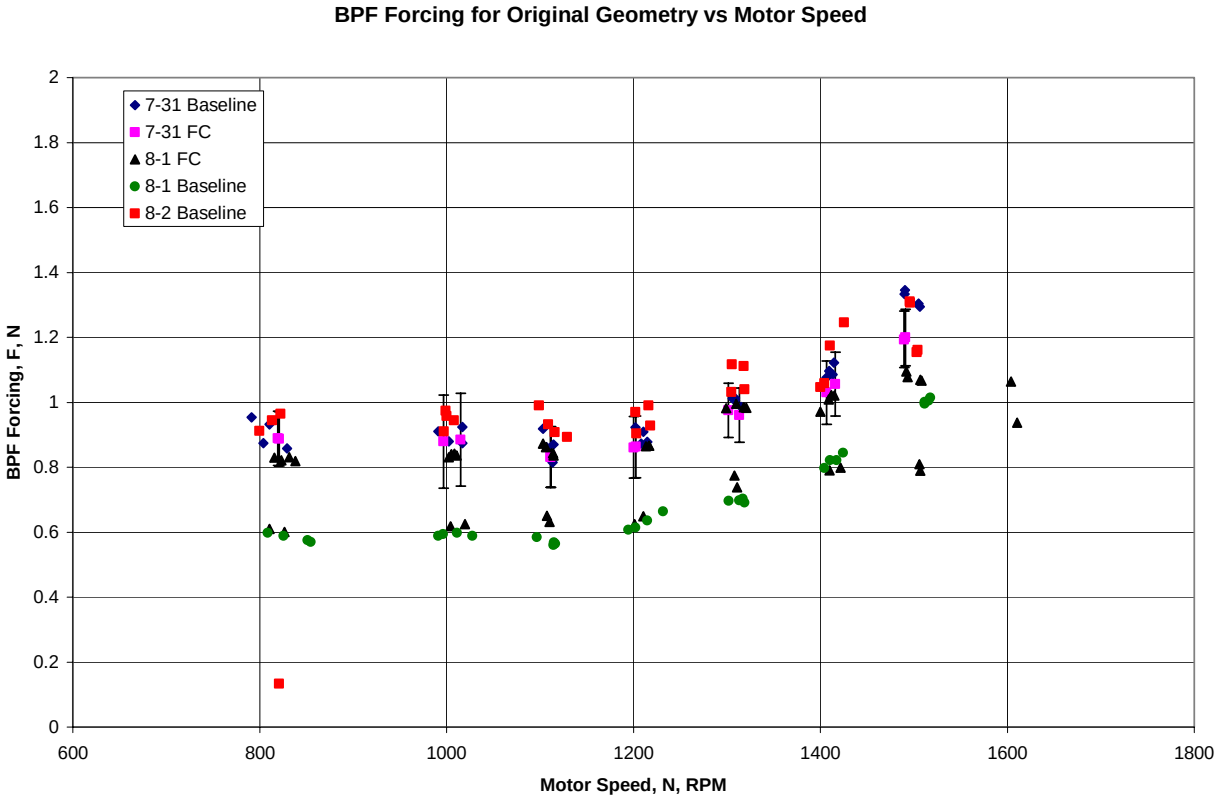

Figure 5.3: Forcing at the BPF for the 1.27 mm slot thickness case for both with and without flow control with respect to motor speed.

Throughout all tests performed using this assembly, the accelerometer and the strain gauges showed a larger sensitivity to changes in motor position. In this case, the magnitude of the accelerometer response was smaller than the sensitivity of the transducer and the data acquisition system. It is unlikely that the acceleration that was measured was able to indicate any sort of trend in the EGV response. Conversely, the strain measurements were significantly larger than those taken for the LEB case, though not due to obvious resonance effects. Since the accelerometer measurement was too small to be confidently measured, the measured strain alone was used to confirm the results of the force gauge measurements. The BPF component of the strain at location 3 for both the flow control cases and the baselines cases are shown in Figure 5.4 with respect to the measured motor speed. While the frequency response function does not contain any significant resonances in this tested frequency, the 1200 rpm test case does yield a BPF of 60 Hz. Due to the bandwidth that is used to calculate the forcing at the BPF, the 60 Hz

electrical noise magnitude becomes added the measured BPF magnitude for some cases where the BPF is within 0.5 Hz of 60 Hz. In order to limit the effect of the electrical noise, the BPF magnitude of the strain was computed using a 1 Hz bandwidth, as opposed to the 4 Hz band that was used for the other measurements. However, the reduction in computation band only accounts for the electrical noise in those measurements that were taken at speeds that were at least 15 rpm less or greater than 1200 rpm. This electrical noise explains the significantly higher values of strain that occur at motor speeds with BPFs very close to 1200 rpm. Despite this, for the flow control slot thickness of 1.27 mm the SPR does not show any indication of consistent changes due to the addition of flow control, thus it is unlikely that the SPR was expelling fluid from the slot.

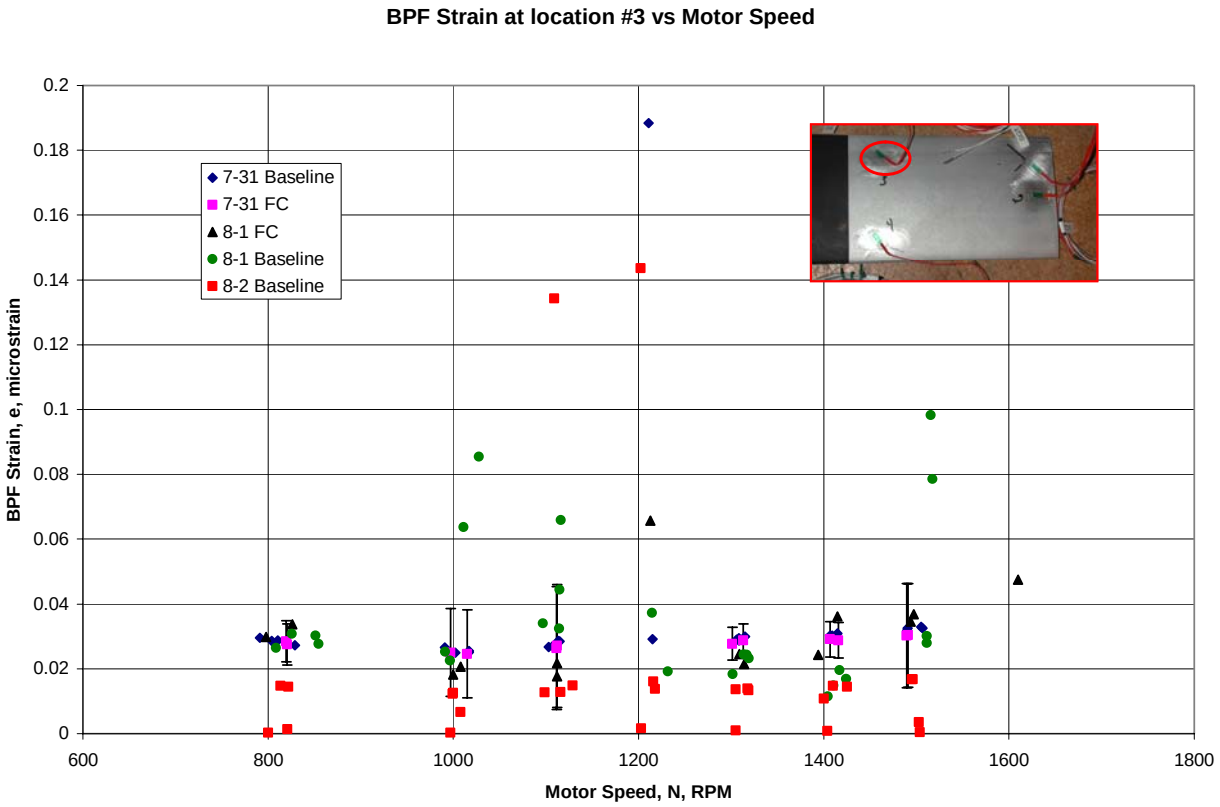

Figure 5.4: BPF strain at location #3 for the baseline and flow control slot thickness of 1.27 mm.

5.2 Case 2 and 3 Flow Control Results

The SPR was not originally designed to have a flow control slot with variable thickness. However, given the results produced by the Case 1 configuration, it was decided that alterations

were required in order yield a functioning SPR prototype. The size of the inlet was fixed by the physical constraints of the rotor. However, one of the possible causes for the rotor to be unable to pump fluid was a large amount of pressure losses due to friction from both the internal passageways and the jet exit. The wall friction within the passageways could not be altered or smoothed after the manufacture of the propeller without causing serious damage. Therefore, the pressure losses caused by the jet were chosen to be the issue that was addressed. To this end, the slot thickness was enlarged to reduce the jet exit losses. Due to the geometry of the blade trailing edge, this change involved a significant alteration of the rotor trailing edge, making the trailing edge very blunt. Figure 5.5 shows pictures of the Case 2 and Case 3 altered rotors. The blunt trailing edges cause a larger amount of drag on the propeller, thus increasing the torque demand. The torque demand with respect to motor speed for both the Case 2 and 3 rotors is given in Figure 5.6, which indicates that increasing of the slot thickness does increase the torque demand as expected. Yet, the torque demand still does not change significantly between the baseline and the flow control cases; as discussed in Section 5.1 this result implies that the SPR was not functioning as designed because the torque should increase with the transfer of power to pumping the internal fluid.

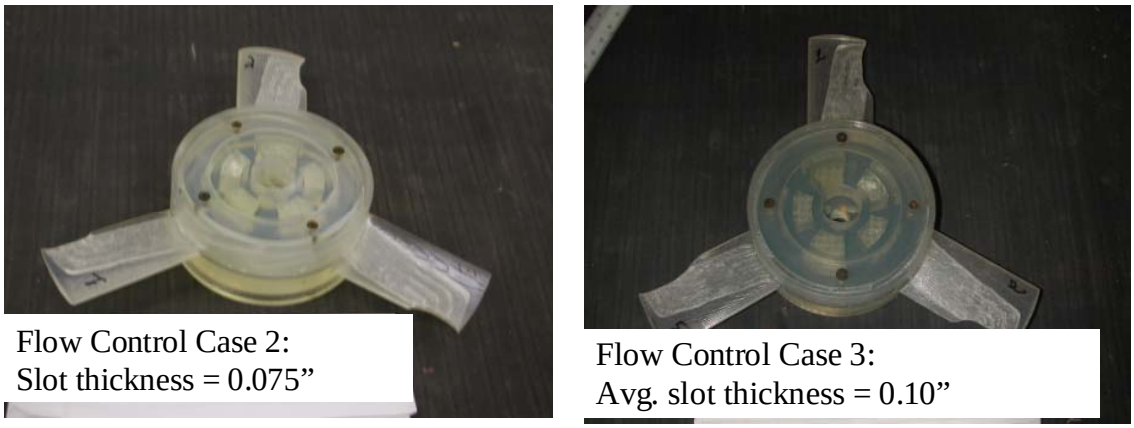

Figure 5.5: Pictures of the Case 2 and Case 3 rotor alterations.

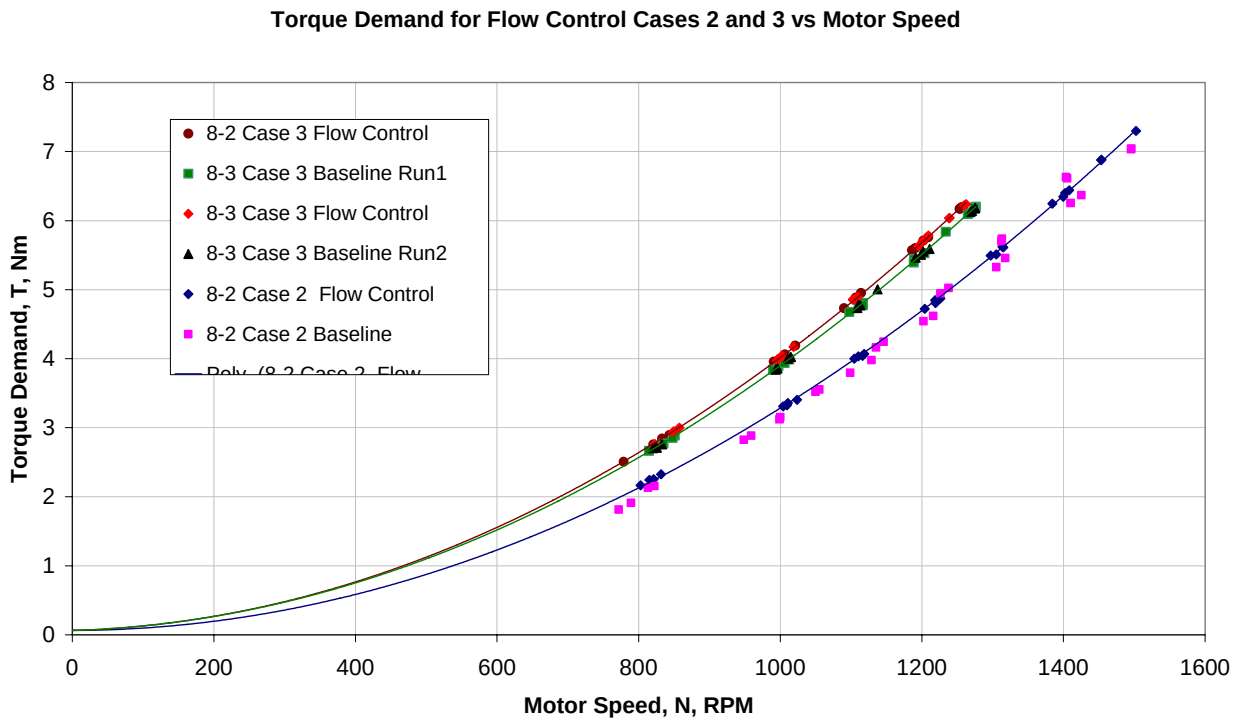

Figure 5.6: Average torque demand versus motor speed for the Case 2 and 3 altered rotor.

Unfortunately, these alterations also caused free surface vortices to occur on the water surface. The strength of these vortices caused the set of motor speeds to be limited to 1300 rpm and below for the Case 3 experiments. The surface vortices were of such strength that the instrumentation and non-waterproof sections of the EGV assembly, such as the force gauge and the linear bearings, were in danger of becoming damaged by water. Due to the lack of information on the rotor flow field, the cause of the surface effects is not precisely known. The blunt trailing edge could have caused a large tip vortex that then interacted with the water surface. Due to space constraints there was only 0.165 m of water above the rotor blade tip. This means that the rotor wake could have diffused enough to interact with the water surface.

Despite the free surface effects caused by the alterations to the rotor, the fluctuating force exerted on the EGV did not change dramatically in magnitude due to the application of the flow control configuration. The forcing at the BPF for Cases 2 and 3 with respect to motor speed is given in Figure 5.7. The estimated error for the force measurements is given by a 95% confidence interval as outlined in Appendix F.2. As can be seen, the application of the flow control configuration, both Case 2 and Case 3, fails to make any measurable changes in the BPF

tonal forcing on the EGV. The spread of the data points covers a large range due to the error caused by removing the motor assembly in between tests. However, the small changes in the force measurements do not correlate with the application of flow control and are within the measurement error of the data. Given this consistency of the unsteady forcing data even with the addition of flow control, there is no data to suggest that the SPR was able to pump fluid from the blade trailing edge.

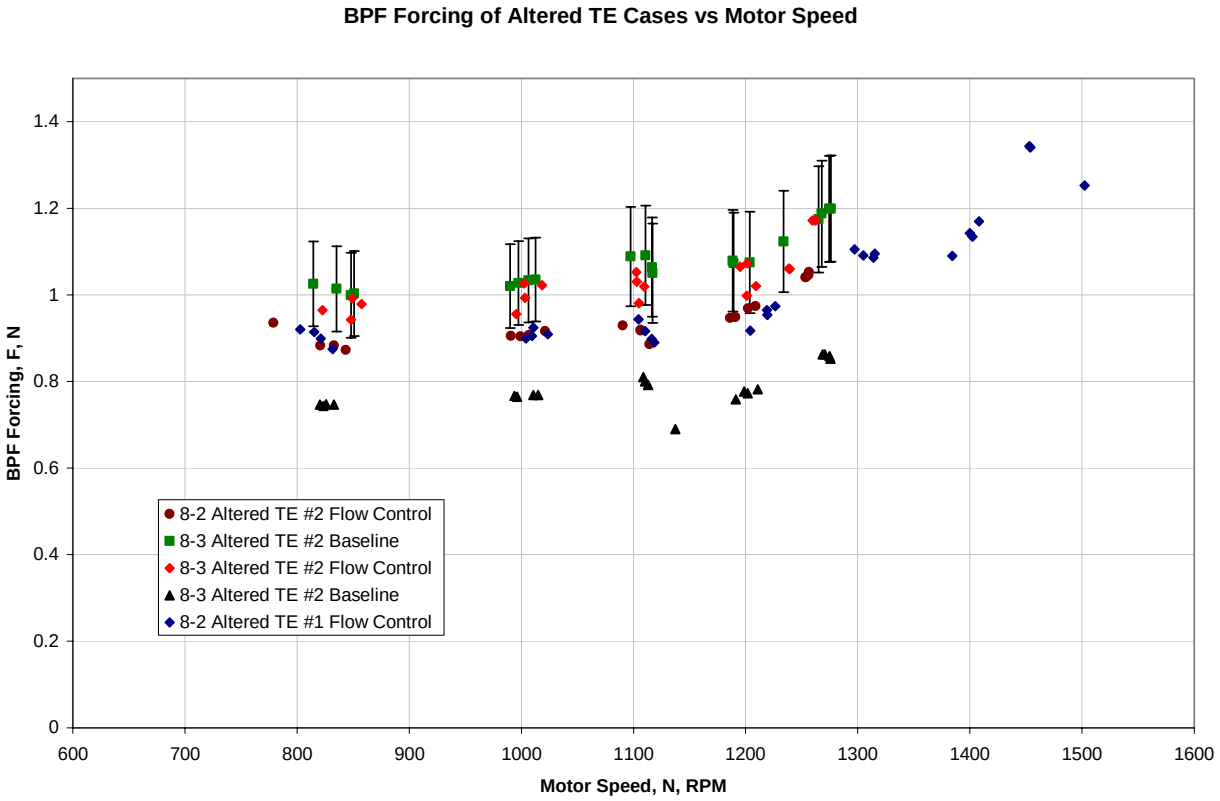

Figure 5.7: BPF forcing magnitude versus motor speed for flow control cases 2 and 3

As in the Case 1 results, given in Section 5.1, the accelerometer yielded BPF magnitudes that were not within its measurement range. Thus, it remains that the strain gauge measurements confirm the effects, or lack thereof, of the flow control configuration. The BPF strain measured at location 3 is shown in Figure 5.8 with respect to the motor speed. The error, as calculated in Appendix F.2, is the measurement limitation of the strain gauges. As seen previously, the 1200 rpm data is magnified by the 60 Hz electrical noise that occurs close to the BPF. Due to the band required to calculate the magnitude at the BPF form 1200 rpm, the electrical noise could not be separated from the strain caused by the wake forcing for all of the data points. This data also

shows that the flow control configuration results do not differ from the baseline results. Thus, given that no effect was observed through the available instrumentation and there is no direct measurement of the flow emitted from the flow control configuration, the conclusion is that this first generation design was unable to pump a significant amount of water from the trailing edge flow control slot to fill in the rotor wake. In order for the experiments to prove the SPR effective, a significant tonal reduction should have been observed. Since the trailing edge blowing from a rotor has been heavily researched by previous experiments and proven to reduce the radiated acoustic noise, it can be concluded that this SPR design was not able to produce any fluid to fill in the rotor blade wakes.

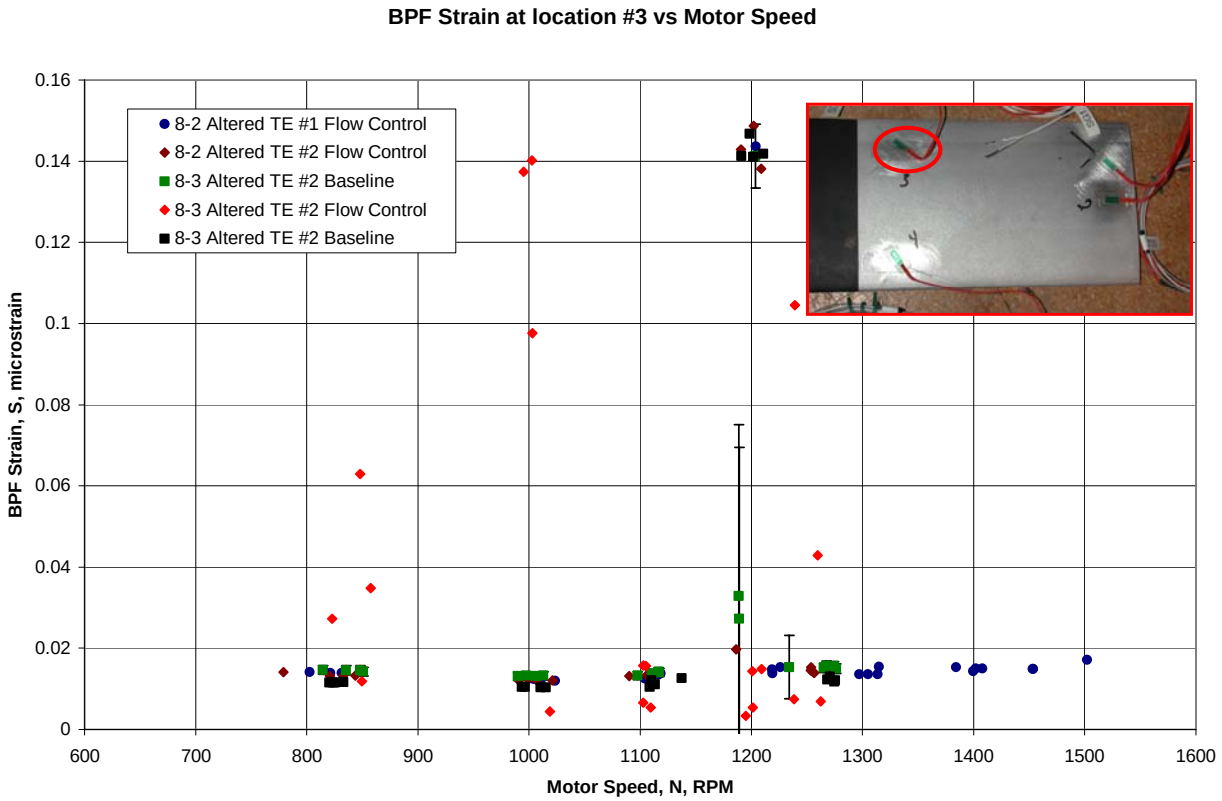

Figure 5.8: BPF component of the strain measured at location #3 with respect to the motor speed.

5.3 Summary of Self-Pumping Rotor Tests

In the effort to discover a mechanically simple method to implement trailing edge active flow control from a rotor, a prototype self-pumping rotor (SPR) was designed. The SPR ingested low velocity flow from the hub and pumped flow internally to the trailing edge of the

rotor blade. This flow was expelled from an inch long trailing edge blowing flow control slot that was placed at the tip of the rotor blade. A set of experiments were conducted that tested the EGV response to the SPR at varying motor speeds. In addition, torque demand measurements were acquired to gauge the performance penalties of the SPR.

Experimental data taken on the initial design showed none of the expected increases in torque demand due to the additional work being done on the fluid by the internal pumping of the SPR. The torque required by the rotor remained the same both with and without the flow control. Also, the force gauge response to the rotor showed no significant change between the baseline case and the flow control case. Unfortunately, the SPR was not equipped with any direct measurements of the flow velocity exiting the flow control slot. Thus, it cannot be confirmed that the Case 1 SPR was able to pump water. Given the lack of response by all of the measurements it was concluded that the Case 1 SPR was not able to supply fluid to the flow control.

In an attempt to reduce the pressure losses within the flow control plumbing, the thickness of the exit slot was enlarged 1.5 and 2 times the original Case 1 thickness. The two iterations of enlarging the exit area, Case 2 and Case 3, were examined using the same method as Case 1. As opposed to Case 1, both Case 2 and Case 3 caused an increase in the free surface effects caused by the rotor likely due to the blunter trailing edge created by the enlargement of the flow control slot. However, neither case showed any deviation in torque or EGV forcing from their respective baseline configurations. Therefore, the Case 2 and Case 3 alterations did not give any indication that the SPR was able to eject water from the flow control slots. Incorporating all of the results from each measurement and the different slot thicknesses, the conclusion is that the first generation design of the SPR was unable to pump water from the hub to the trailing edge slot.

6 Conclusions

This research investigated the design and testing of new methods for reducing the noise generated by rotor-stator interactions. The application of active flow control to both the rotor and the EGV was used to reduce the magnitude of the interactions, thus reducing the radiated noise. The active flow control on the rotor was implemented via a self-pumping design which used fluid taken from the hub of the rotor and pumped through the rotor blade to a trailing edge slot at the tip, thus providing fluid to fill in the rotor wake. The EGV was equipped with two separate active flow control concepts, leading edge blowing and tangential blowing. Both were designed to reduce forcing on the EGV by increasing the offset distance of any passing vortices. The leading edge blowing used a single jet located at the leading edge of the blade while the tangential blowing utilized two tangential jets along the blade surface. This chapter reviews the results and conclusions of the experiments on these flow control techniques presented previously as well as suggested avenues for further research in this area.

6.1 Results and Conclusions

Previously, the predominate application of active flow control was for aeroacoustic noise reduction in turbomachines. This work tested the application of these concepts in a hydrodynamic turbomachine. The principle is that the reduction of the rotor-stator interaction noise is achieved by reducing the scope of the interaction. This radiated noise from this interaction is directly related to the fluctuating force applied to the lifting body by the rotor wake. This principle was applied to the design of a new apparatus for testing the feasibility of active flow control configurations. The apparatus consisted of two parts: a motor assembly and an exit guide vane (EGV) assembly. The motor assembly drove a custom designed propeller, creating a three-dimensional flow field upstream of the EGV assembly. The EGV assembly was instrumented with a force gauge to measure the fluctuating lift force exerted on the EGV by the passing rotor wakes. This measurement allowed extrapolation of the effects of the flow control on the acoustic radiation. All of the experiments were conducted at Virginia Tech's Fluids Laboratory in a 2 ft by 2 ft x 6 ft recirculating water tunnel.

Two types of flow control were tested in this apparatus: leading edge blowing from the EGV and trailing edge wake filling from the rotor. The leading edge blowing consisted of two

separate configurations that were installed on the EGV. The first, leading edge blowing or LEB, incorporated a single jet that located at the leading edge of the hydrofoil. The jet is directed upstream into the oncoming flow to break up or offset any convecting coherent structures before they impact the EGV. The other type of leading edge blowing, TB, involves the application of two symmetric jets that are positioned tangential to the EGV surface. The jets attach to the surface and flow downstream towards the trailing edge of the hydrofoil. Similar to the film cooling used in high-speed turbines, the jet insulates the blade from the surrounding flow structures. The second type of flow control that was examined was the use trailing edge blowing from the rotor blades for the purposed of wake filling. Unlike typical rotor wake filling designs, the rotor design that was evaluated required no external plumbing to supply the blowing fluid. The rotor was equipped with an intake at the hub that ingested low velocity flow from around the centerbody and pumped it out to the trailing edge. This self-pumping rotor was equipped with a flow control slot that extended over a third of the blade span at the tip.

The calibration of the EGV assembly yielded data modeling the influence of structural vibration on the measurement of the fluctuating force shed by the seven-bladed rotor. For the tests of the LEB and TB configurations a structural resonance was present within the frequency bandwidth of interest, thus introducing a large measurement error at the 1600 rpm motor speed. Despite this, the LEB experiments did yield some viable results. However, none of the results acquired showed any conclusive change in forcing on the EGV at the BPF for this assembly. All measurements indicated little to no change in the system at the BPF. Similar tests were conducted to evaluate the TB configuration. The measurements for the TB experiments experienced the same limitations as those in the LEB tests. The system response was different with the application of the TB configuration; however, no improvement in the fluctuating forcing at the BPF was yielded.

A first-generation prototype of a three-bladed self-pumping rotor was installed in the test assembly to determine the functionality of the rotor design. No direct measurements were available to assess the amount of flow that was pumped through the rotor; the assessment of the rotor's functioning capacity was provided by the secondary measurements of the fluctuating force on the EGV and the torque demand on the motor. With the addition of the flow control the torque demand should increase due to the increase in work performed on the fluid. Also, from the previous research performed in air, the wake filling applied to the rotor should reduce the

amount of fluctuating force measured by the EGV. Tests were performed on the self-pumping rotor with three blowing slot heights. None of the blowing slot configurations yielded any change from the baseline conditions. The lack of change in any of the available measurements indicated that the rotor was able to pump any fluid to fill the rotor wake. Further investigation into the design of the interior passageways and velocity measurements of the rotor wake would assist in optimizing this design and achieving positive results.

6.2 Suggested Future Work

The research outlined in this document gives rise to several possible improvements and additions that could be made to further the experiments. The two main changes are the alterations to the experimental assembly and the continuation of the self-pumping rotor design. In conducting the tests on the flow control configurations several improvements in the assembly were highlighted by the difficulties that arose. An application of a different seven-blade rotor design could improve the clarity of the measured data. The rotor design used was designed for optimal performance at a given torque value. However, the wakes shed by the rotor did not cause enough force on the EGV to be measured reliably with the available instrumentation. Redesigning the rotor to produce more work on the fluid would have increased the force exerted on the EGV, thus improving the measurement quality. In addition, a more sensitive force gauge could have also have improved the system measurement feasibility.

The linear bearings used to isolate the fluctuating lift force did not allow for any high frequency analysis. The friction inherent in the bearing caused damping that limited the frequency response of the system. A different design of the EGV mount that did not require the use of linear ball bearings could have improved the system frequency response. Related to the frequency limitations was the presence of structural resonances in the bandwidth of interest. A redesign of the EGV assembly that increased the structural stiffness would reduce the amount of data corrupted due to resonance effects by increasing the frequency of the first structural mode outside of the frequency band of interest.

Although the first generation self-pumping rotor that was tested did not show any signs of functioning as intended, the concept is still valid. The application of CFD to model the intake and internal flow could provide guidance for a more robust rotor design. In addition, the manufacturing limitations of stereolithography (SLA) indicate that the rotor should be

manufactured out of a difference material. The first-generation rotor that was tested had rough structures inside of the internal passageways. This causes frictional pressure losses that further reduce the operability of the rotor. Also, detailed velocity measurements of the rotor wake would also guide the design of the trailing edge slot to match the rotor design. Such velocity measurements could also indicate the amount of blowing that would be required to fill in the wake velocity deficit. In addition, measurements of the flow upstream of the rotor would better guide the design of the intake such that advantage could be taken of the existing flow effects in order to maximize the efficiency of the pumping mechanism. Yet, despite the setbacks found in this research, the self-pumping rotor design still merits further investigation.

Appendix A Derivation of Acoustic Pressure-Force Relationship

The force exerted on the EGV is related to be acoustic radiation by the wave equation,

$$\frac{1}{c_0^{\,2}}\frac{\partial^2}{\partial t^2}p-\nabla^2 p=-\nabla\cdot\bar{f}_v, \qquad \textbf{A.1}$$

where $\bar{f}_v$ is the force exerted by the EGV on the fluid per unit volume. Using a free-field assumption to simplify the situation means that the effects of solid boundaries are ignored. This means that adding the Green's function, $G\langle\bar{x},t\mid\bar{y},t\rangle$ to Equation A.1 yields the inhomogeneous equation,

$$\left(\frac{1}{c_0^{\,2}}\frac{\partial^2}{\partial t^2}-\nabla^2\right)G\langle\bar{x},t\mid\bar{y},t\rangle=-\nabla\cdot\bar{f}_v(\tau)\delta(\bar{x}-\bar{y}). \qquad \textbf{A.2}$$

Previous researchers have determined the Green's function for common situations such as this to be

$$G\langle\bar{x},t\mid\bar{y},t\rangle=\frac{1}{4\pi|\bar{x}-\bar{y}|}\delta\left(t-\tau-|\bar{x}-\bar{y}|/c_0\right). \qquad \textbf{A.3}$$

The pressure field response solution to A.2 is related to the Green's function as

$$p(\bar{x},t)=-\int_{-\infty}^{\infty}\int_V\left\{\nabla_y\cdot\bar{f}_v(\bar{y},t)\right\}G\langle\bar{x},t\mid\bar{y},\tau\rangle d\bar{y},d\tau\,. \qquad \textbf{A.4}$$

Combining Equations A.3 and A.4 yields

$$p(\bar{x},t)=\nabla_x\int\frac{\bar{f}_v\left(\bar{y},t-|\bar{x}-\bar{y}|/c_0\right)}{4\pi|\bar{x}-\bar{y}|}d\bar{y} \qquad \textbf{A.5}$$

Applying a thin blade approximation to the EGV and utilizing Gauss' Divergence Theorem Equation A.5 becomes

$$p(\bar{x},t)=\nabla_x\cdot\int_{S_v}\frac{\bar{f}_s\left(\bar{y},t-|\bar{x}-\bar{y}|/c_0\right)}{4\pi|\bar{x}-\bar{y}|}dS_v(\bar{y}), \qquad \textbf{A.6}$$

where f_s is the force per unit area of the EGV surface, S_v. Estimating the sound source as concentrated at the center of mass, y_c allows Equation A.6 to be solved in terms of the net applied force. In this case according to orientation shown in Figure 4.1, the net force is

$$\bar{F}\left(\bar{y}_c, t-\left|\bar{x}-\bar{y}_C\right|/c_0\right)=0\hat{i}+F_L\left(\bar{y}_c, t-\left|\bar{x}-\bar{y}_C\right|/c_0\right)\hat{j}+0\hat{k} \qquad \textbf{A.7}$$

Combining Equations A.6, A.7, and the previously listed approximations yields[32]

$$p(\bar{x},t)\approx\frac{\partial}{\partial x_2}\left\{\frac{1}{4\pi\left|\bar{x}-\bar{y}_c\right|}F_L\left(\bar{y}_c, t-\left|\bar{x}-\bar{y}_C\right|/c_0\right)\right\}. \qquad \textbf{A.8}$$

Which can be written as

$$p(\bar{x},t)\approx\frac{1}{4\pi\left|\bar{x}-\bar{y}_c\right|}\nabla_x\cdot\bar{F}_L\left(\bar{y}_c, t-\left|\bar{x}-\bar{y}\right|/c_0\right). \qquad \textbf{A.9}$$

Appendix B Modal Data Results

The modal analysis performed on the EGV assembly involved measuring the response of all of the instrumentation due to a point impulse force on the blade. The blade was divided into a grid of 65 points. This section gives examples of the measured coherence and frequency response functions for the force gauge and the accelerometer mounted on the blade. All of the plots are indexed by their location on the blade, see Figure 3.10 for the coordinate system used in these tests.

B.1 Typical Force Gauge and Accelerometer Coherence Data

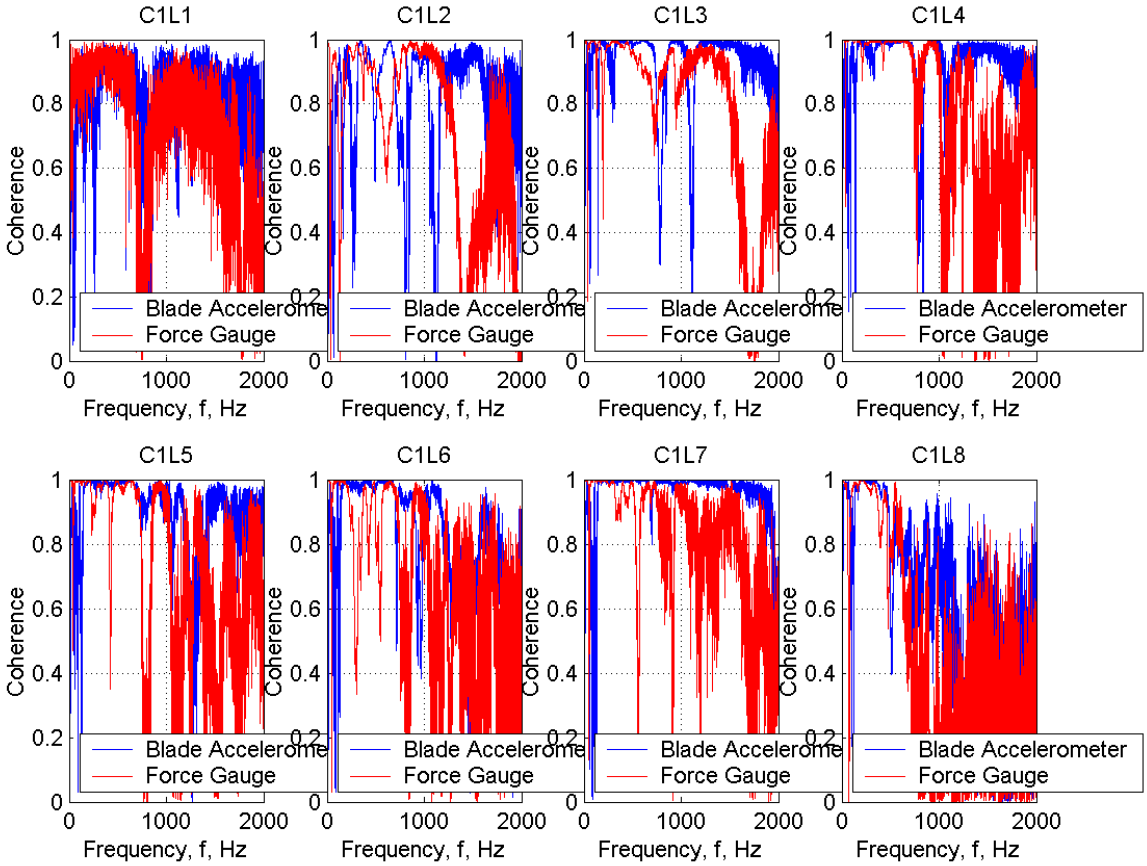

Figure B.1: Coherence between repeated hammer tests at points C1L1 through C1L8 for the accelerometer and the force gauge.

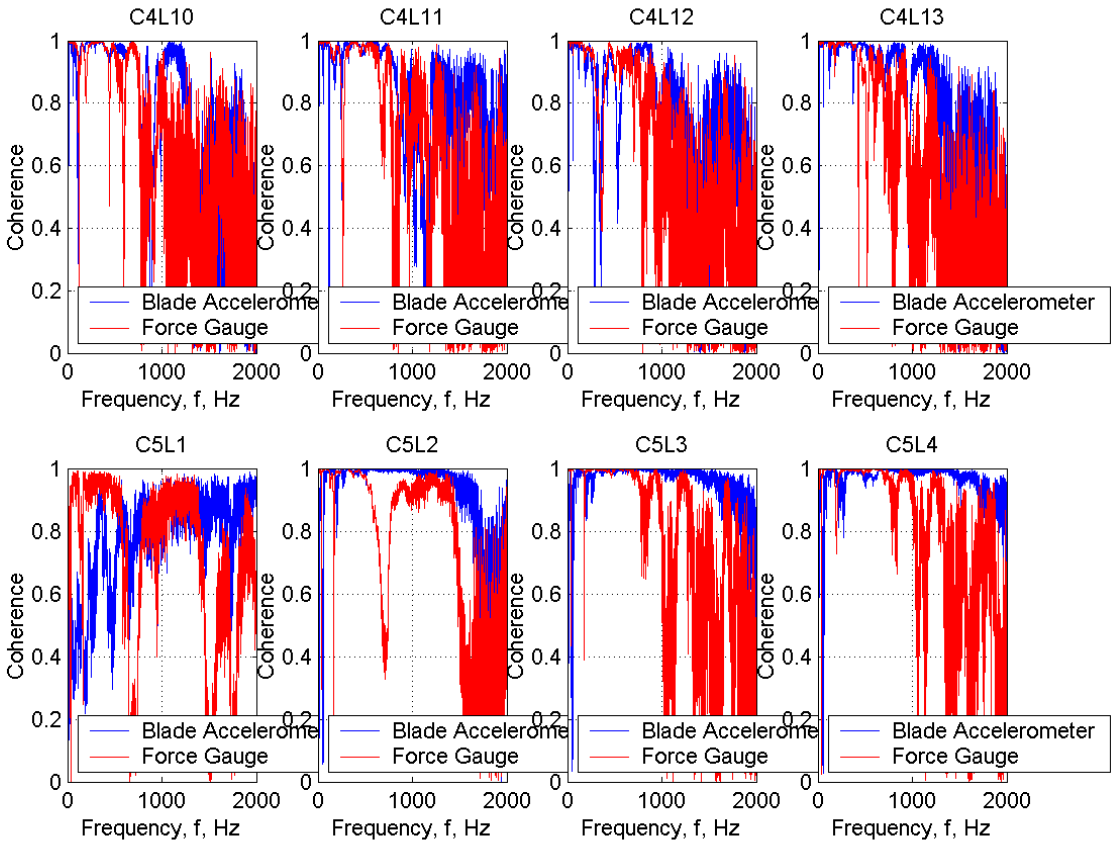

Figure B.2: Coherence between repeated hammer tests at points C4L10 through C5L4 for the accelerometer and the force gauge.

B.2 Typical Force Gauge Frequency Response Functions

The frequency response functions for the force gauge were computed using the H_1 response function estimator given in Equation 4.1.

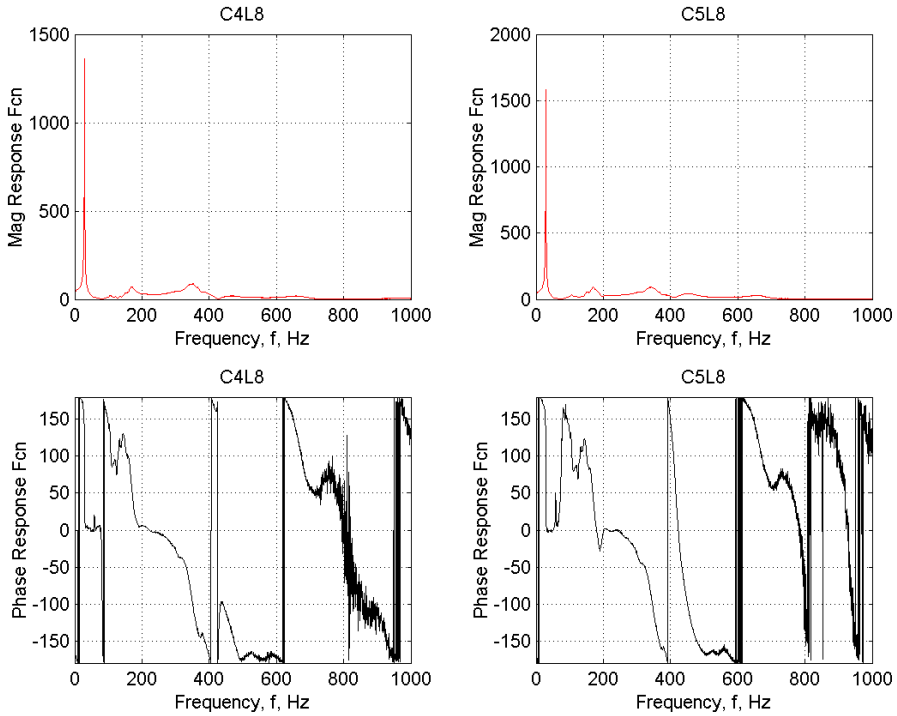

Figure B.3: Frequency Response Functions for the points C4L8 and C5L8

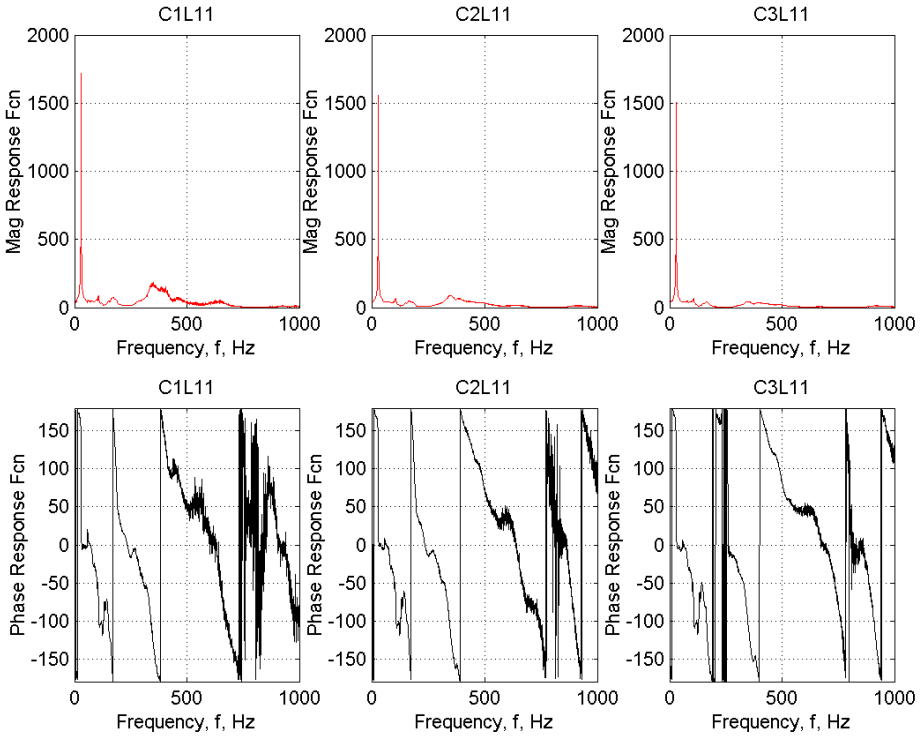

Figure B.4: Magnitude and phase of the frequency response functions for the points C1L11, C1L11, and C1L12

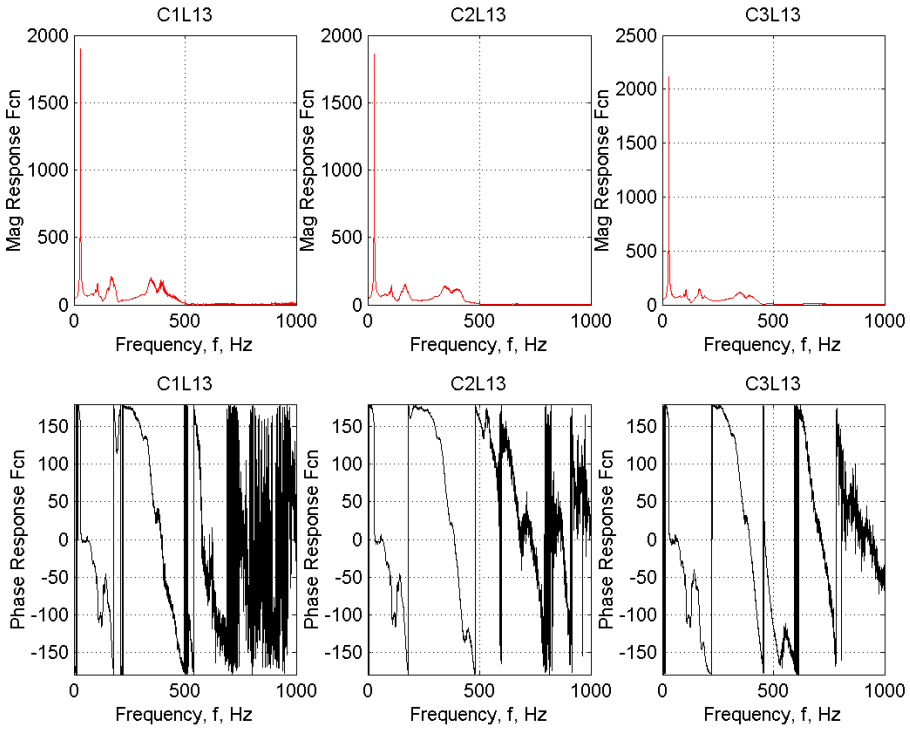

Figure B.5: Magnitude and phase of the frequency response functions for the points C1L13, C1L13, and C1L13

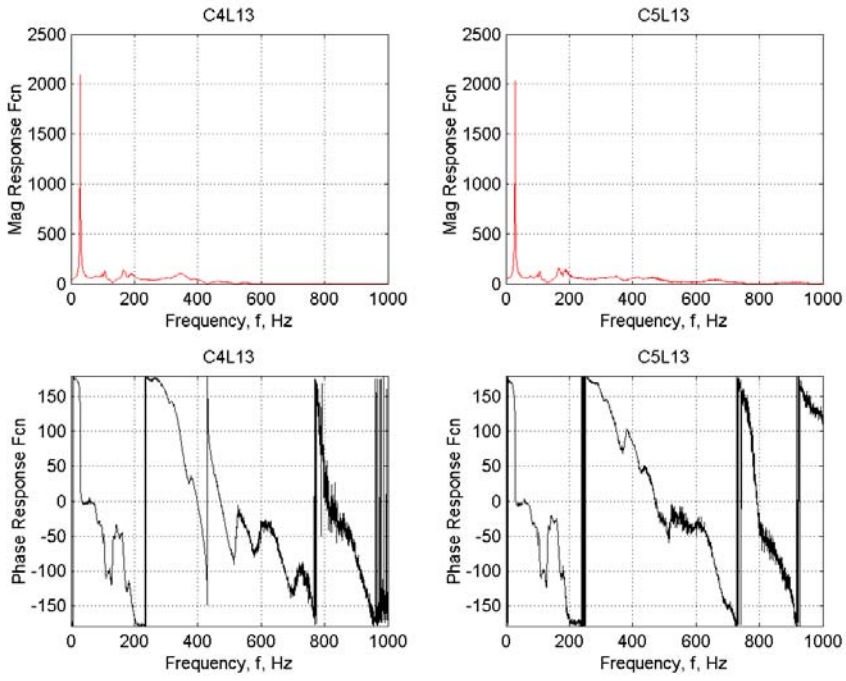

Figure B.6: Magnitude and phase of the frequency response functions for the points C4L13 and C5L13

B.3 Typical Accelerometer Frequency Response Function

In the same manner as the force gauge frequency response functions, the accelerometer mounted on the blade for the structural response tests was measured in order to compute the frequency response function. This section gives the several example frequency response functions.

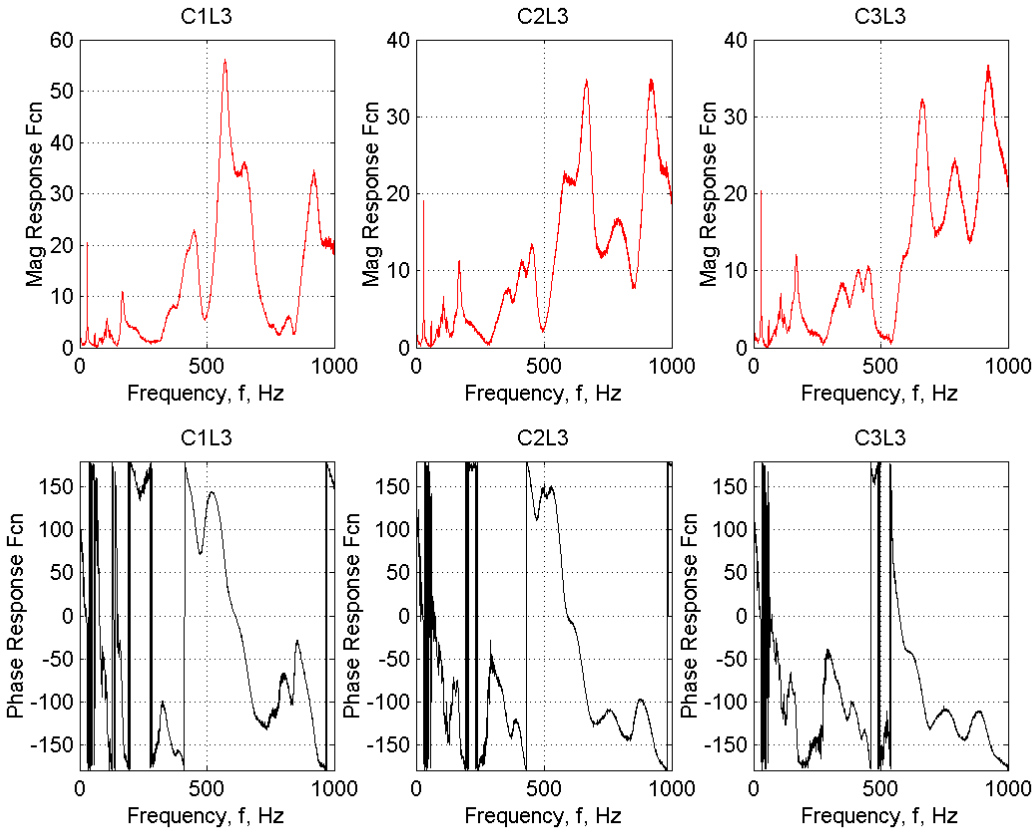

Figure B.7: Accelerometer frequency response functions for points C1L3, C2L3, and C3L3.

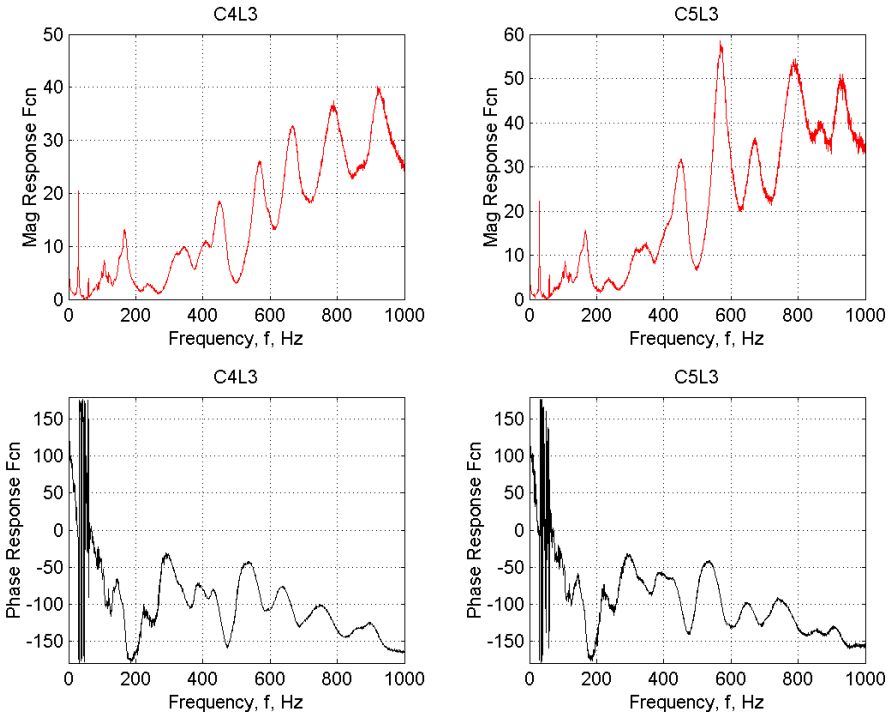

Figure B.8: Accelerometer frequency response functions for points C4L3 and C5L3.

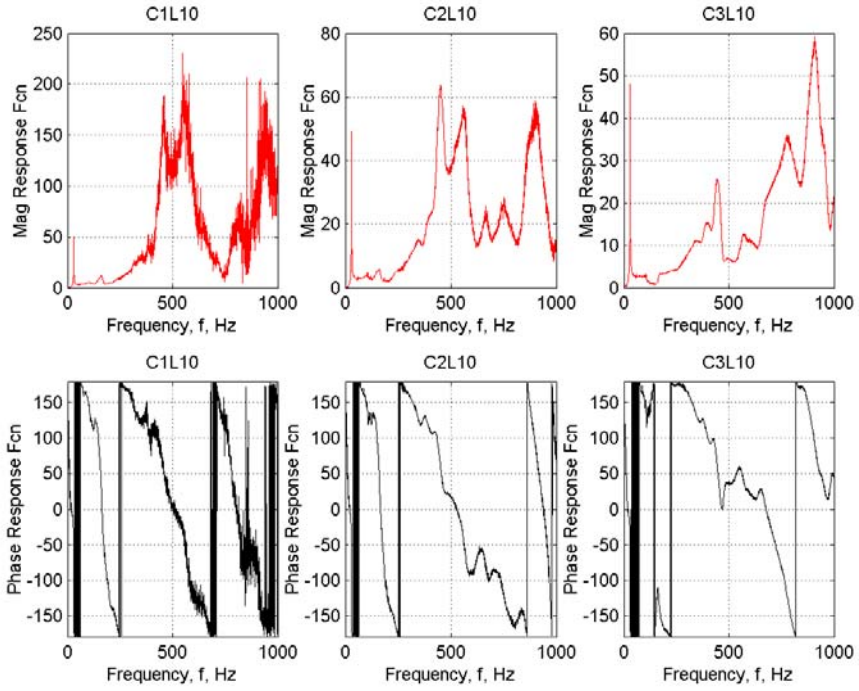

Figure B.9: Accelerometer frequency response functions for points C1L10, C2L10, and C3L10.

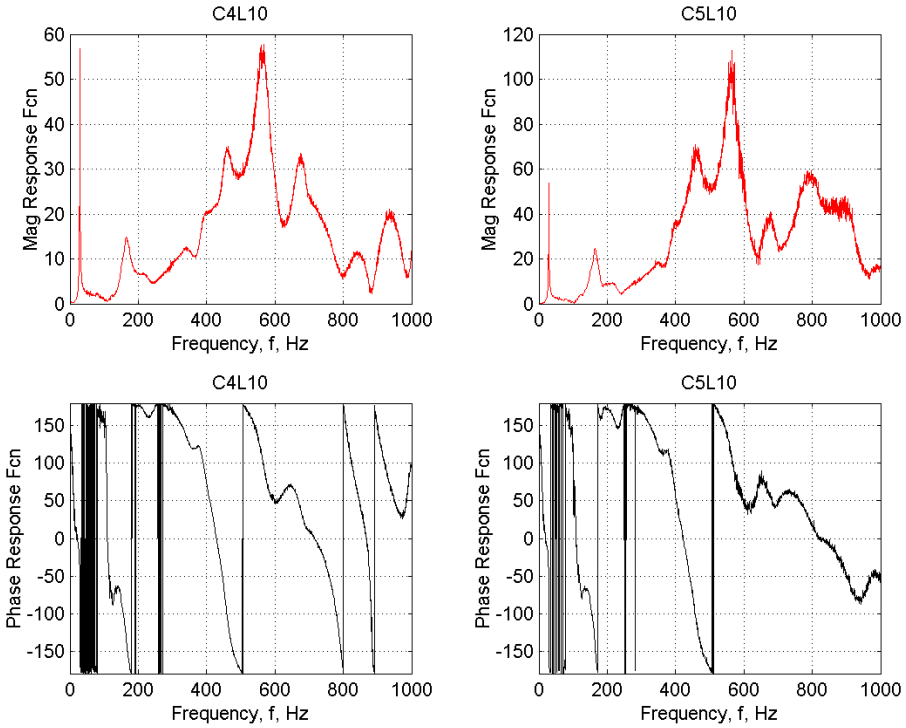

Figure B.10: Accelerometer frequency response functions for points C4L10 and C5L10.

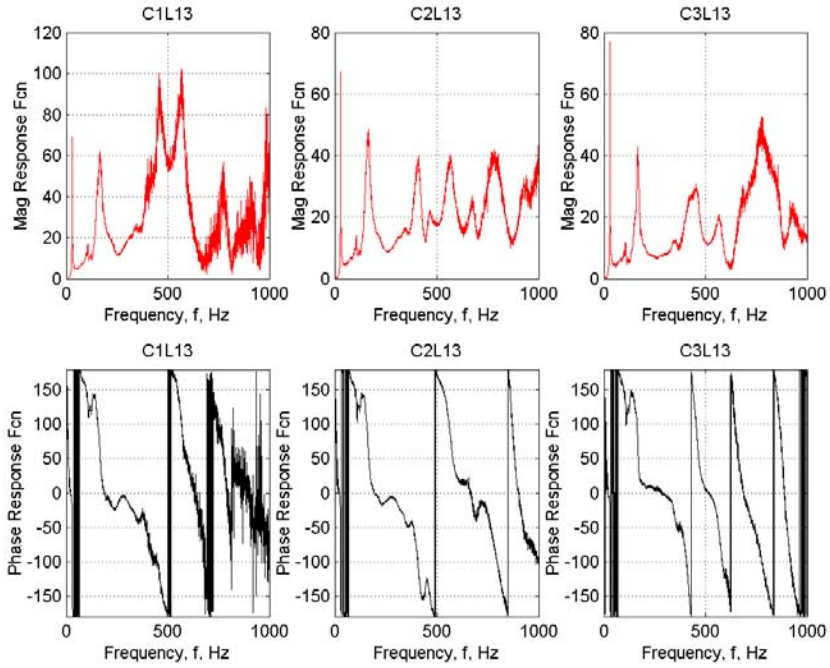

Figure B.11: Accelerometer frequency response functions for points C1L13, C2L13, and C3L13.

Appendix C Jet Characterization Experiment

The functionality of active flow control depends on the uniformity of the jet as it exits the blade. In order to quantify the behavior of the leading edge blowing (LEB) jet and the tangential blowing (TB) jet the velocity field as it leaves the slot. The jet velocity field was characterized in stagnant flow in order to eliminate some of the three dimensional effects and simplify the data collection. This section outlines the experimental apparatus and the results of the jet characterization experiments.

C.1 Experimental Setup

For these tests, as well as the tests on the full assembly, particle image velocimetry (PIV) is used to measure the velocity field within a particular measurement area. PIV involves seeding the flow with small reflective particles that are illuminated in an area by a laser sheet. A high-speed digital camera then records the movement of the particles within the laser sheet. From the particle displacement and the time between camera frames, the velocity of a particle can be calculated. In this case, 10 micron diameter particles were seeded into a small 15 gallon fish tank in which the airfoil was mounted as shown in Figure C.1. The airfoil is mounted between two polycarbonate plates that keep it above the floor of the tank while still allowing optical access for the camera from one side. A dual-head Ng-YAG laser supplies the laser beam. This laser beam is routed and expanded into a sheet by a series of lenses and mirrors. The laser sheet is made as thin as possible in order to minimize the amount of out of plane motion that the camera sees.

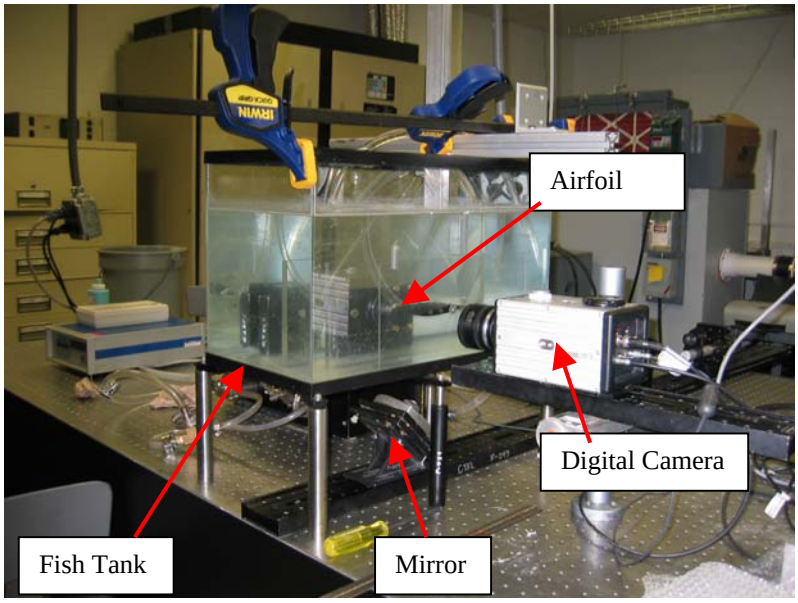

Figure C.1: Picture of the jet characterization assembly. The experiments were performed in the Mechatronics Lab at Virginia Tech

There were two different flow control configuration to be characterized. Each configuration was measured span-wise and chord-wise; see Figure C.2 and Figure C.3, for five different blowing flowrates. The maximum flowrate available was 10 L/min, supplied by two programmable pumps joined in series. The pumps were calibrated using a container with a known volume and a stopwatch. Thus, there were a total of 20 measurement cases run. For each case, a total of 2000 frames were saved. For PIV processing, two frames are used to calculate a particular velocity field at a point in time. Thus, 1000 image pairs were recorded. However, for time-averaged steady flow only 100-200 image pairs need to be processed in order to get a good average flowfield.

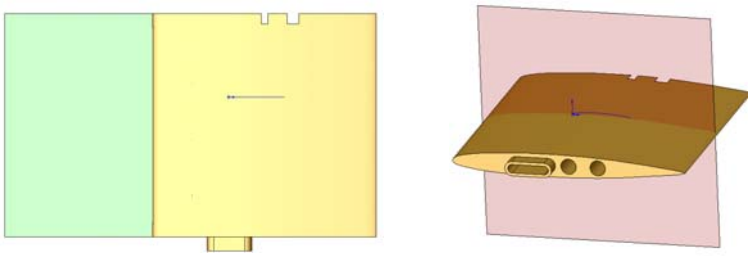

(A) **(B)**

Figure C.2: Diagram of the measurement planes for the jet characterization tests. Picture (a) is the span-wise plane and (b) is the chord-wise plane. The blade is shown in yellow.

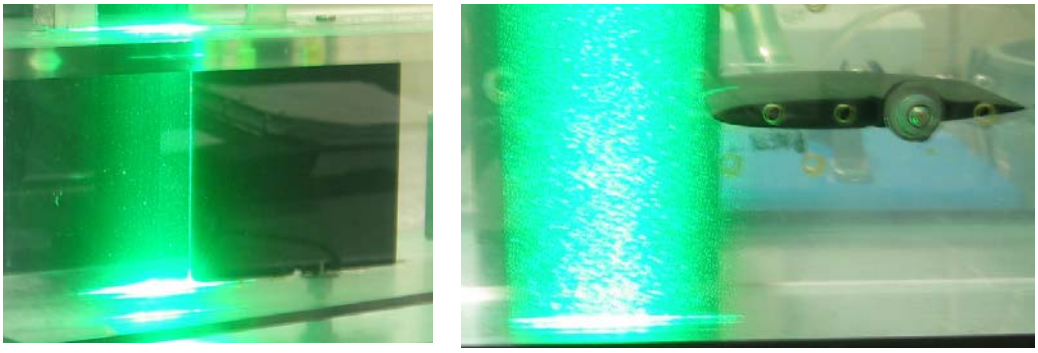

(A) **(B)**

Figure C.3: Picture of the laser planes used. (a) shows the span-wise plane and (b) shows the chord-wise plane.

In order to get accurate velocity data, the time between camera images must the scaled to match the measured flow. If the particle moves too far between two frames, the computer has a difficult time tracking the movement and can yield incorrect data. To minimize this problem, the rule of thumb is that a certain particle should move no more than four pixels between two frames. Thus, a finite time step is chosen to control the pulse of the camera and the laser. Pulsing the laser acts much the same as the flash on a normal camera; it illuminates the particle at only a specific point in time so that the camera does not pick up the motion of the particle, only its position. The pulses of the laser are extremely small, on the order of 10 ns, whereas the exposure time of the camera is on the order of 0.2 ms. This pulse separation is approximated beforehand using the calculated jet velocity, but is confirmed by checking the particle displacement in a between two frames before taking the full data set. The camera and laser are

synchronized by a separate timing system. Figure C.4 shows a schematic of the data flow in the test setup.

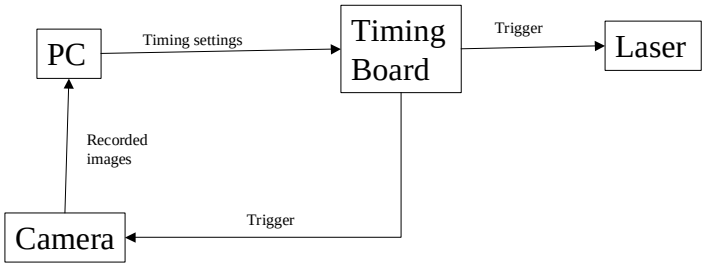

Figure C.4: Schematic of data flow for jet characterization tests.

The other important parameter in PIV experiments is the flow seeding. Too few particles in the flow can create problems in data processing because the computer does not have enough data to work with. On the other hand, if the seeding is too dense, the computer will have difficulty distinguishing one particle from another. To estimate the seeding density, the number of particles found in a 32x32 pixel area on a single camera image is counted. The number of particles should be around 10. Figure C.5 shows one of the raw, unprocessed images for the span-wise measurement.

Figure C.5: An unprocessed image from the spanwise straight leading edge tests.

For each measurement plane, a calibration image is taken. In this calibration image, a ruler is placed in the field of view as a reference scale for the image. This scale is then used to correlate the length of the viewing plane to the number of pixels in the image. This resolution is needed in order to calculate the velocity magnitudes in standard units. Figure C.6 shows the calibration images for the chord-wise leading edge jet measurements and the span-wise tangential jet measurements. Note that the chord-wise measurement has a higher magnification than the span-wise. The reason for this is that the high magnification was able to show more of the jet behavior at the slot. Also, this jet is very thin; therefore, the high magnification is required into ensure that all of the jet behavior is captured.

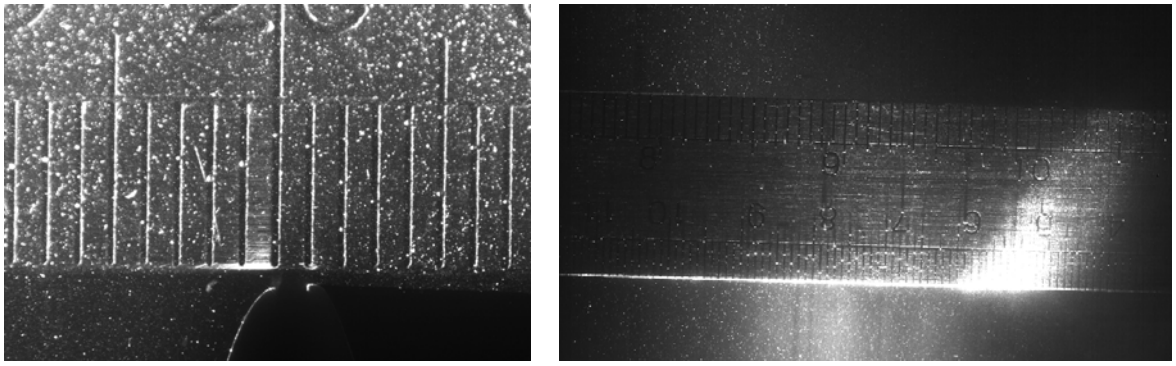

(A) **(B)**

Figure C.6: (a) shows the calibration image for the chord-wise straight measurements, the small increments shown are millimeters. (b) shows the calibration image for the span-wise tangential measurements. The same ruler was used in both calibrations. Note that the magnification is much higher in the chord-wise measurements.

The series of images saved from the camera are processed in a program called FlowIQ that pairs the image frames, measures the particle velocities according to user-defined settings, and maps them onto a designated grid. The settings for this processor vary depending on the acquisition rate and the experiment itself. The data is then output as a data file that can be plotted in TecPlot. An additional post-processing tool is known as 3PI. This program, written by Dr. Vlachos, is capable of averaging many data sets together to form a single average flowfield. It is also able to calculate flow quantities such as vorticity and shear stress from the velocity fields.

Using the above programs, the first round of processing was conducted on all of the datasets. The results were lightly filtered in order to remove any bad vectors created by

correlation errors. Figure C.7 shows the difference between the velocity vectors before and after filtering. It was vital that the data be filtered enough to remove the bad data, but not oversmoothed. Over-filtering the data can distort the results. As can be seen from Figure 6, the only difference between the two flowfields is the bad vectors. Once filtered results were computed, the results could then be averaged into a single flowfield. This could be done because the tests were conducted using steady blowing. While there will be some time-dependent variation in the jet, the system was allowed to run long enough at a steady state that this variation was negligible. The time-accurate interaction of the jet with freestream flow will be measured in subsequent tests.

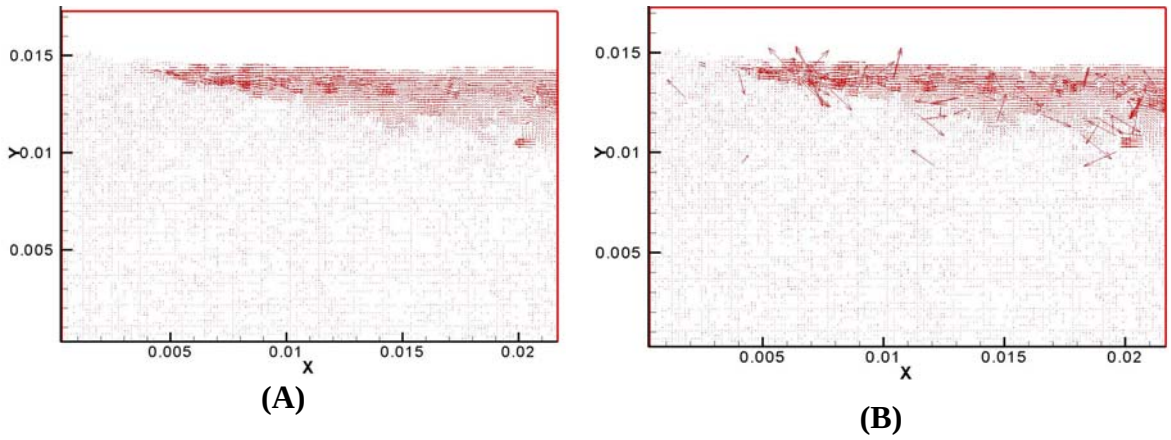

Figure C.7: Filtered (A) and unfiltered (B) vector data of the tangential jet.

C.2 PIV Results

Using Dr. Vlachos' 3PI program to compute the average properties of the blowing jets were analyzed to determine the effectiveness of the designs. The straight leading edge jet was fairly straightforward. As can be seen from Figure C.8 the jet behaves much as expected for a jet in a quiescent fluid. The major design issue in this blowing configuration was the addition of turning vanes to the interior plenum. The goal of this was to create a more uniform span-wise velocity distribution at the exit. This preliminary design proved to be moderately effective.

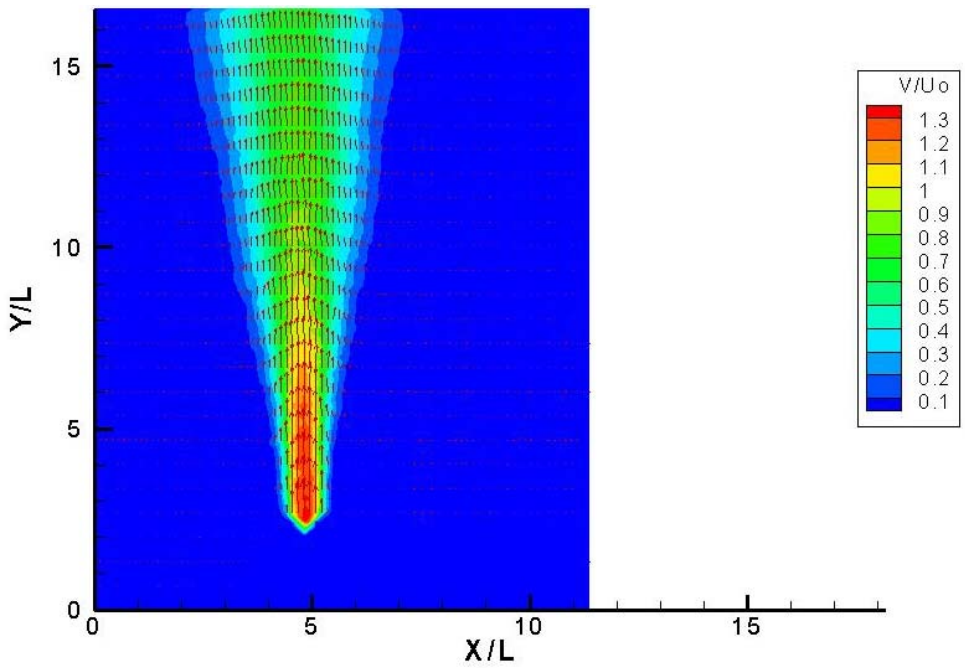

Figure C.8: Cross-section of the time-average jet velocity non-dimensionalized by the ideal average velocity (U_0 = 1.221 m/s) and the slot height (L = 1.02 mm) measures by the chord-wise plane. The contours show the jet velocity component in the y-direction.

The velocity distribution should small spikes that corresponded to the turning vanes. Figure C.9 shows an image overlay of the velocity field and the solid model of the EGV. The spikes in velocity contours match the turning vanes very closely, expect for the end closest to the supply. This drop in velocity towards the edge is most likely cause by poor placement of the first turning vane. The fluid is not guided to the end of the slot as effectively as elsewhere. As can be seen from the figure, the first turning vane is roughly in line with the edge of the slot. However, moving the vane further into the slot area would not completely solve the problem. The first vane would then have the potential for blocking the other two turning vanes.

In this design, the vanes are equally spaced across the length of the slot. The intention was that then equal amounts of fluid would be supplied to each region. Also, noteworthy is the regions of higher velocity around the third vane. A likely explanation for this behavior is flow separation on the back side of the second turning vane. A similar pattern appears around the second vane, likely caused by the separation region behind the first vane. This could be corrected by using a less sharp turn. In this case there were space constraints that prevented lengthening the plenum in order have a shallower turn. For the case shown, the volume flowrate was 6.6 L/min. In order to gain a better understanding of the flow physics, the data was plotted

on a non-dimensional system. Using the flowrate and the slot height, the ideal average velocity was calculated using mass conservation. These values were then used as the reference values to non-dimensionalize the data.

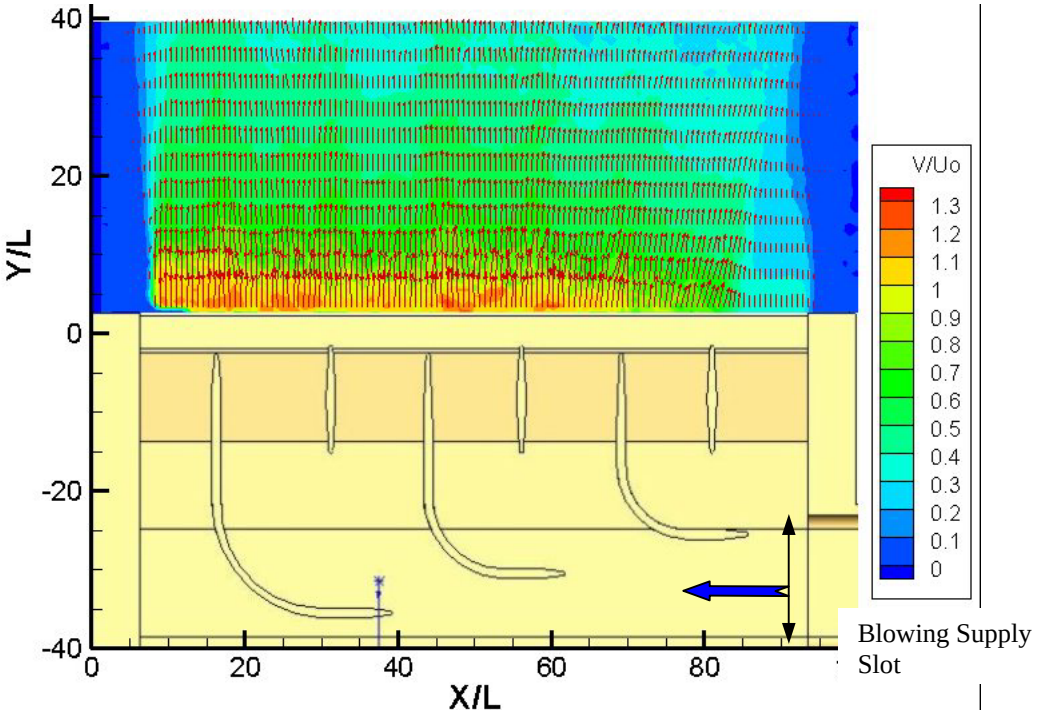

Figure C.9: Image overlay of the average spanwise velocity distribution (nondimensionalized by slot height, L = 1.02 mm and ideal mean velocity, U_0 = 1.221 m/s) and the interior geometry of the blade. The contours show the nondimensionalized velocity component in the y-direction.

The tangential blowing configuration underwent the same examination. The jet remained attached to the blade surface for an inch, see Figure C.8. The velocity fields that are shown have an average flowrate of 6.6 L/min. While this means that the jet is worked as desired, it makes the span-wise measurement more difficult.

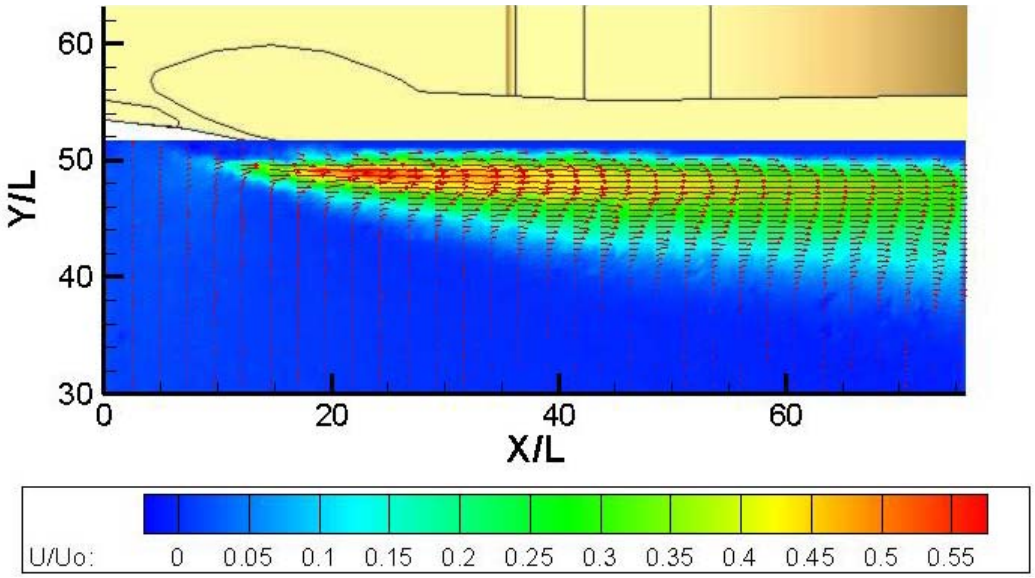

Figure C.10: An image overlay of the tangential slot velocity field. These measurements were taken in the chord-wise plane and time averaged. The contours show the nondimensional velocity component in the x-direction. The data was nondimensionalized by the slot height, L, and the ideal average velocity, U_0, 0.279 mm and 1.11 m/s, respectively.

The spanwise plane had to be positioned tangent to the slot while still within the jet region. This proved to be extremely difficult because the jet is only 2 mm thick and the laser plane had a minimum thickness of 1 mm. The thin jet thickness combined with the surface curvature meant that the spanwise velocity distribution could not be measured directly at the slot. The measurements were taken beginning at 11 mm downstream of the slot. Figure C.11 shows an overlay of one of the measurement images with the unfiltered velocity field. The slot is highlighted show that the velocity field was not able to be resolved at the slot. The bad vectors in the upper left hand corner are vectors with poor correlation due to uneven illumination at the edge of the plane. However, despite these problems the data within a 28 mm band the PIV measurements give a picture of the velocity profile as jet exits the blade. This velocity field for the 6.6 L/min case is shown in Figure C.12. The negative velocity indicates that the flow is moving from right to left. Individual wakes from the turning vanes are not as obviously visible as in the LEB geometry

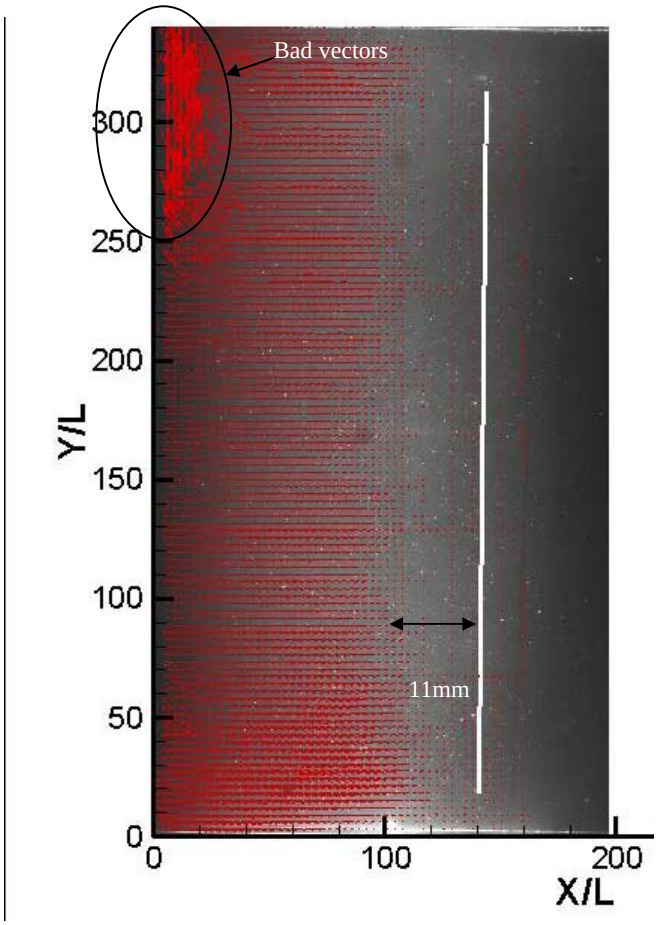

Figure C.11: Image overlay of the unfiltered velocity field on a measurement image. The slot is highlighted in white. Due to the thinness of the jet and the airfoil curvature, the jet could not be measured until approximately 11 mm downstream of the slot.

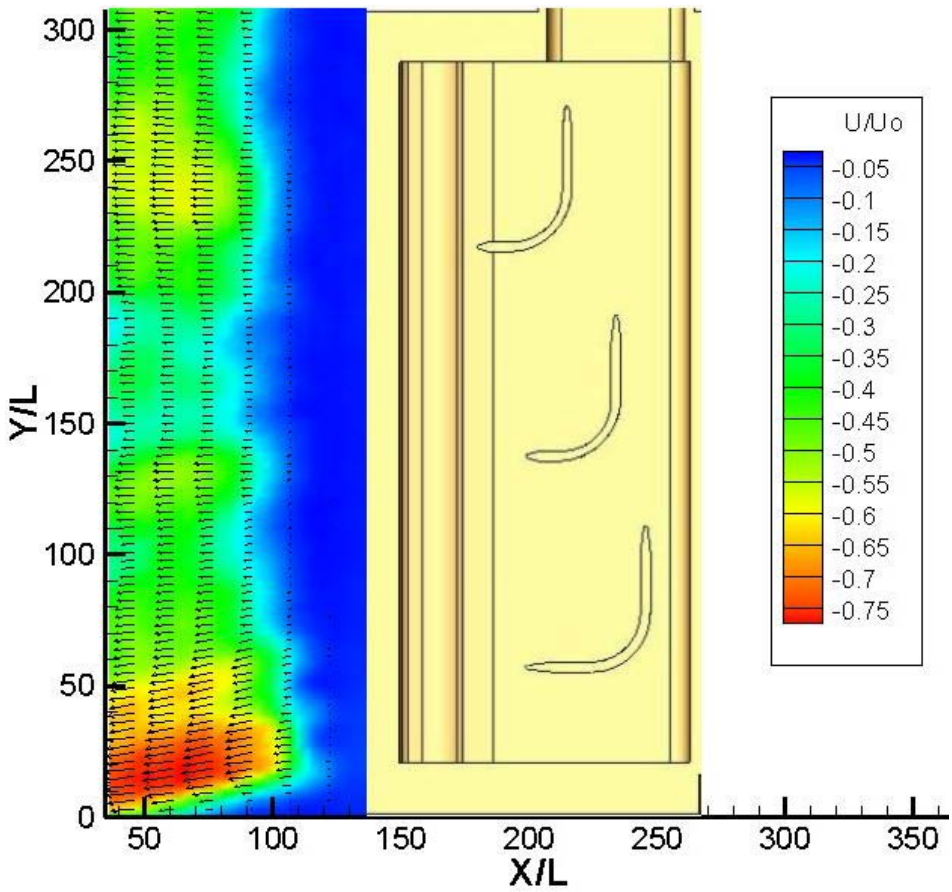

Figure C.12: An image overlay of the tangential slot velocity field. These measurements were taken in the span-wise plane and time averaged. The contours show the nondimensional velocity component in the y-direction. The data was nondimensionalized by the slot height, L, and the ideal average velocity, U_0, 0.279 mm and 1.11 m/s, respectively.

Appendix D LEB and TB Experimental Data

This appendix shows select autospectrum plots and all BPF forcing magnitude plots of the force gauge, accelerometer, and strain gauges results for both the LEB and TB experiments.

D.1 LEB Experimental Data

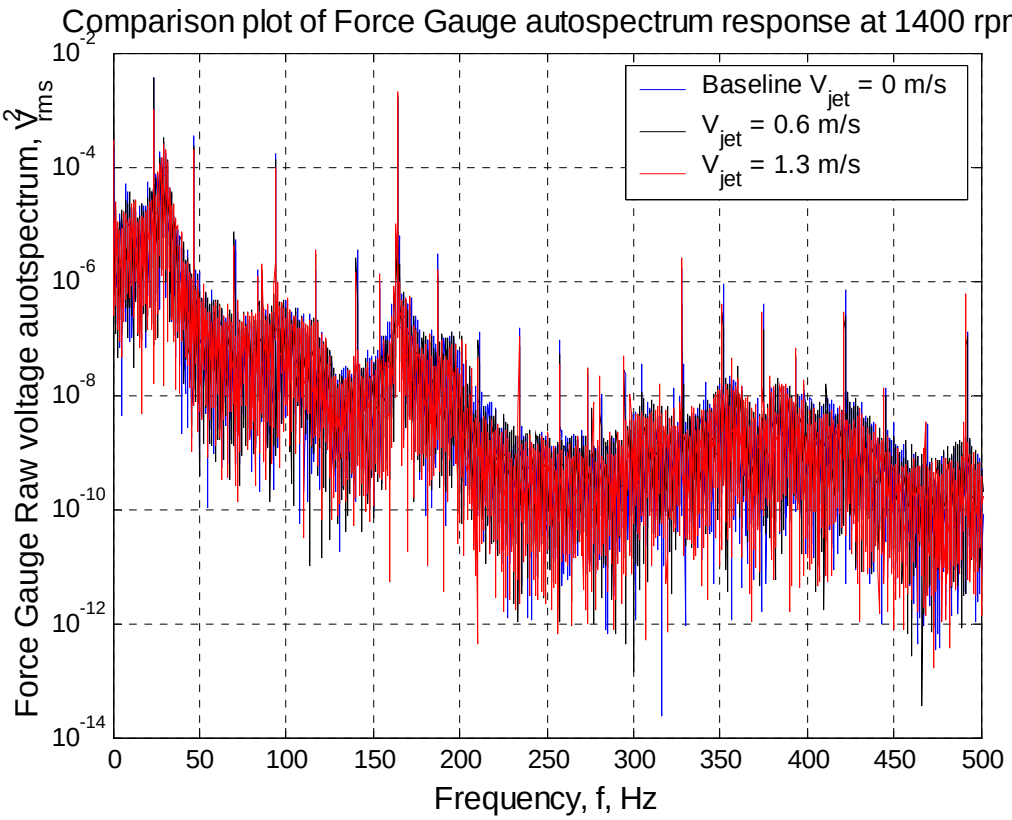

Figure D.1: Force gauge autospectrum at 1400 rpm for three different flow control jet velocities

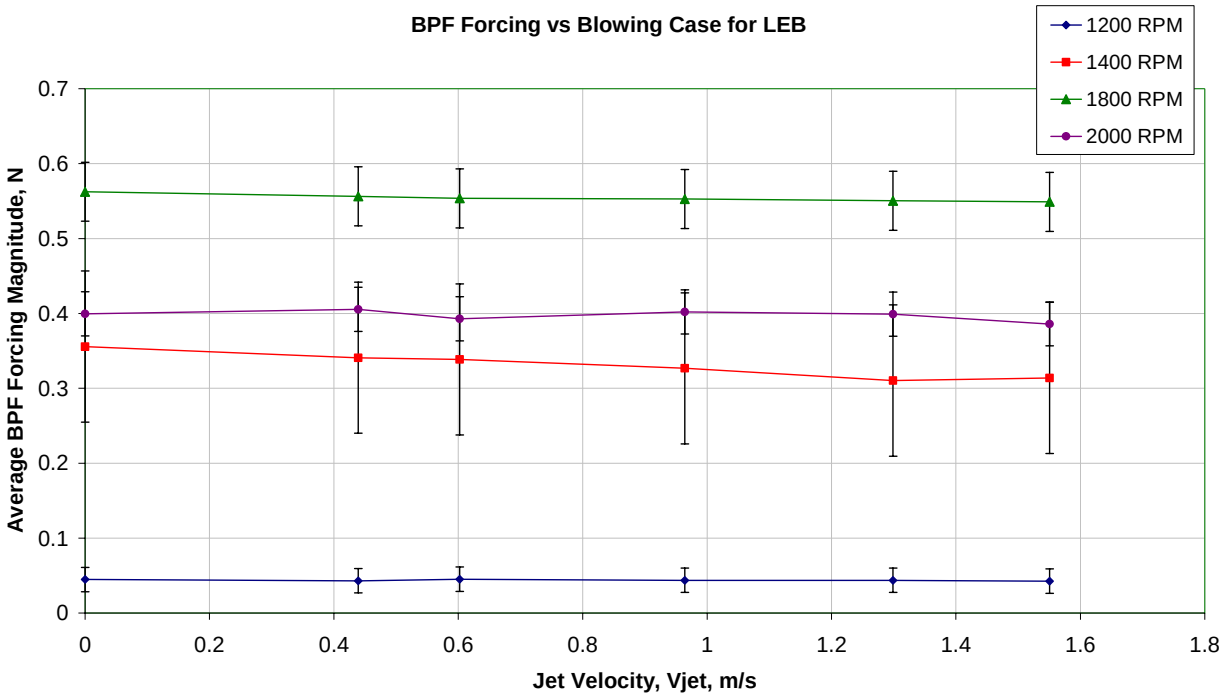

Figure D.2: Average BPF forcing magnitude for the LEB flow control

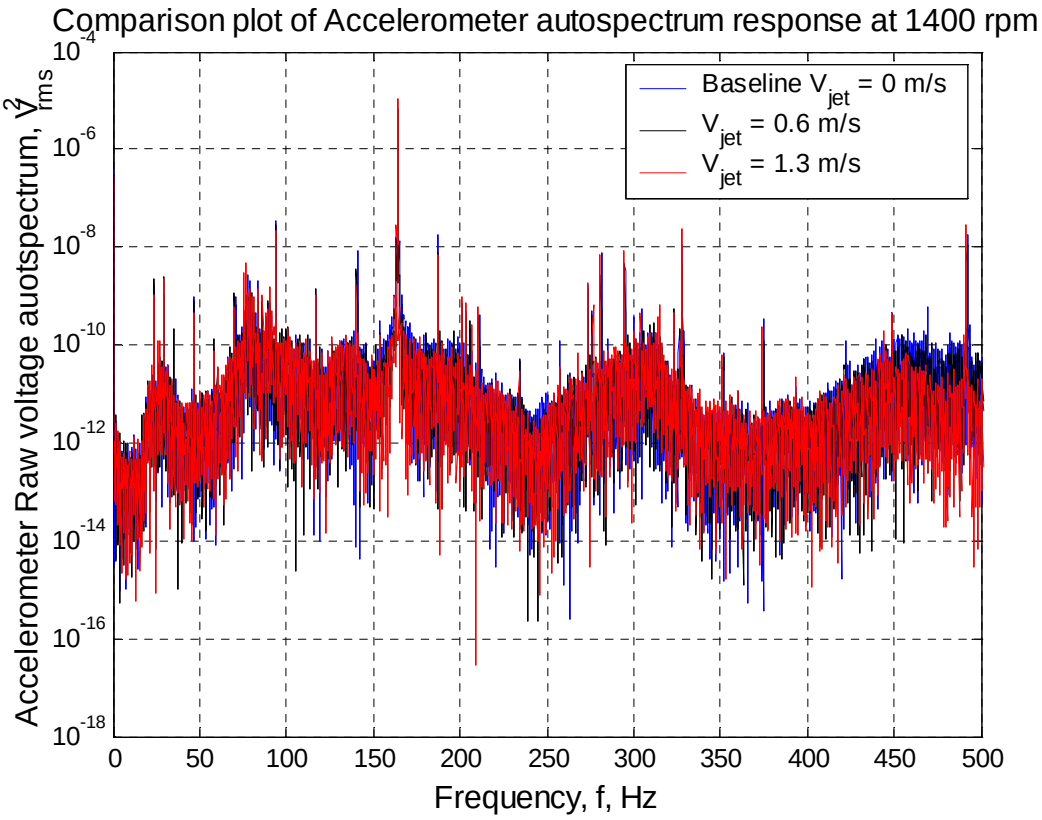

Figure D.3: Accelerometer autospectrum at 1400 rpm for three different flow control jet velocities

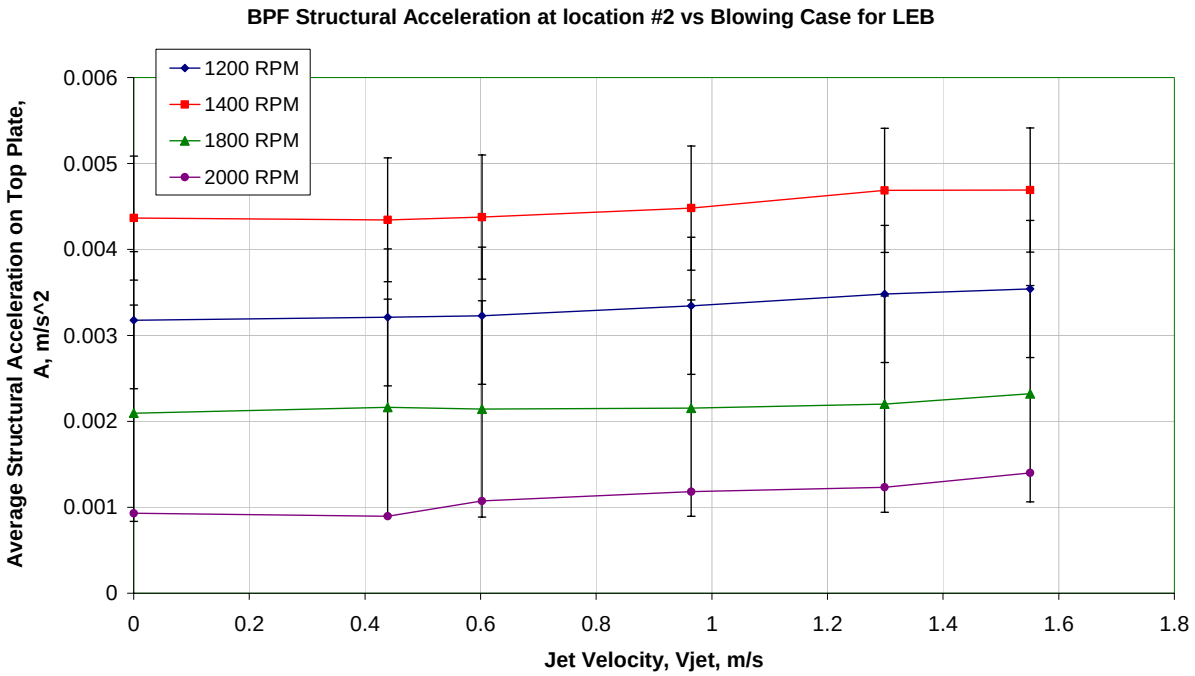

Figure D.4: Average BPF acceleration magnitude for the LEB flow control

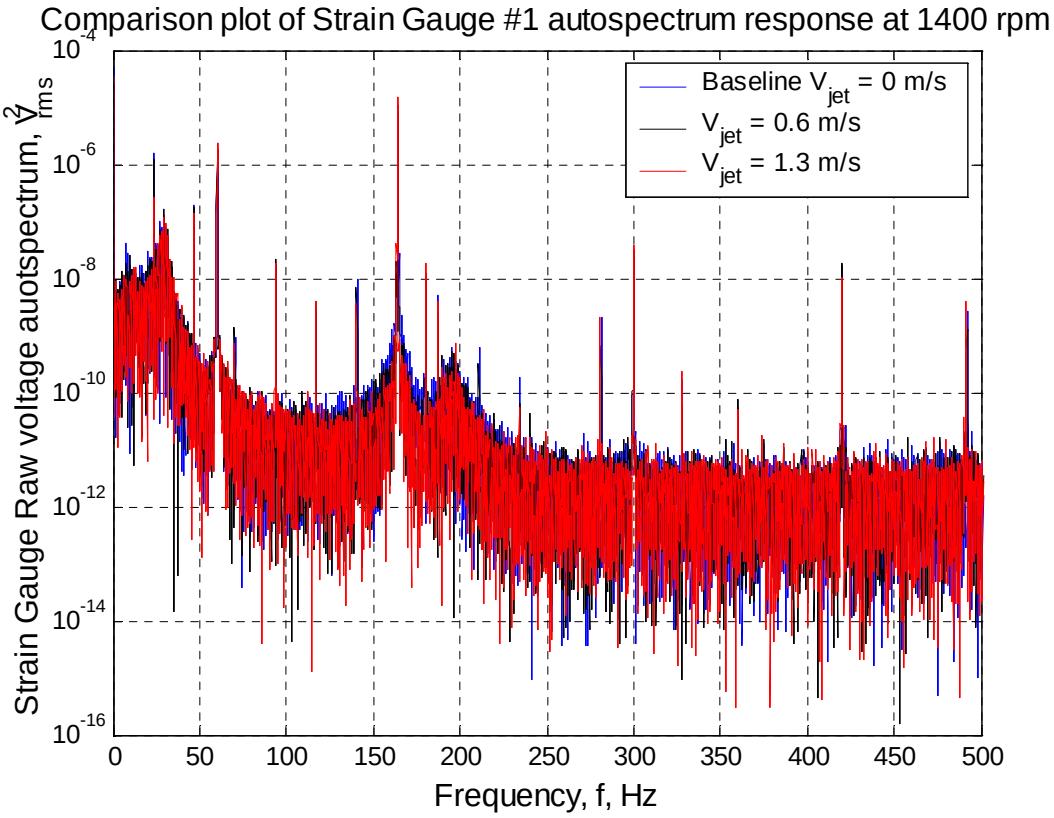

Figure D.5: Strain gauge #1 autospectrum at 1400 rpm for three different flow control jet velocities

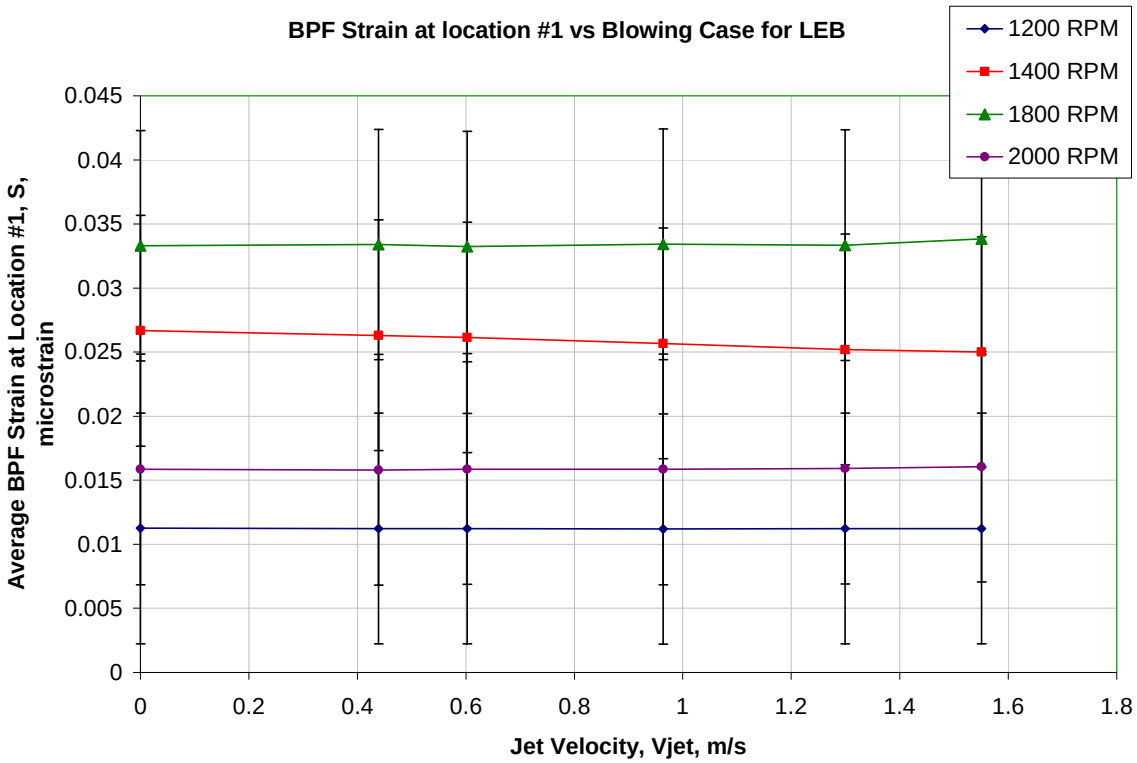

Figure D.6: Average BPF strain magnitude at location #1 for the LEB flow control

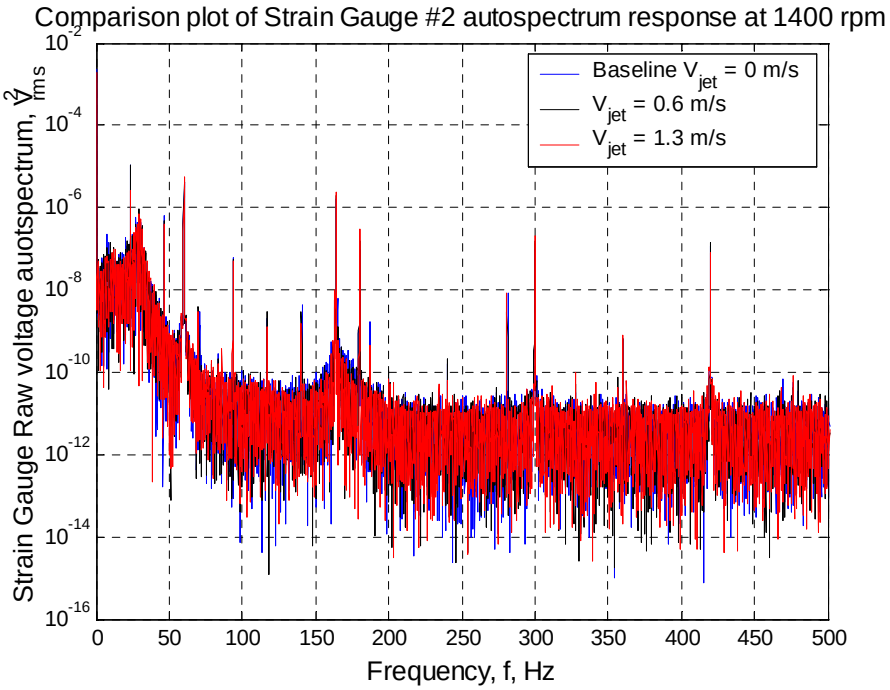

Figure D.7: Strain gauge #2 autospectrum at 1400 rpm for three different flow control jet velocities

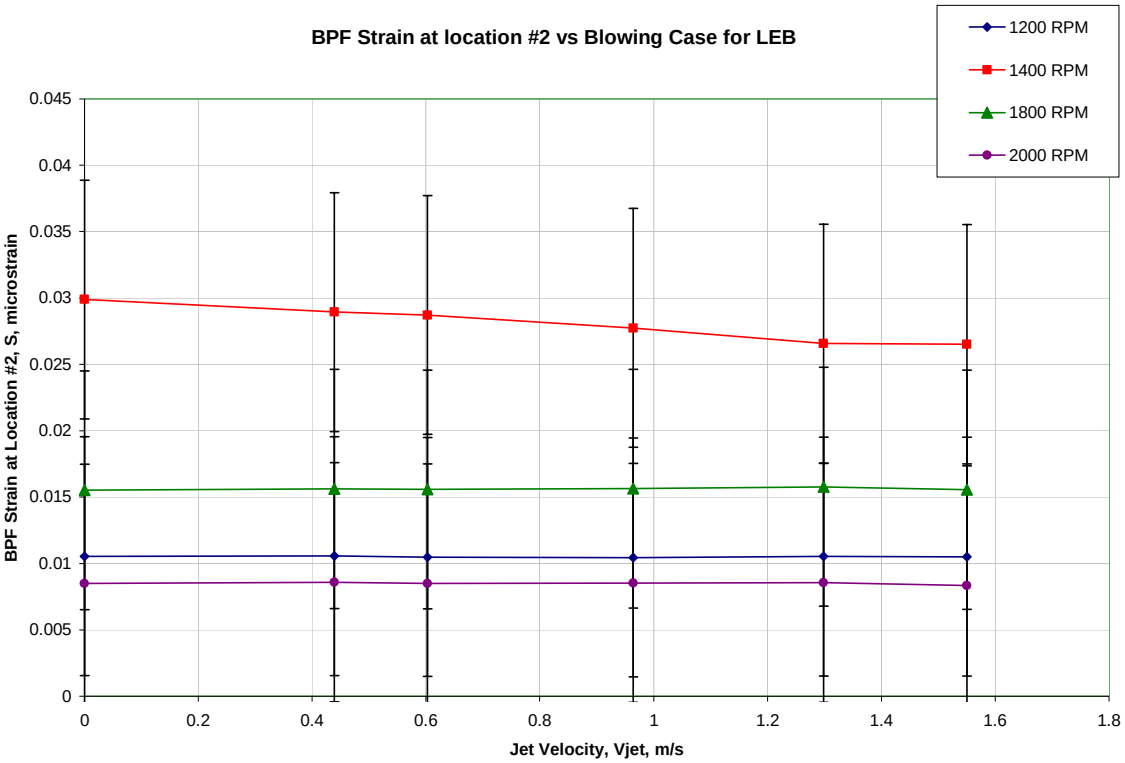

Figure D.8: Average BPF strain magnitude at location #2 for the LEB flow control

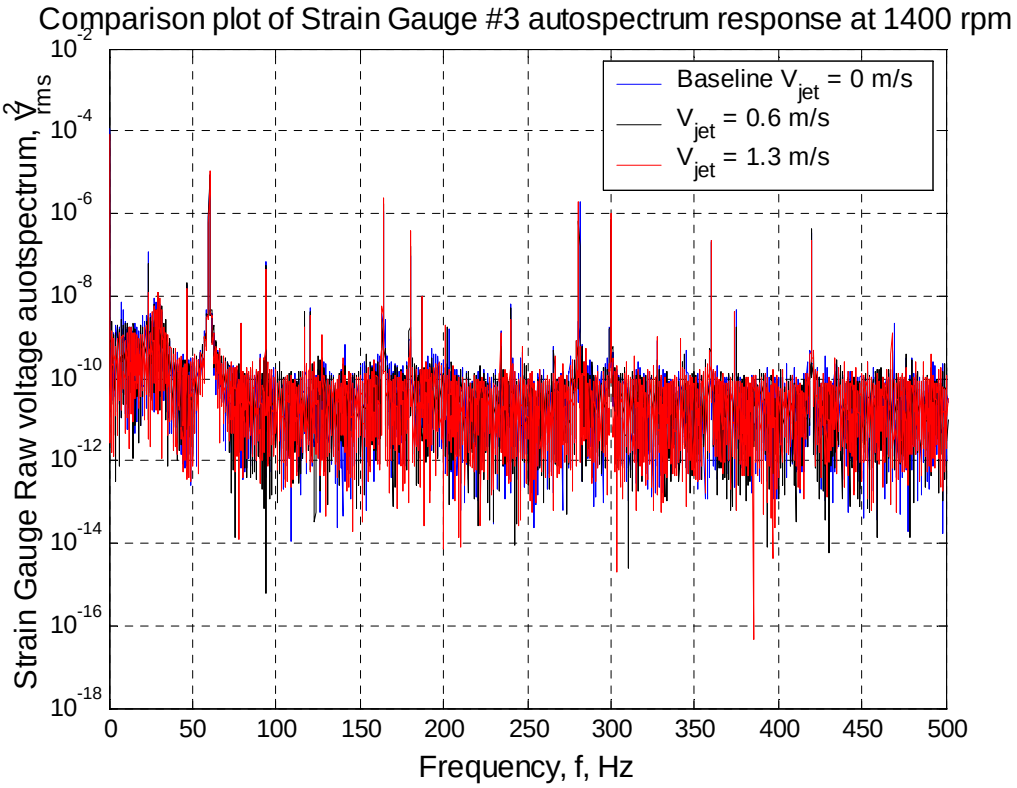

Figure D.9: Strain gauge #3 autospectrum at 1400 rpm for three different flow control jet velocities

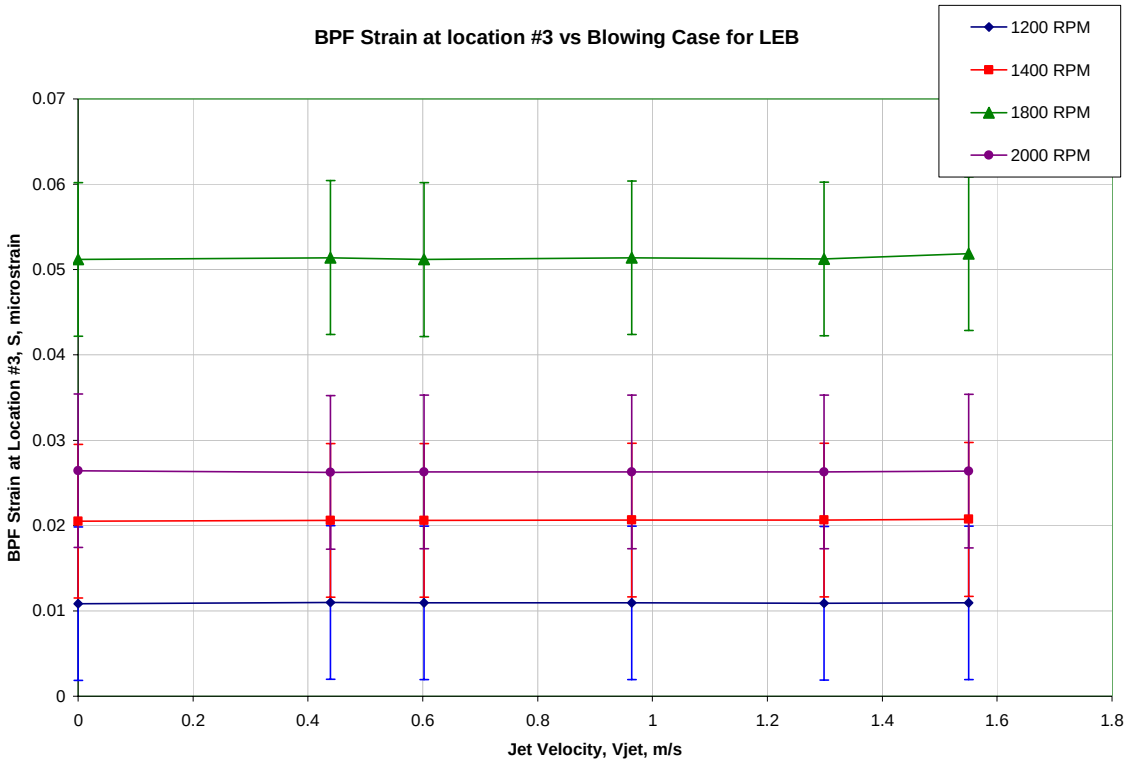

Figure D.10: Average BPF strain magnitude at location #3 for the LEB flow control

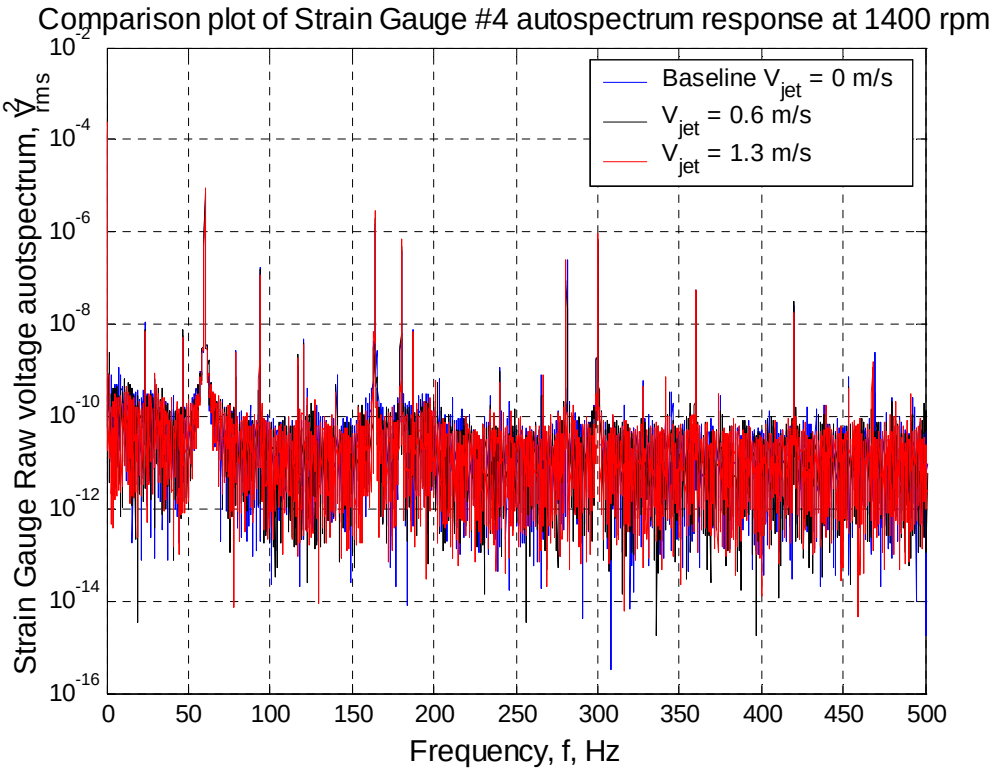

Figure D.11: Strain gauge #4 autospectrum at 1400 rpm for three different flow control jet velocities

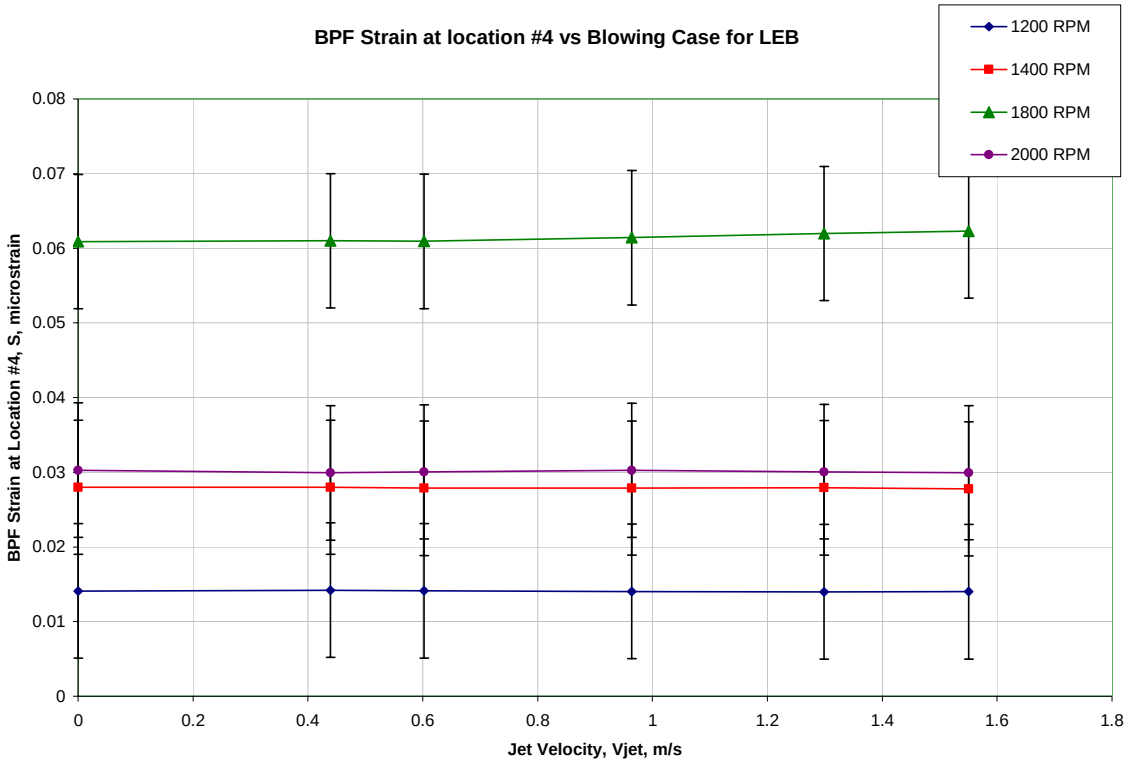

Figure D.12: Average BPF strain magnitude at location #4 for the LEB flow control

D.2 TB Experimental Data

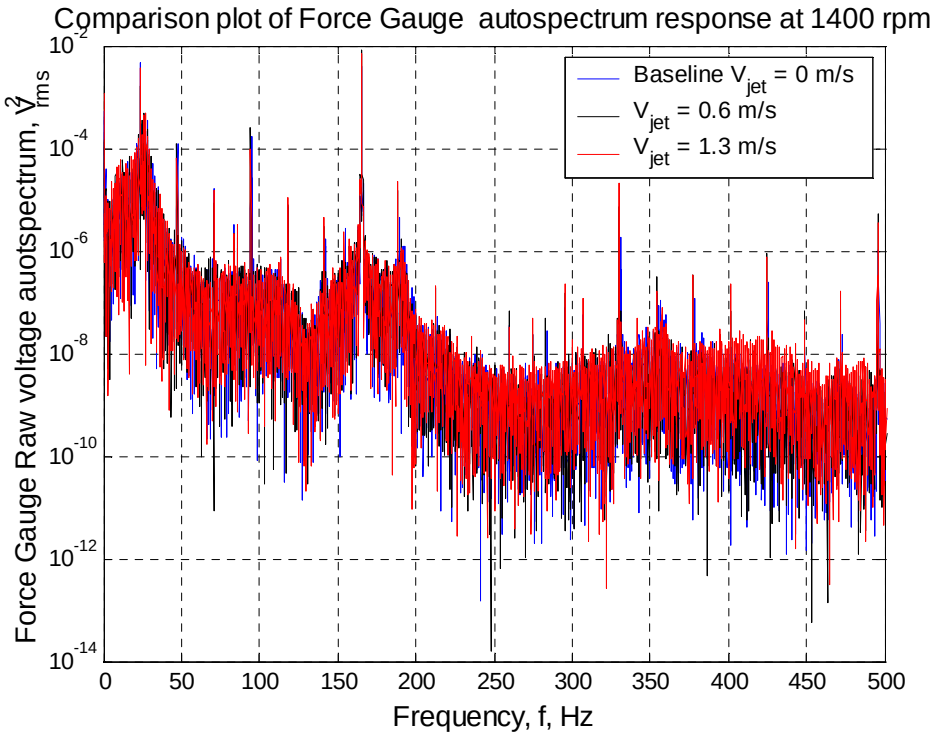

Figure D.13: Force gauge autospectrum at 1400 rpm for three different flow control jet velocities

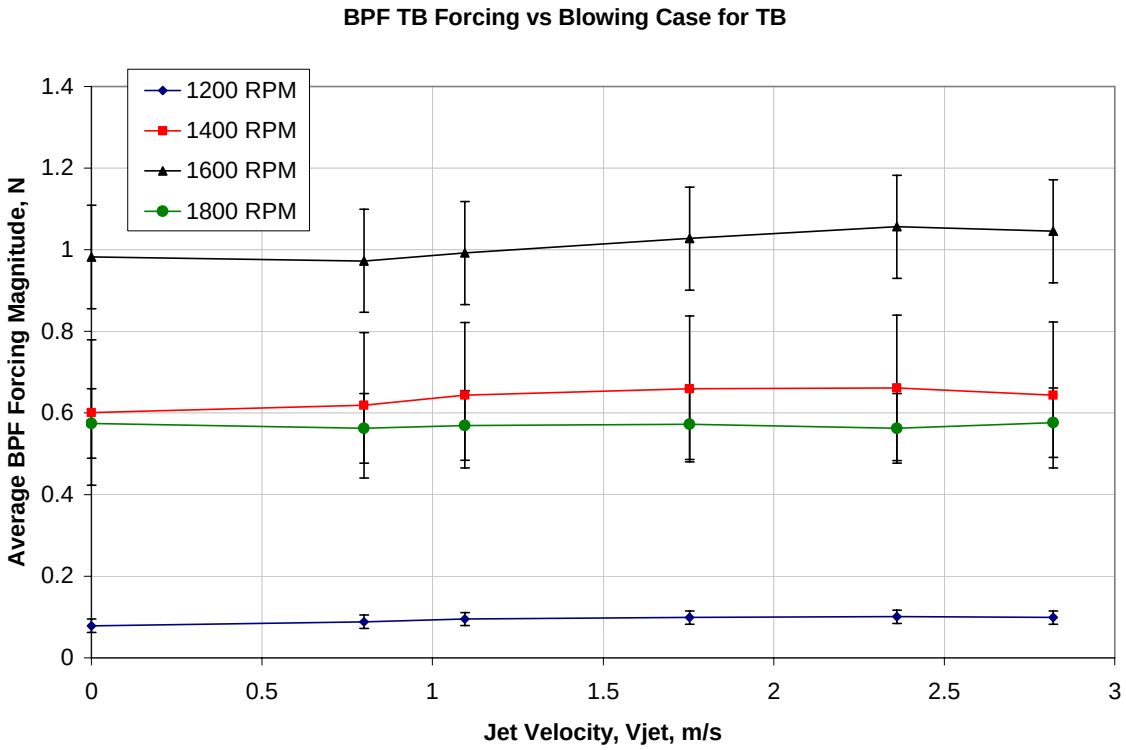

Figure D.14: Average BPF forcing magnitude for the TB flow control

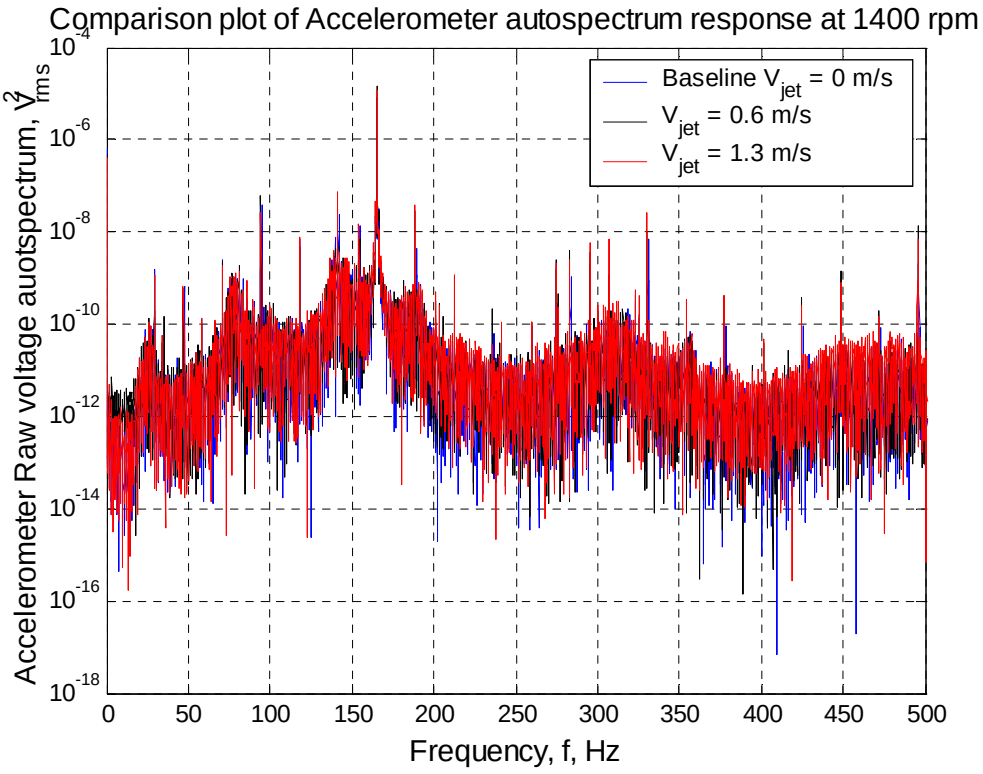

Figure D.15: Accelerometer #2 autospectrum at 1400 rpm for three different flow control jet velocities

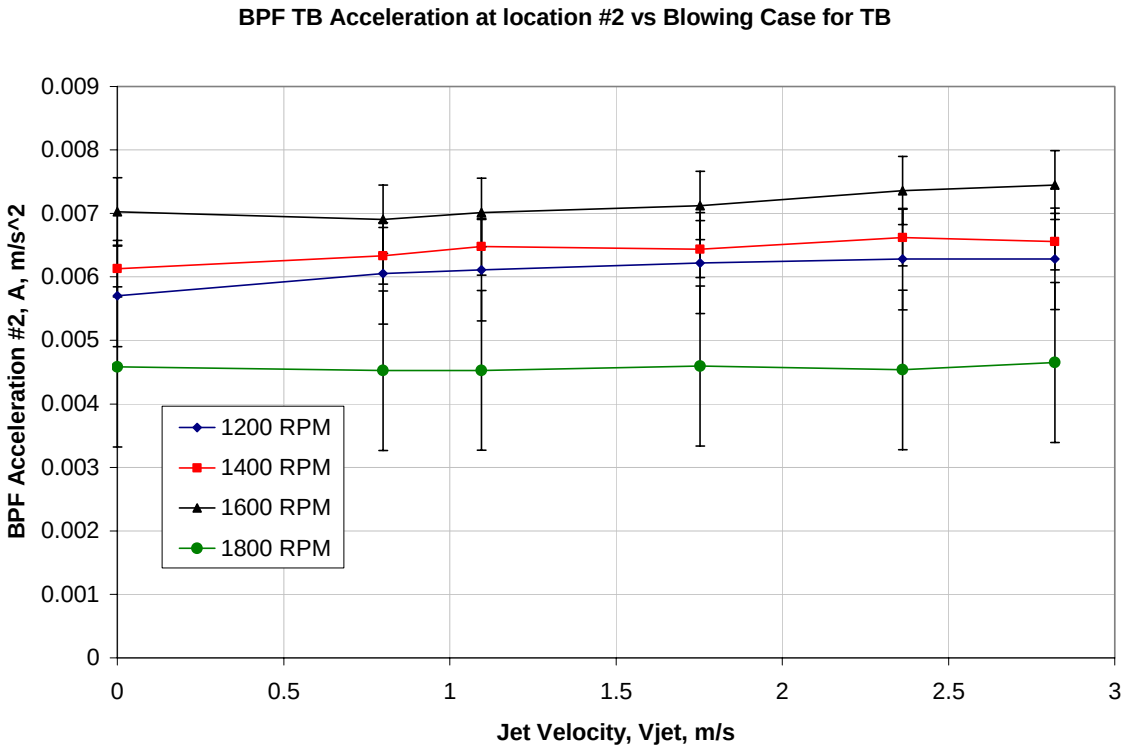

Figure D.16: Average BPF acceleration magnitude for the TB flow control

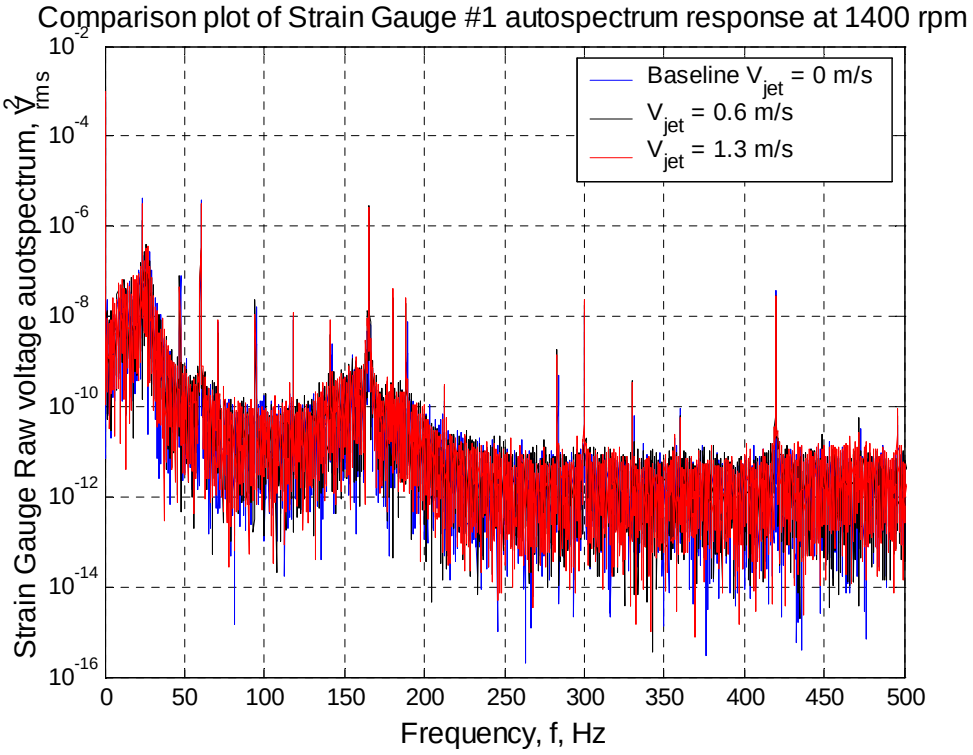

Figure D.17: Strain gauge #1 autospectrum at 1400 rpm for three different flow control jet velocities

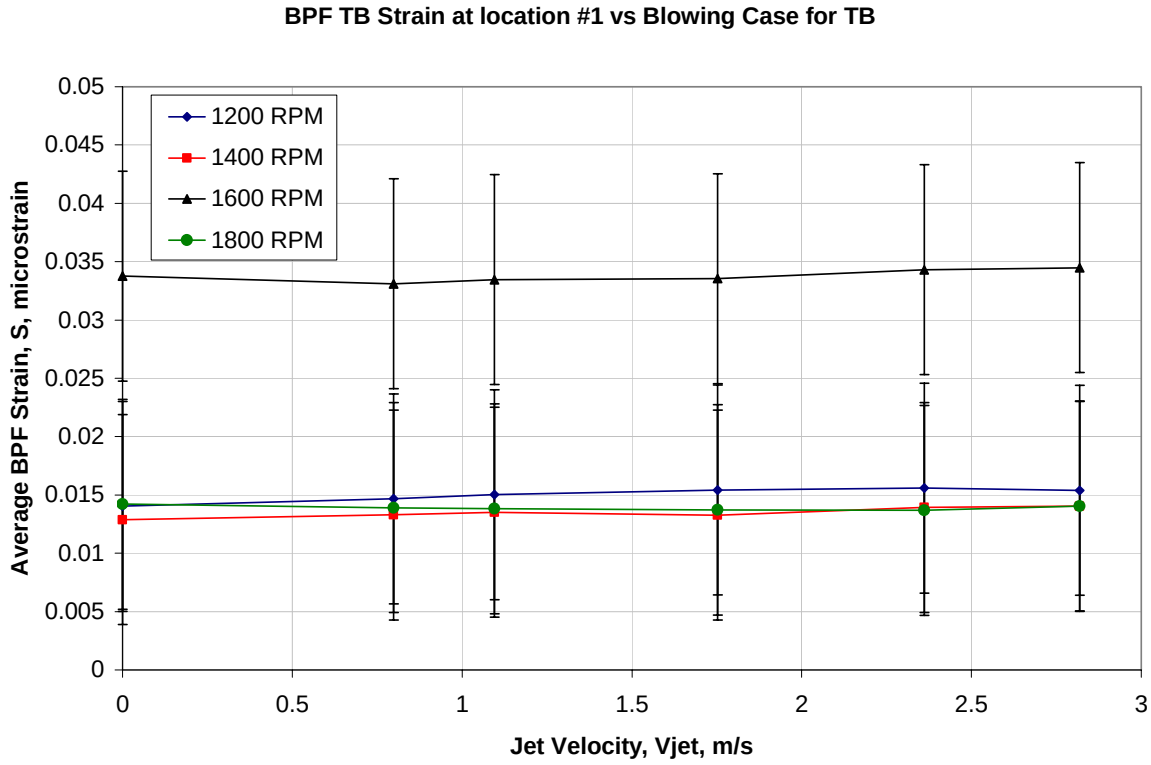

Figure D.18: Average BPF strain magnitude at location #1 for the TB flow control

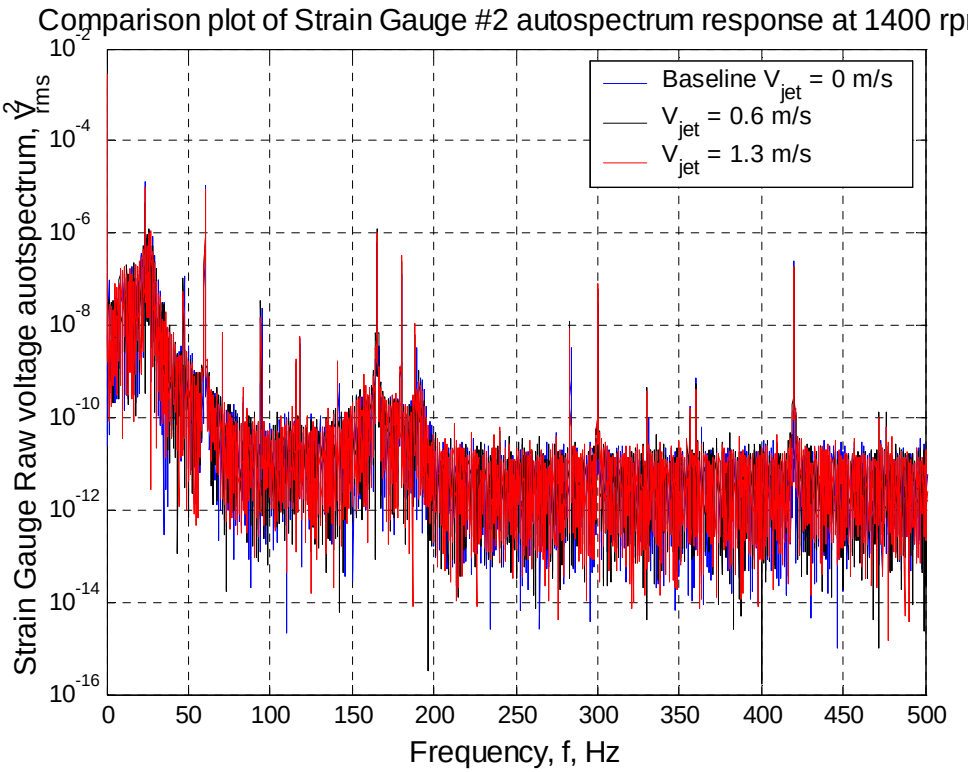

Figure D.19: Strain gauge #2 autospectrum at 1400 rpm for three different flow control jet velocities

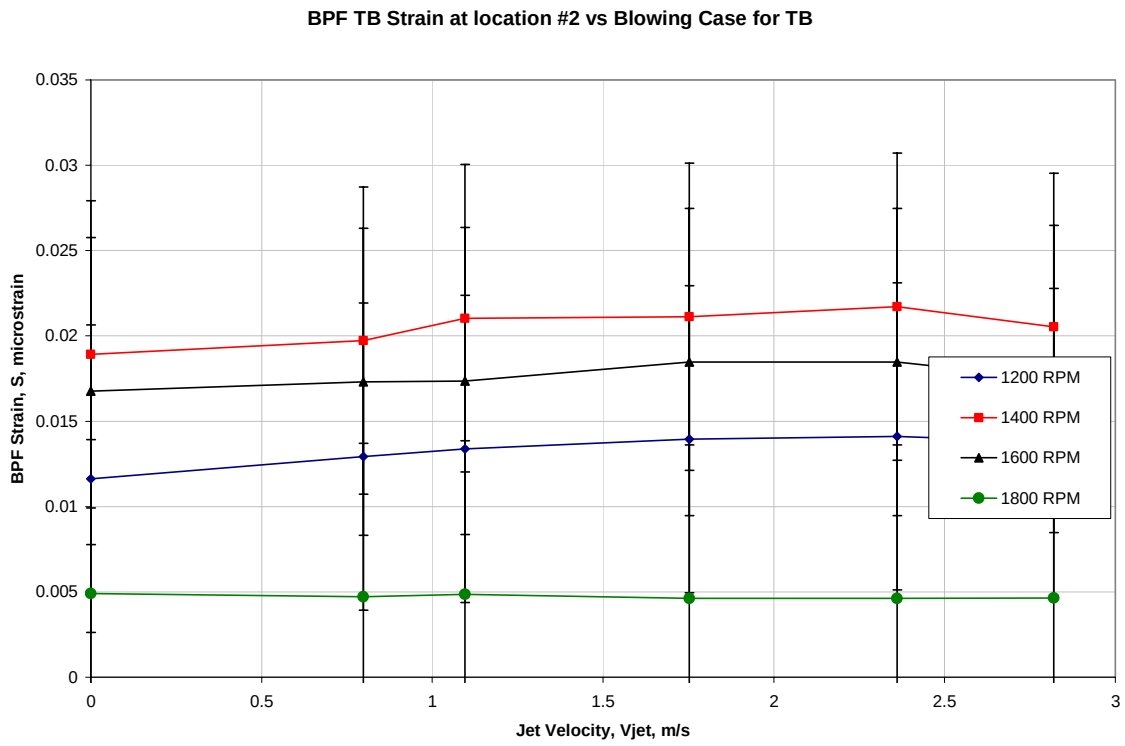

Figure D.20: Average BPF strain magnitude at location #2 for the TB flow control

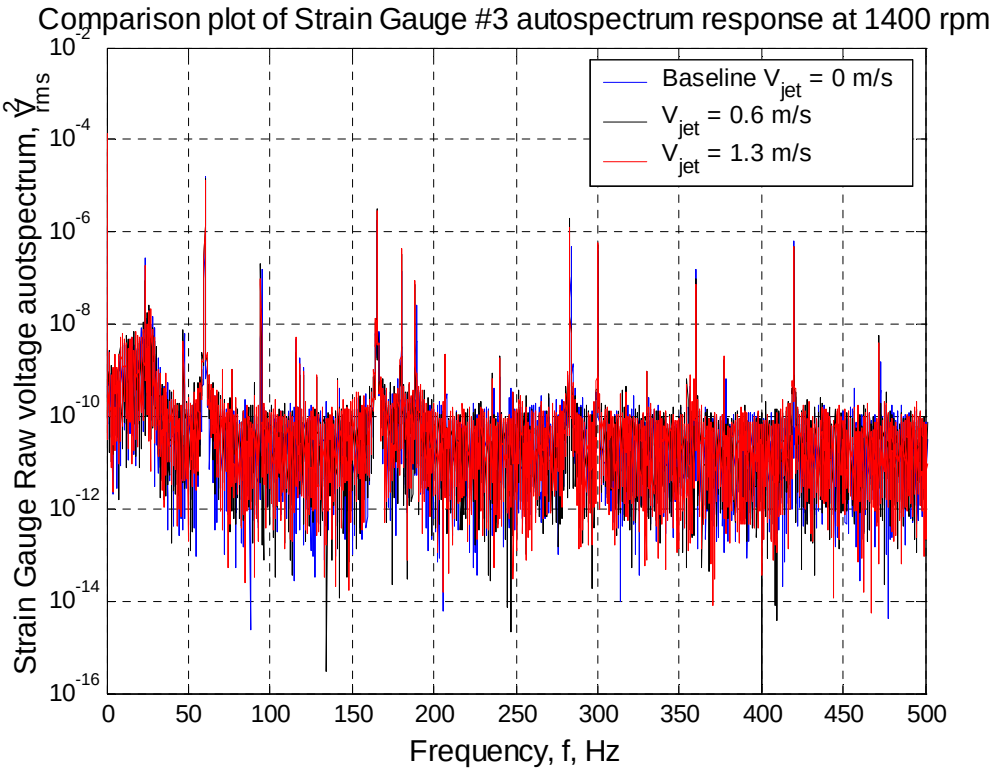

Figure D.21: Strain gauge #3 autospectrum at 1400 rpm for three different flow control jet velocities

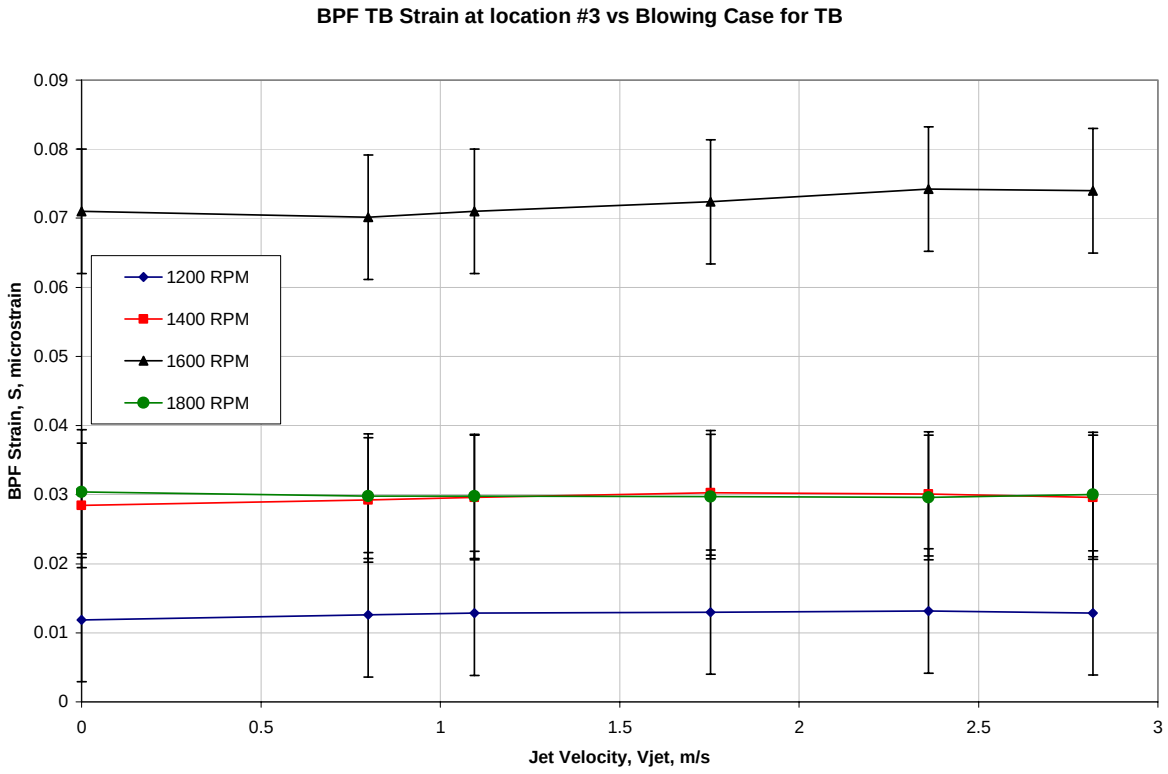

Figure D.22: Average BPF strain magnitude at location #3 for the TB flow control

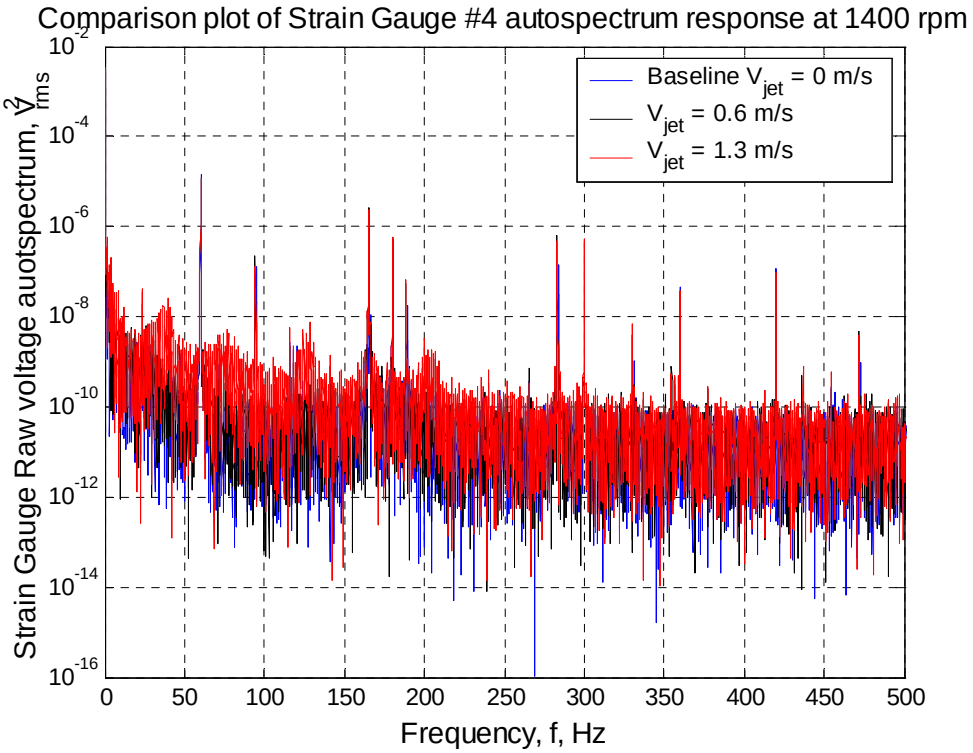

Figure D.23: Strain gauge #4 autospectrum at 1400 rpm for three different flow control jet velocities

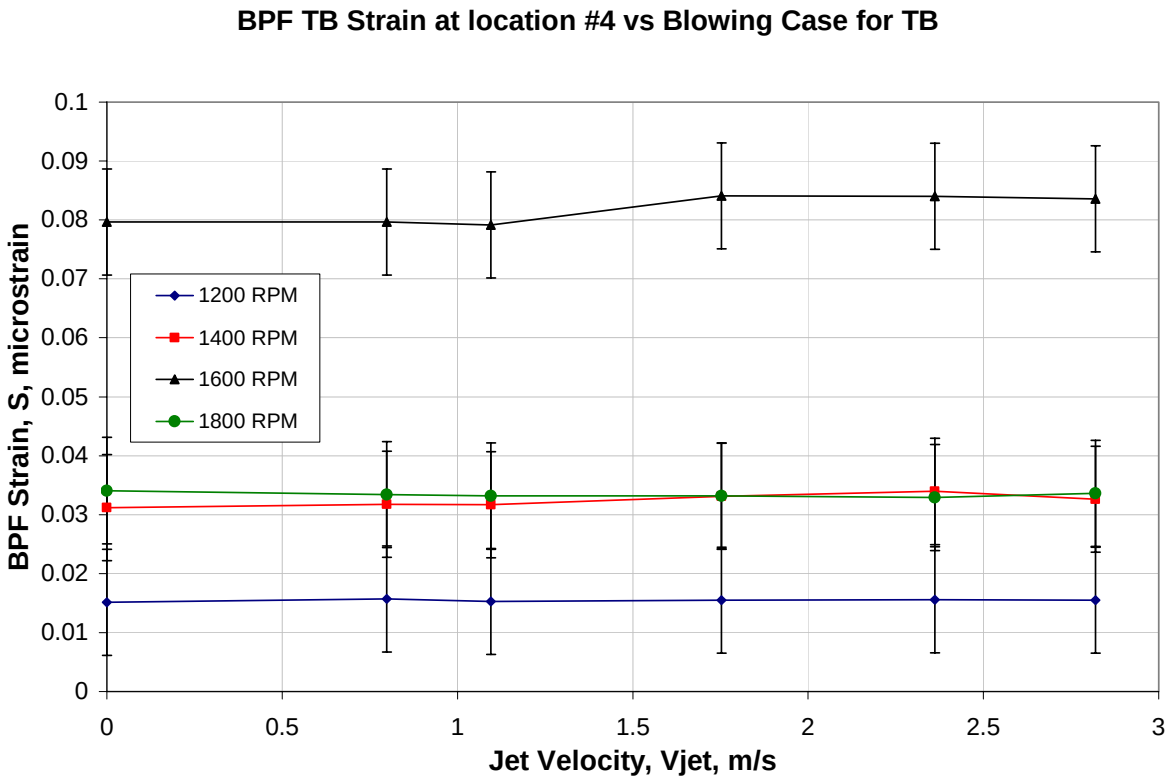

Figure D.24: Average BPF strain magnitude at location #4 for the TB flow control

Appendix E Self-Pumping Rotor Experimental Data

This appendix shows select autospectrum plots of the force gauge, accelerometer, and strain gauges results for both the self-pumping rotor experiments.

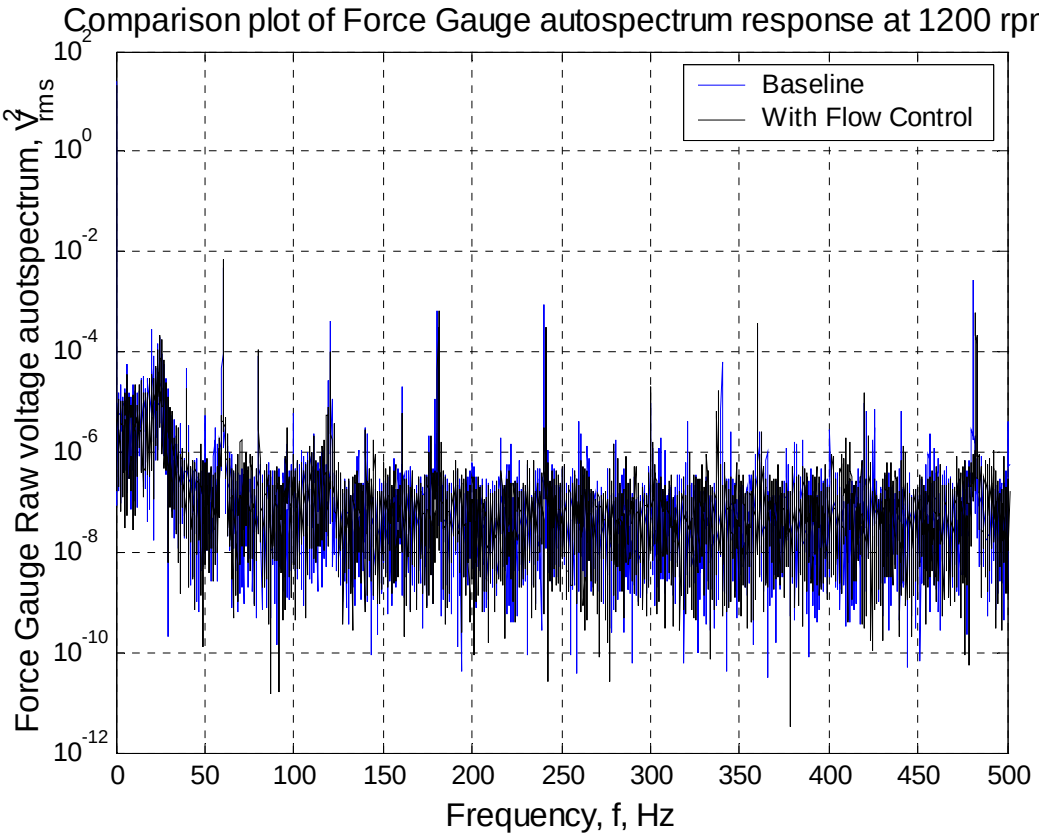

Figure E.1: Force gauge autospectrum for Case 1 trailing edge slot thickness

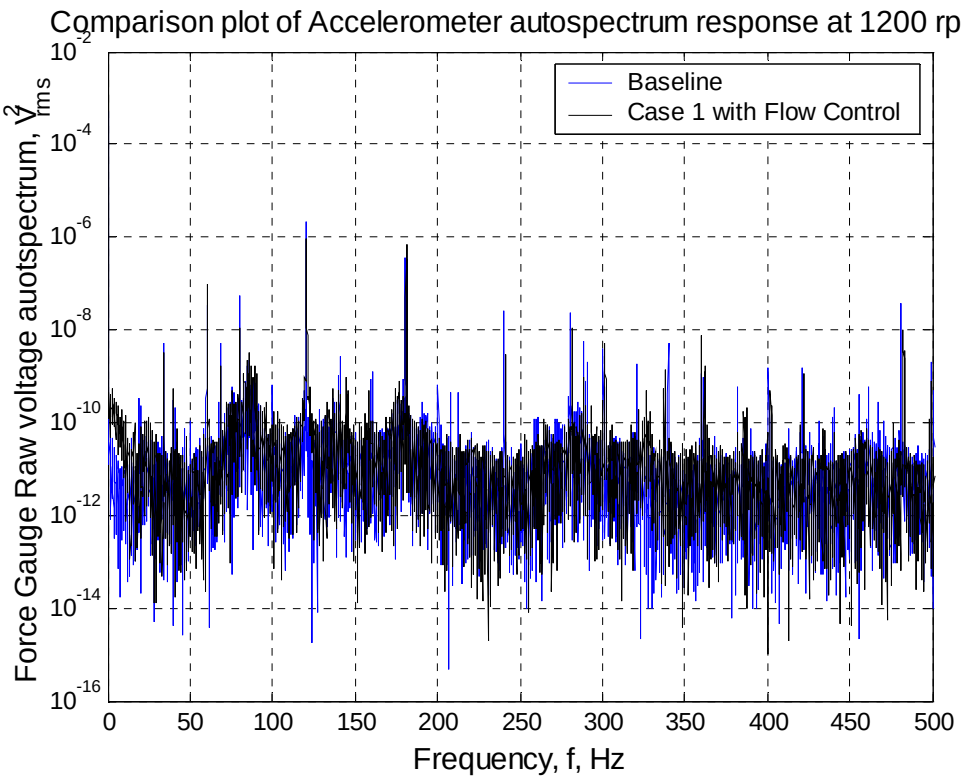

Figure E.2: Accelerometer autospectrum for Case 1 trailing edge slot thickness

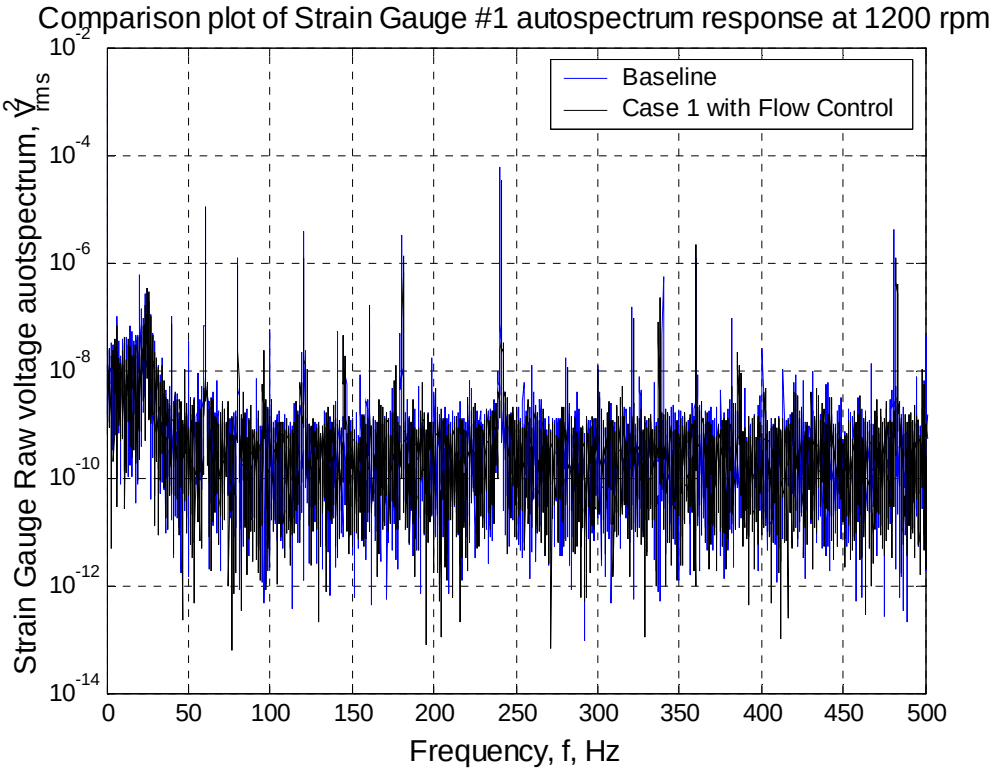

Figure E.3: Strain gauge # 1 autospectrum for Case 1 trailing edge slot thickness

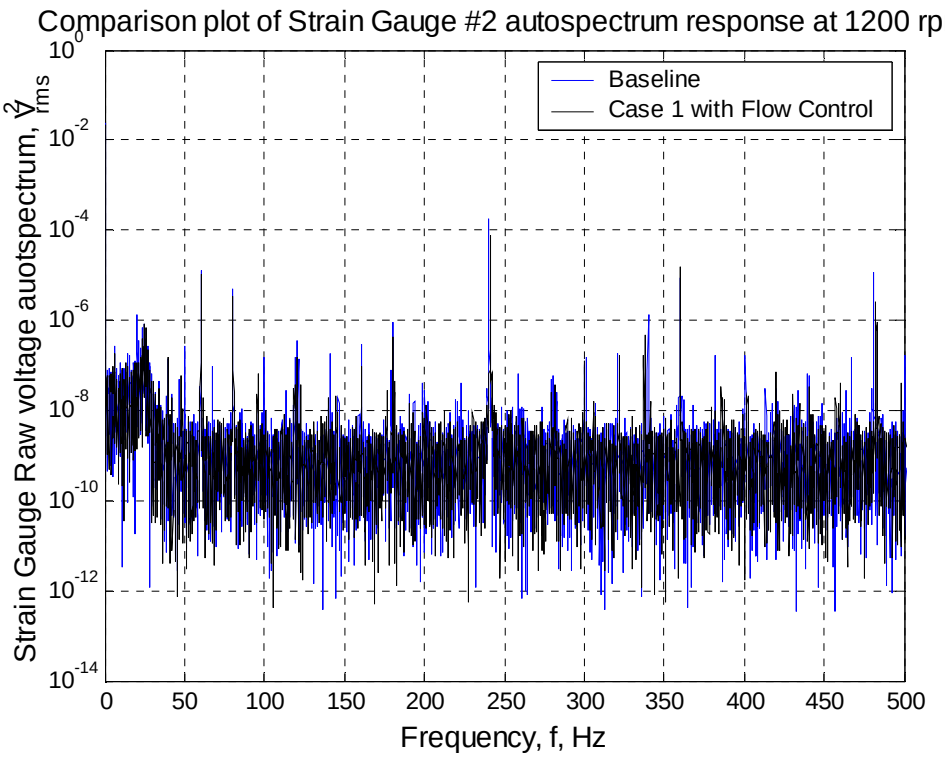

Figure E.4: Strain gauge #2 autospectrum for Case 1 trailing edge slot thickness

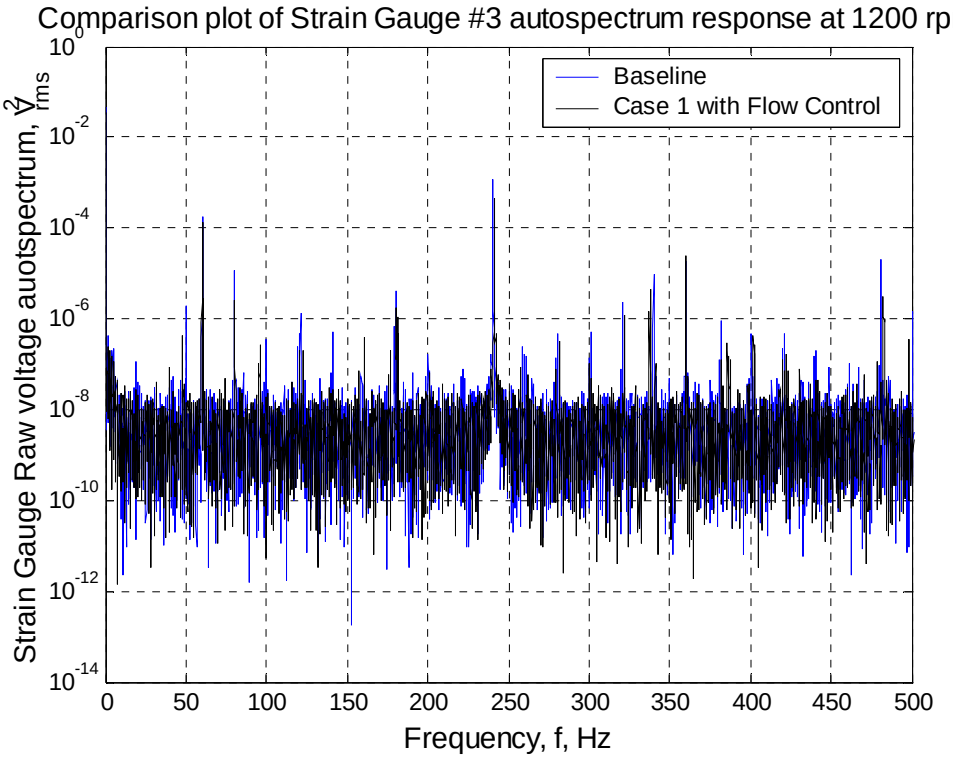

Figure E.5: Strain gauge # 3 autospectrum for Case 1 trailing edge slot thickness

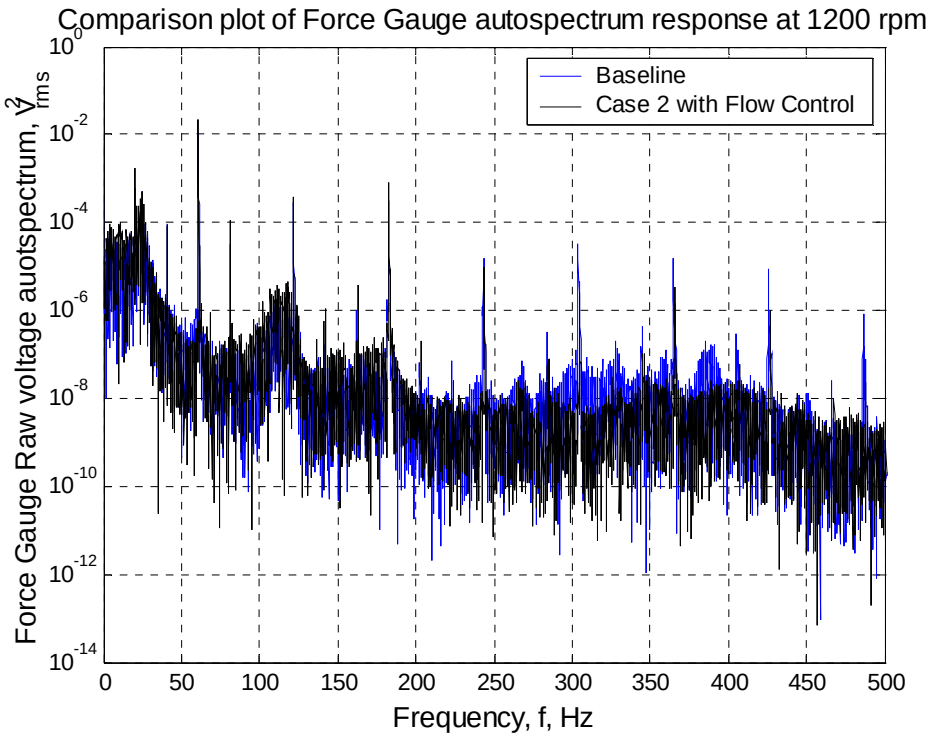

Figure E.6: Force gauge autospectrum for Case 2 trailing edge slot thickness

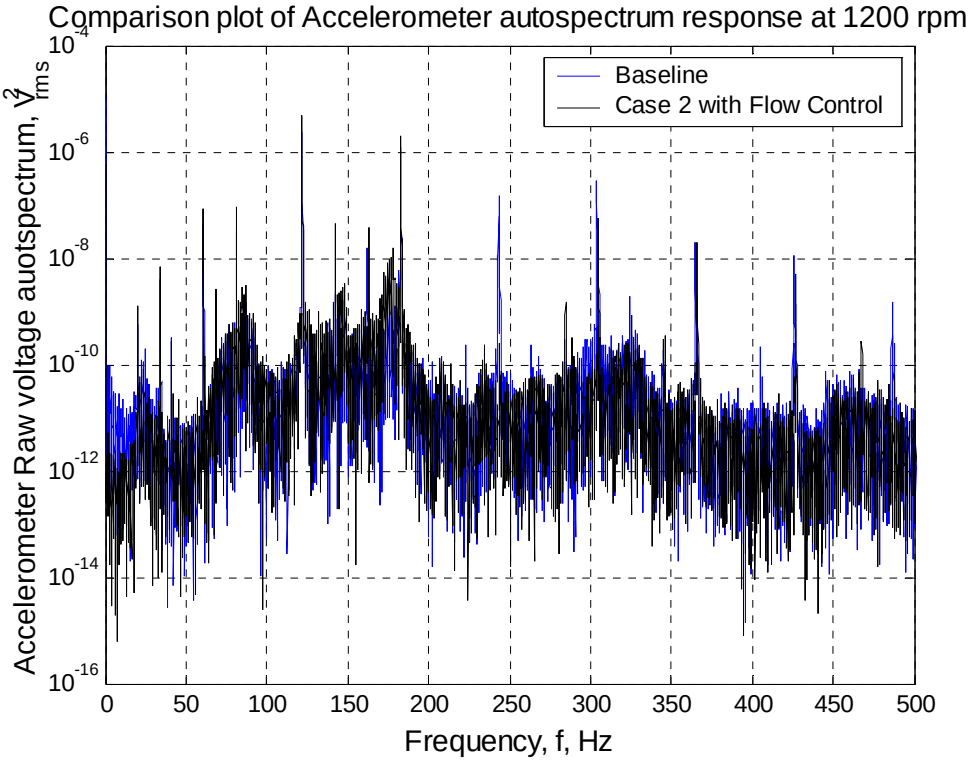

Figure E.7: Accelerometer autospectrum for Case 2 trailing edge slot thickness

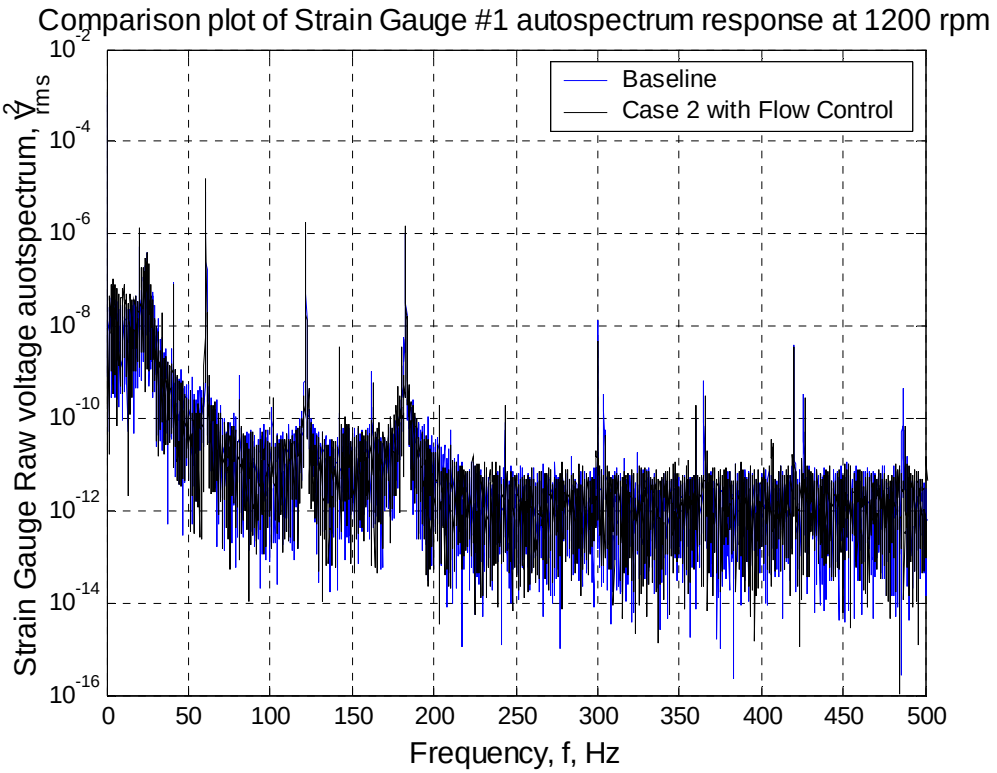

Figure E.8: Strain gauge #1 autospectrum for Case 2 trailing edge slot thickness

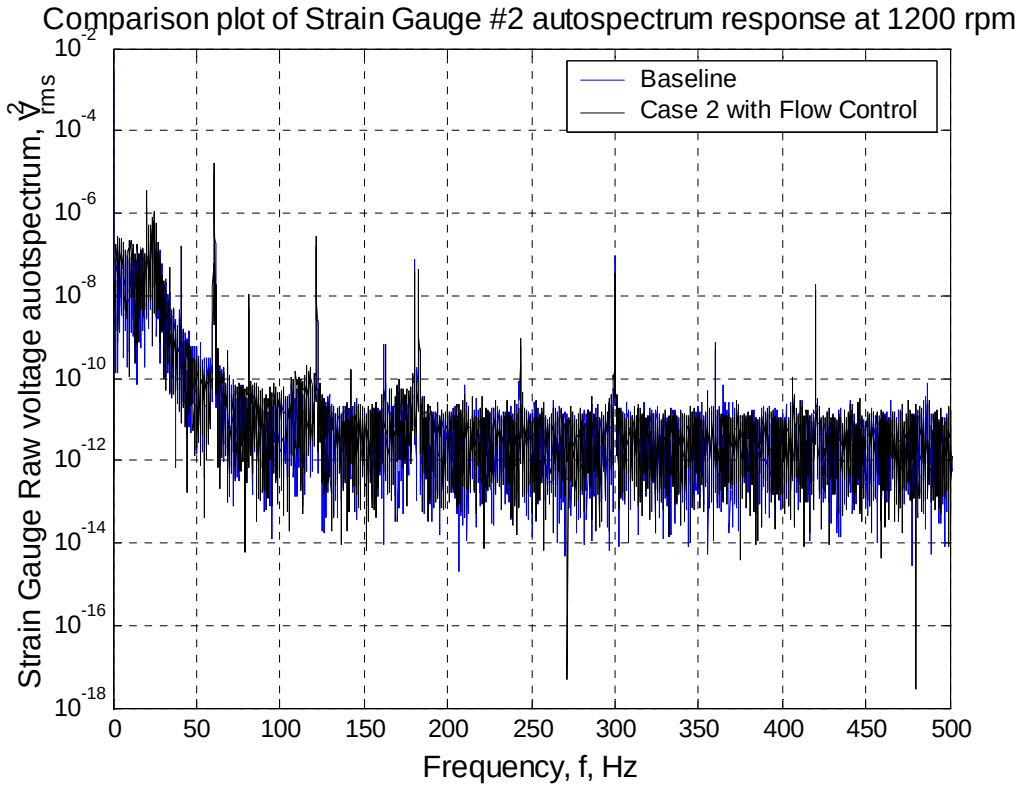

Figure E.9: Strain gauge #2 autospectrum for Case 2 trailing edge slot thickness

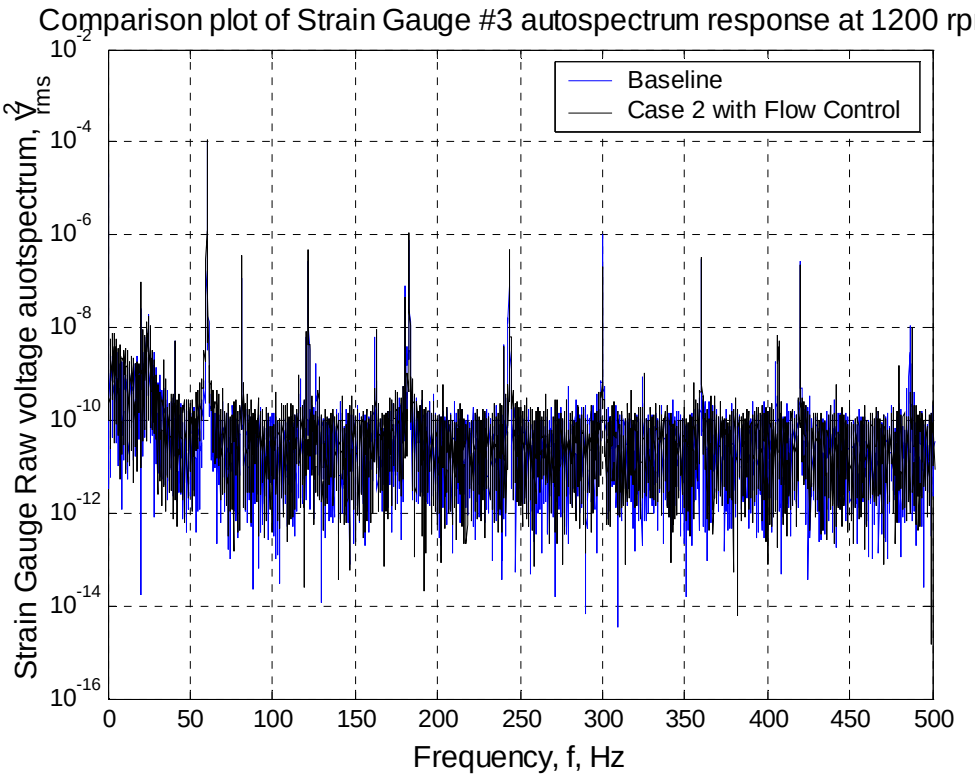

Figure E.10: Strain gauge #3 autospectrum for Case 2 trailing edge slot thickness

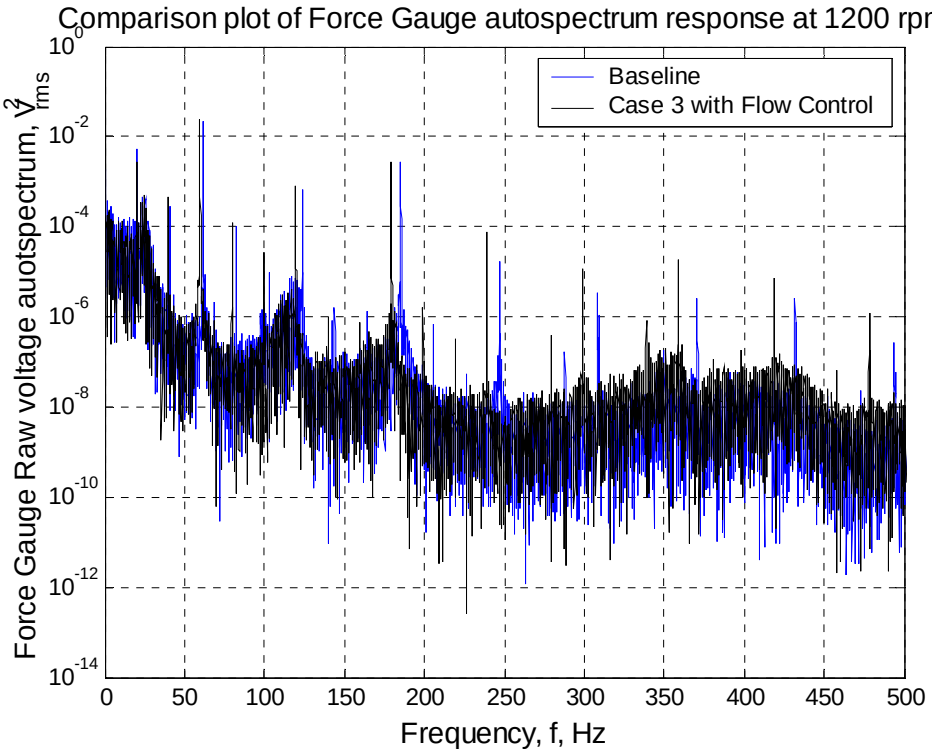

Figure E.11: Force gauge autospectrum for Case 3 trailing edge slot thickness

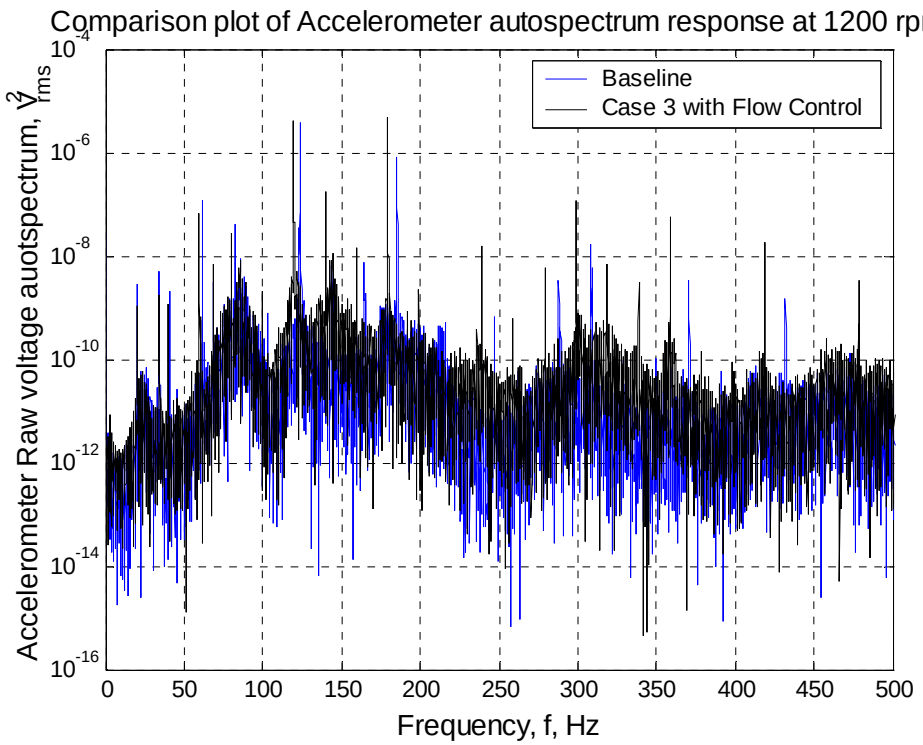

Figure E.12: Accelerometer autospectrum for Case 3 trailing edge slot thickness

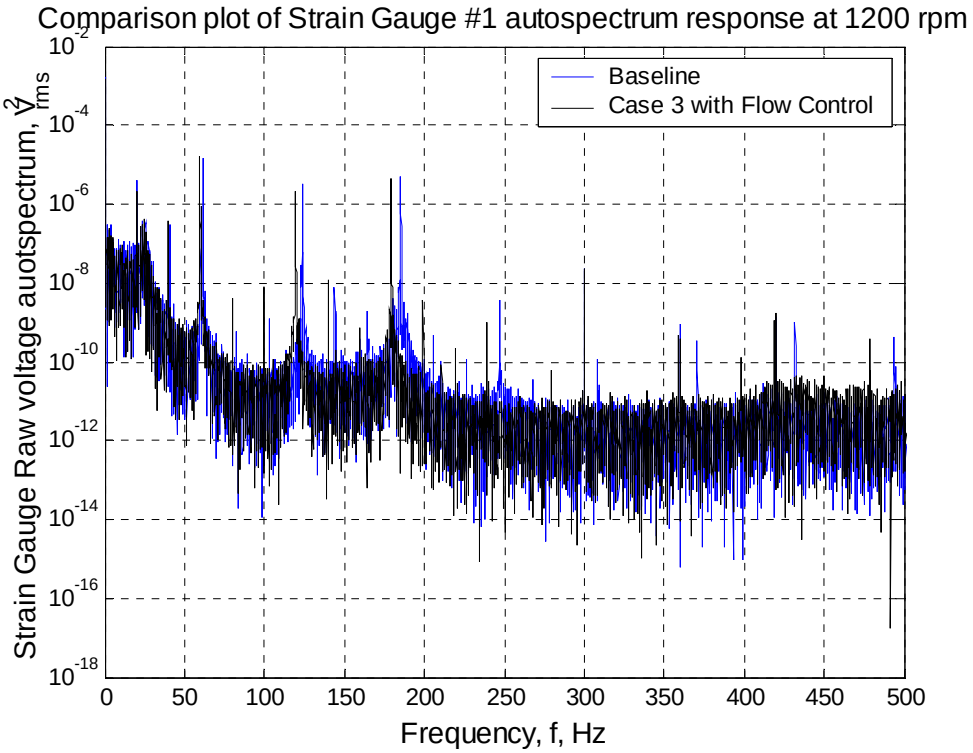

Figure E.13: Strain gauge #1 autospectrum for Case 3 trailing edge slot thickness

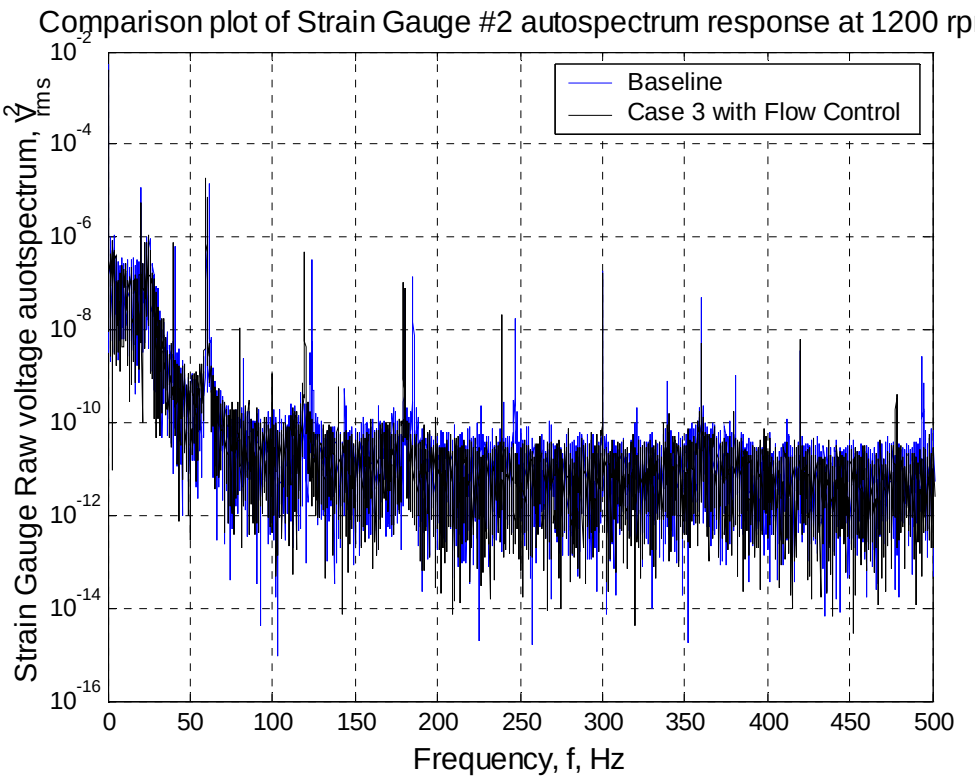

Figure E.14: Strain gauge #2 autospectrum for Case 3 trailing edge slot thickness

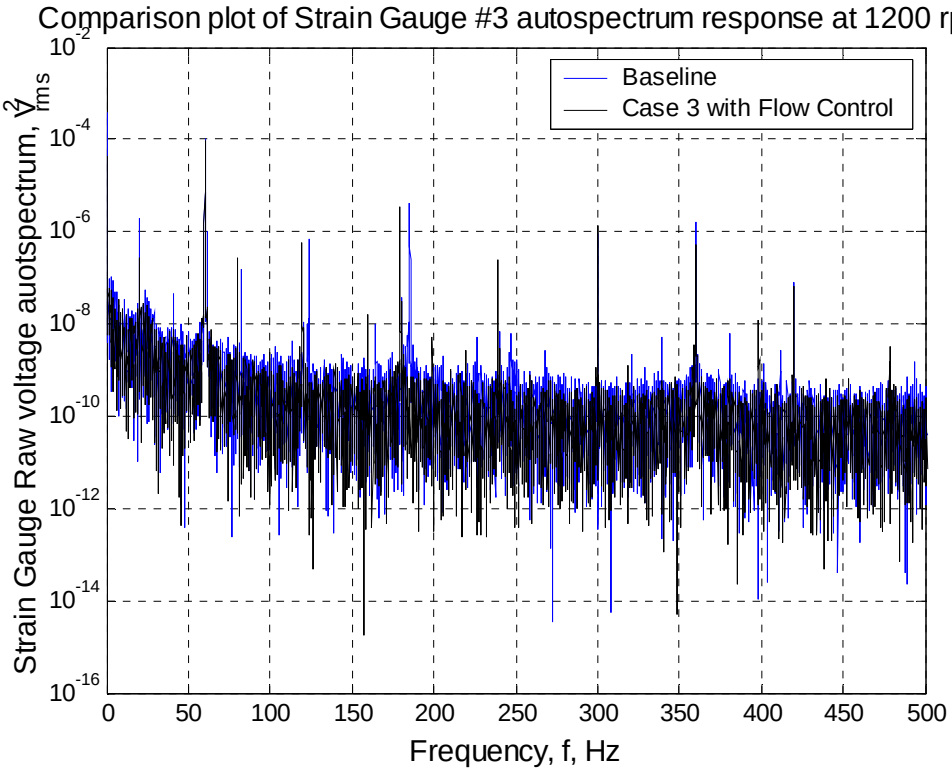

Figure E.15: Strain gauge #3 autospectrum for Case 3 trailing edge slot thickness

Appendix F Uncertainty Calculations

F.1 Student's t-test Hypothesis Test

To determine the likelihood that two datasets overlap, a Student's t-test is performed. The null hypothesis is that the means are not equal:

$$\begin{aligned} H_0 &: \mu_1 = \mu_2 \\ H_a &: \mu_1 \neq \mu_2 \end{aligned}. \qquad \text{F.1}$$

For this test the degrees of freedom is defined as

$$df = n_1 + n_2 - 2. \qquad \text{F.2}$$

where n_1 is the number of samples in set 1 and n_2 is the number of samples in set 2. The two sample t-test has a test statistic of

$$t_0 = \frac{(\bar{y}_1 - \bar{y}_2)}{s_p \sqrt{\frac{1}{n_1} + \frac{1}{n_2}}} \qquad \text{F.3}$$

where s_p is defined as

$$s_p = \sqrt{\frac{(n_1 - 1)s_1^{\,2} + (n_2 - 1)s_2^{\,2}}{n_1 + n_2 - 1}} \qquad \text{F.4}$$

with s_1 as the standard deviation of set 1 and s_2 as the standard deviation of set 2. The criteria for rejecting the null hypothesis is shown in Table F.1[33]

Table F.1: Rejection criteria for the Student's t-test

H_a	Reject H_0 if
$\mu_1 < \mu_2$	$t_0 < -t_{n1+n2-2,\alpha}$
$\mu_1 < \mu_2$	$t_0 > t_{n1+n2-2,\alpha}$
$\mu_1 \neq \mu_2$	$t_0 < -t_{n1+n2-2,\alpha/2}$

The results of the Student's t-tests for the LEB baseline data are shown in Table F.2. When the null hypothesis is rejected, this implies that the difference found between the two sets not likely to be the results of random error.[34] The rejection yields the conclusion that statistically the two

sets are the results of two different occurrences, i.e. the error of the data does not account for the difference in measured magnitude.

Table F.2: Results of the hypothesis test on the LEB Baseline data for several speed comparisons

Set 1	Set 2	t	Probability of H_o being true (%)	Accept/Reject H_0 with 95% confidence
1200 rpm	1400 rpm	-8.23	< 0.01	Reject
1400 rpm	1800 rpm	-2.20	3.5	Reject
1800	2000	4.85	< 0.01	Reject

F.2 Sensitivity Analysis of Force Gauge, Accelerometer, and Strain Gauges

The specifications given for the PCB 208C01 ICP Force Sensor state that the sensitivity is 115.7 mv/N with an uncertainty of +/- 1%. It was assumed that the uncertainty was 1% of the full scale value. For this gauge, the full scale value is 10 lb which can be converted into a voltage of 5151 mV. 1% of 5151 mV is 51.51 mV or 0.446 N.

Since this value did not correlate with the values given by the hypothesis test outlined in Section F.1, an alternate method of computing the approximate error was used. The largest source of error was the removal of the motor between tests. Therefore, by taking the baseline measurements at all five tested speeds for several days, a confidence interval can be calculated. The confidence interval gives an estimation of the error of the data. The 95% confidence interval is calculated by

$$\bar{y} \pm z_{\alpha/2} \frac{\sigma}{\sqrt{n}}, \qquad \text{F.5}$$

where y is the sample mean, sigma is the standard deviation, n is the number of samples, and z is the standard normal value. From Equation F.5 the error in the measurement as

$$\pm z_{\alpha/2} \frac{\sigma}{\sqrt{n}}. \qquad \text{F.6}$$

This formula was applied to the baseline LEB data to account for the experimental error of the system. Table F.3 shows the computed error for the force gauge measurements at each rpm. The technique of computing error only gives an estimation of the error. The definition of a confidence interval assumes that the distribution is normal, the central limit theorem states that a sample set of greater than 25 samples approaches a normal distribution. However, in this case only 18 samples were available for correlation. Therefore, the error estimation is only approximate. A similar analysis was conducted on the accelerometer measurements since no uncertainty was provided by the manufacturer.

Table F.3: Table of the estimated measurement error as computed by a 95% confidence interval

Motor Speed	Estimated Measurement Error	
	Force Gauge (N)	Accelerometer (m/s^2)
1200	0.0075	0.00080
1400	0.1009	0.00045
1600	0.1263	0.00054
1800	0.0394	0.00126
2000	0.0294	0.01649

The error in the strain gauge measurements were computed differently. Unlike the force and acceleration transducers, the main limitation on the stain gauge response was the resolution of the data acquisition (DAQ) system. The AI-16E-4 National Instruments DAQcard was capable of acquiring 12 bits of information at 500 kS/s. The range of input was 10 volts, thus giving a voltage resolution of 2.44 mV. The voltage can be converted to strain using the formula

$$\varepsilon = \frac{4\Delta e}{EK}, \qquad \text{F.7}$$

where e is the change in voltage output by the strain gauge, E is the excitation voltage provided by the amplifier, and K is the gauge factor given by the manufacturer. Since each strain gauge was given a slightly different excitation voltage, every strain gauge had a slightly different error.

The error for each strain gauge is shown in Table F.4. For the location of each strain gauge, see Figure 3.8.

Table F.4: Strain gauge measurement error for each strain gauge

Strain Gauge Location	Measurement Error (microstrain)
1	0.0091
2	0.0226
3	0.0181
4	0.0224

Appendix G References

[1] Fedaration of American Scientists, Military Analysis Network. http://www.fas.org/man/dod-101/sys/

[2] Dunne, R. C., Howe, M.S. "Wall-Bounded Blade-Tip Vortex Interaction Noise", Journal of Sound and Vibration v. 202, n.5, pg 605-618, 1997.

[3] Woodward, R. P., Balombin, J.R. "Tone Generation by Rotor-Downstream Strut Interaction", AIAA 83-0767, 1983.

[4] Goldstein, Marvin. Aeroacoustics. McGraw-Hill, New York. 1976.

[5] Chen, S. H., Eastland, A.H., Jackson, E.D. "Efficient Method for Predicting Rotor/Stator Interaction." Journal of Propulsion and Power, v 10, n 3, 1994.

[6] Giles, M.B. "Calculation of Unsteady Wake/Rotor Interaction." AIAA Paper 1987-0006, 1987

[7] Sawyer, S., Fleeter, S., Simonich, J. "Active Control of Discrete-Frequency Noise Generated by Rotor-Stator Interactions." Journal of Propulsion and Power, v 18. n 1, 2002.

[8] Hall, D.G., Woodward, R.P. "Assessment of Noise Control Measures for a Model Advanced Ducted Propulsor." Journal of Aircraft, v. 33, n. 3,1996.

[9] Simonich, J., Lavrich, P., Sofrinf, T., Topol, D. "Active Aerodynamic Control of Wake-Airfoil Interaction Noise – Experiment." AIAA Journal, v. 31, n. 10, 1993.

[10] Minter, J.A., Fleeter, S. "Active Control of Turbomachine Discrete Frequency Noise Utilizing Oscillating Flaps and Pistons". AIAA Journal, v. 35, n. 7, 1997.

[11] Elhadidi, B., Atassi, H.M. "Passive Control for Turbofan Tonal Noise". AIAA Journal, v. 43, n. 11, 2005.

[12] Kantola, R.A., Gliebe, P.R. "Effects of Vane/Blade Ration and Spacing on Fan Noise". AIAA 1981-2033, 1981.

[13] Hughes, C.E., Woodward, R.P., Podboy, G.G. "Effect of Tip Clearance of Fan Noise and Aerodynamics Performance". AIAA 2005-2875, 2005.

[14] Woodward, R.P., Elliott, D.M., Hughes, C. E., Berton, J.J. "Benefits of Swept-and-Leaned Stators for Fan Noise Reduction". Journal of Aircraft, v. 38, n. 6, 2001.

[15] Zhang, M., Wang, H., Tsukamoto, H. "Numerical Analysis of Unsteady Hydrodynamic Forces On A Diffuser Pump Impeller Due to Rotor-Stator Interaction", ASME/FEDSM2002-31181, 2002.

[16] Minton, C. M., "Wake Filling Techniques for Reducing Rotor-Stator Interaction Noise", Master's Thesis, Virginia Polytechnic Institute and Technical University, Blacksburg, VA, 2005.

[17] Brookfield, J.M., Waitz, I.A. "Trailing-Edge Blowing for Reduction of Turbomachinery Fan Noise." Journal of Propulsion and Power, v.16 n. 1, 2000.

[18] Langford, M.D. et al. "Fan Flow Control for Noise Reduction Part 3: Rig Testing of Optimal Design." AIAA 2005-3027, 2005

[19] Fite, E.B., Woodward, R.P., Podboy, G.G. "Effect of Trailing Edge Flow Injection of Fan Noise and Aerodynamic Performance". AIAA 2006-2844, 2006.

[20] Sutliff, D.L., Tweedt, D.L., Fite, E.B., Envia, E., "Low-Speed Fan Nose Reduction With Trailing Edge Blowing". AIAA 2002-2492, 2002.

[21] Naumann, R.G., "Control of the Wake from a Simulated Blade by Trailing Edge Blowing," Master's Thesis, Lehigh University, Bethlehem, PA, 1992.

[22] Fleming, J., Johnson, M.J. "Flow Control & Vibration Isolation for IMP Quieting", Techsburg, Inc., Phase I Final Report, Navy Contract N0014-04-M-0277, 2004.

[23] Wo, A.M., Lo, A.C., Chang, W.C. "Flow Control via Rotor Trailing Edge Blowing in Rotor/Stator Axial Compressor." Journal of Propulsion and Power, v 18, n 1, 2002.

[24] Kerrebrock, J.L. et al. "Aspirated Compressors", ASME International Gas Turbine & Aeroengine Congress and Exhibitiion. ASME 97-GT-525, 1997.

[25] Weiland, C.J., Vlachos, P.P. "Modification of Blade Vortex Interactions Using Leading Edge Blowing," ASME/FEDSM2006-98114, 2006.

[26] Black, Scott. Engineer, Naval Surface Warfare Center, Carderock Division, Propulsion and Fluid Systems Division. scott.black@navy.mil , 2006

[27] Nakamura, Y. "Vortex Shedding From Bluff Bodies and a Universal Strouhal Number." Journal of Fluids and Structures. v. 10, pp 159-171, 1996.

[28] Zandbergen, T. "Stator Vane Response Due to the Impingement of the Wake of an Unloaded Rotor." AIAA-88-2814, 1988.

[29] Uzol, O., Chow, Y., Soranna, F., Katz, J. "3D Structure of a Rotor Wake at Mid-Span and Tip Regions". AIAA 2004-2552, 2004.

[30] Shaw, L.M., Balombin, J.R., "Rotor Wake Characteristics Relevent to Rotor-Stator Interaction Noise Generation". Journal of Aircraft, v. 19, n. 11, 1982.

[31] Borgoltz, A., Geiger, D., Devenport, W.J. "Analysis of Wakes Shed by Idealized Aircraft Engine Fan Blade for Noise Reduction". AIAA 2004-2912, 2004.

[32] Anderson, J., Fleming, J. "Flow Control and Vibration Isolation for IMP Quieting", Techsburg, Inc., Phase II Progress Report 5, Navy Contract N00014-04-C-0323, October 2005.

[33] Ott, L., Longnecker, M. An Introduction to Statistical Methods and Data Analysis. 5th ed. Duxbury Press, 2001.

[34] College of St Benedicts and St John University Statistics Department. http://www.physics.csbsju.edu/stats/t-test.html